Suitably impressive thesis title

Lennart Golks
Department of Physics

A thesis submitted for the degree of
Doctor of Philosophy

October 2025

Acknowledgements

Personal

I would like to thank Alex Elliott for his wonderful help and support. None of this would be possible otherwise.

Institutional

If you want to separate out your thanks for funding and institutional support, I don't think there's any rule against it. Of course, you could also just remove the subsections and do one big traditional acknowledgement section.

Abstract

Your abstract text goes here. Check your departmental regulations, but generally this should be less than 300 words. See the beginning of Chapter **??** for more.

Contents

List of Figures

1 Introduction

Here, we briefly describe the currently used standard to retrieve atmospheric trace gas concentrations and what motivates us to employ a hierarchical Bayesian framework on an atmospheric limb sounder measuring ozone, where we contribute to existing methods and how we improve those. Lastly, we provide the reader with the thesis structure.

1.1 Motivation

Since the only currently operating ozone limb sounder, the Microwave Limb Sounder (MLS) on NASA's Aura satellite, is gradually drifting from its orbit and scheduled to be phased out by 2026 [1], a group led by Harald Schwefel has proposed an alternative approach to fill this observational gap using a much smaller platform, such as a disk-shaped resonator mounted on a 6U CubeSat [2]. The proposed system targets a narrow frequency band and converts the thermal radiation emitted by ozone from the terahertz region to the optical domain [3, 4].

This conversion offers a cost-effective and energy-efficient solution, as it circumvents the need for energy-hungry and large cooling devices that are traditionally required to capture terahertz signals. Instead, signal acquisition in the optical domain can be implemented by using compact, cheap, and low-power photonic technologies.

Currently, the inverse problem to retrieve any trace gas from limb-sounding data is approached by the atmospheric physics community using optimisation and regularisation techniques developed in the 1970s [5, 6] This approach is based on a "best fit to data but not the best fit to parameters" [7]. Instead, we employ a hierarchically structured Bayesian framework to infer ozone concentrations, where we find the best distribution of parameters given some data. This probabilistic approach provides estimates and their true uncertainties.

1.2 Research Gap and Contribution

As already mentioned, currently the MLS retrieval algorithm [8] is based on the "optimal estimation" method from [5]. This approach iteratively minimises a squared residual norm by fitting parameters to a set of data and penalises against a chosen regularisation. This does not provide comprehensive information about the parameters, the underlying correlation structures and can lead to unphysical results, e.g. negative ozone concentration values [9]. The errors provided are based on a local derivative of the forward map around one optimal solution, which is obviously highly sensitive to its location. Additionally, these retrievals are conditioned on external estimates of other parameters, such as temperature or pressure [8]. This does result in biased solutions, where the bias is then removed based on empirical decisions [52, 55]. Even current machine learning efforts condition on one single noise hyper-parameter value in their model, which is trained for about one month, and do not include noise as a retrieval parameter, additionally they do compare to a "ground truth" provided by the previously described optimal estimation approach [10, 11].

We address these limitations by including measurement noise as well as other hyperparamters, e. g. smoothness of the ozone profile, explicitly in both the modelling and inversion process to provide a range of ozone profiles all fitting to the data within seconds. Naturally, noise (hyper-parameter) is a random process and occording to that noise we deal with distributions over hyperparameters and parameters (e.g. ozone concentrations) and can provide errors according to those distributions, instead of one "optimal" solution. This approach is called *hierarchical* Bayesian modelling. Livesey et al. [8] report "unexpected spectrally correlated noise" on the MLS aura, so here is another real reason why one should include and estimate noise.

To solve this inverse problem within a linear-Gaussian hierarchical Bayesian framework, we apply the marginal-and-then-conditional (MTC) method [12], with which we evaluate distributions over both hyper-parameters (e.g. noise and ozone smoothness) and parameters. This is a fairly new method within the Bayesian community, and we are the first to our knowledge to apply it to a forward model based on the radiative transfer equation (RTE). Then, instead of sampling from those posterior distributions, we are the first to utilise a tensor-train (TT) to approximate the posterior distribution, which enables us to provide estimates and uncertainties via quadrature or the inverse Rosenblatt transform (IRT).

Since the RTE is weakly non-linear, we approximate the RTE with an affine map, which seems to be another novelty in the field of atmospheric remote sensing. Additionally, we provide a new approach by jointly inferring pressure, temperature and ozone profiles given one set of measurements.

1.3 Thesis Structure

In Ch. 2, we give a brief overview of the methods used and provide references for more details. Then, in Ch. 3, we provide the forward model based on a simplified RTE, and discuss how to measure most effectively. Using our findings, we simulate some noisy data for an idealised limb sounder within a simplified atmosphere based on the RTE. Then, in Ch. 4, we setup our linear hierarchical Bayesian model and discuss some prior modelling. Given the simulated data, we provide posterior distributions of our Bayesian framework based on the linearised RTE to then approximate the non-linear forward model with an affine map. We compare a regularisation solution with the posterior distributions of the approximated linear Bayesian model against a ground truth ozone profile, where we also provide posterior distributions over hyper-parameters. Additionally, we condition on an ozone profile and noise sample to give joint pressure and temperature posterior profiles. Furthermore, we assess and discuss some errors of the approximation used to provide arguments for choices made regarding those approximations. Lastly, we discuss our results and provide an outlook, see Ch. 5.

2 Theoretical and Technical Background

In this chapter, we provide introductions and brief derivations of the methods used in this thesis, as well as references for more details. We keep it as general as possible, as the expressions specifically tailored towards the forward map will be presented in the results Chapter 4. We begin by introducing a general hierarchical Bayesian approach to an inverse problem. Next, we provide the basics of Metropolis-Hastings sampling, more specifically, the essentials of Markov-Chain Monte Carlo (MCMC) methods. Further, we explain how we approximate functions using a Tensor-Train (TT) approach, which enables us to calculate marginals from the posterior distribution cheaply. Then, we elaborate on the Wasserstein distance for assessing upper error bounds. Lastly, we provide some background information on affine maps and the Tikhonov regularisation method.

2.1 Hierarchical Bayesian Inference

Assume we observe some data

$$\boldsymbol{y} = \boldsymbol{A}(\boldsymbol{x}) + \boldsymbol{\eta}, \tag{2.1}$$

based on a forward model $\boldsymbol{A}(\boldsymbol{x})$, which may be non-linear, a unknown parameter $\boldsymbol{x}$ and some additive random noise $\boldsymbol{\eta}$. Naturally, due to the noise, which we classify through a hyper-parameter, we deal with a random process, and we wish to include that in our hierarchically ordered modelling. Then define the likelihood function $\pi(\boldsymbol{y}|\boldsymbol{\theta}, \boldsymbol{x})$ according to the nature of the noise as well as all relevant information about the measurement process, captured by the model $\boldsymbol{A}(\boldsymbol{x})$. We read $\pi(\boldsymbol{y}|\boldsymbol{\theta}, \boldsymbol{x})$ as the distribution over $\boldsymbol{y}$ conditioned on $\boldsymbol{x}$ and $\boldsymbol{\theta}$, and $\boldsymbol{\eta} \sim \pi_{\boldsymbol{\eta}}(\cdot|\boldsymbol{\theta})$ as $\boldsymbol{\eta}$ is distributed as $\pi_{\boldsymbol{\eta}}(\cdot|\boldsymbol{\theta})$. Here $\boldsymbol{\theta}$ may account for multiple hyper-parameters, e.g. describing the distribution $\pi_{\boldsymbol{\eta}}(\cdot|\boldsymbol{\theta})$ over the

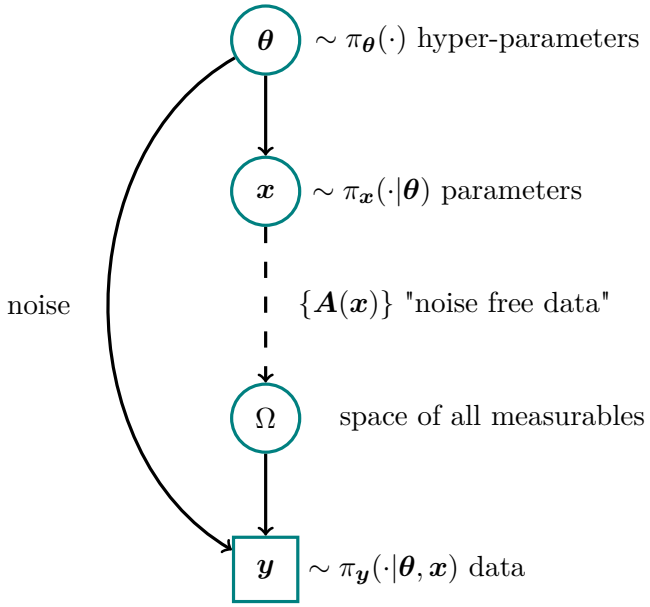

Figure 2.1: The directed acyclic graph (DAG) for an inverse problem visualises statistical dependencies as solid line arrows and deterministic dependencies as dotted arrows. The hyper-parameters $\boldsymbol{\theta}$ are distributed as the hyper-prior distribution $\pi(\boldsymbol{\theta})$. The prior distribution $\pi_{\boldsymbol{x}}(\cdot|\boldsymbol{\theta})$ for the parameter $\boldsymbol{x}$ and the noise are statistically dependent on some of those hyper-parameters. Then a parameter $\boldsymbol{x} \sim \pi_{\boldsymbol{x}}(\cdot|\boldsymbol{\theta})$ is mapped onto the space of all measurables $\boldsymbol{\Omega} = \boldsymbol{A}(\boldsymbol{x})$ deterministically through the forward model. From the space of all measurable noise free data we observe a data set $\boldsymbol{y} = \boldsymbol{A}(\boldsymbol{x}) + \boldsymbol{\eta}$ with some random noise $\boldsymbol{\eta} \sim \pi_{\boldsymbol{\eta}}(\cdot|\boldsymbol{\theta})$, which determines the likelihood function $\pi(\boldsymbol{y}|\boldsymbol{\theta}, \boldsymbol{x})$.

noise vector $\boldsymbol{\eta}$, and describing physical properties or functional dependencies of $\boldsymbol{x}$, e.g. smoothness, trough the prior distribution $\pi(\boldsymbol{x}|\boldsymbol{\theta})$. Consequently we define a hyper-prior distribution $\pi(\boldsymbol{\theta})$, where $\pi(\boldsymbol{x}, \boldsymbol{\theta}) = \pi(\boldsymbol{x}|\boldsymbol{\theta})\pi(\boldsymbol{\theta})$. Choosing these prior distributions is ultimately a modeller's choice and crucial, as it shall not affect the posterior distribution

$$\pi(\boldsymbol{x}, \boldsymbol{\theta}|\boldsymbol{y}) = \frac{\pi(\boldsymbol{y}|\boldsymbol{x}, \boldsymbol{\theta})\pi(\boldsymbol{x}, \boldsymbol{\theta})}{\pi(\boldsymbol{y})} \propto \pi(\boldsymbol{y}|\boldsymbol{x}, \boldsymbol{\theta})\pi(\boldsymbol{x}, \boldsymbol{\theta})\,, \tag{2.2}$$

which according to Bayes theorem gives us a distribution of $\boldsymbol{x}$ and $\boldsymbol{\theta}$ given (conditioned) on the data. Note that here we include the hyper-parameters within the posterior distribution, which is the key idea of hierarchical Bayesian modelling, as we do not only aim to quantify the posterior distribution over the parameters $\boldsymbol{x}$ but also the posterior distribution over the hyper-parameter $\boldsymbol{\theta}$. We can visualise this hierarchically ordered correlation structure between parameters as well as how distributions progress through a measurement process, using a directed acyclic graph (DAG), see Figure 2.1.

The expectation of any function $h(\boldsymbol{x}_{\boldsymbol{\theta}})$, where $\boldsymbol{x}$ may depend on $\boldsymbol{\theta}$, is described as

$$\mathrm{E}_{\boldsymbol{x},\boldsymbol{\theta}|\boldsymbol{y}}[h(\boldsymbol{x}_{\boldsymbol{\theta}})] = \underbrace{\int\int h(\boldsymbol{x}_{\boldsymbol{\theta}})\,\pi(\boldsymbol{x}, \boldsymbol{\theta}|\boldsymbol{y})\,\mathrm{d}\boldsymbol{x}\,\mathrm{d}\boldsymbol{\theta}}_{\boldsymbol{\mu}_{\mathrm{int}}}\,. \tag{2.3}$$

If that is a high-dimensional integral and computationally not feasible to solve, we approximate

$$\mathrm{E}_{\boldsymbol{x},\boldsymbol{\theta}|\boldsymbol{y}}[h(\boldsymbol{x}_{\boldsymbol{\theta}})] \approx \underbrace{\frac{1}{N}\sum_{k=1}^{N} h(\boldsymbol{x}_{\boldsymbol{\theta}}^{(k)})}_{\boldsymbol{\mu}_{\text{samp}}}, \tag{2.4}$$

with an the unbiased sample-based Monte Carlo estimate [13] for large enough N (law of large numbers [14, Chapter 17]). Here, the samples $\{\boldsymbol{x}^{(k)}, \boldsymbol{\theta}^{(k)}\} \sim \pi_{\boldsymbol{x},\boldsymbol{\theta}}(\cdot|\boldsymbol{y})$, for $k = 1, \ldots, N$, form a sample set $\mathcal{M} = \{(\boldsymbol{x}, \boldsymbol{\theta})^{(1)}, \ldots, (\boldsymbol{x}, \boldsymbol{\theta})^{(N)}\}$.

Generating a representative sample set quickly from the posterior distribution often presents a significant challenge. This is mainly due to the strong correlations that usually exist between the parameters and hyper-parameters, as discussed by Rue and Held in [15] and illustrated in Appendix A.1. If $\boldsymbol{x}$ can not be parametrised directly in terms of the hyper-parameters $\boldsymbol{\theta}$, i.e., $\boldsymbol{x}(\boldsymbol{\theta})$, it is beneficial to factorise the posterior distribution as

$$\pi(\boldsymbol{x}, \boldsymbol{\theta}|\boldsymbol{y}) = \pi(\boldsymbol{x}|\boldsymbol{\theta}, \boldsymbol{y})\, \pi(\boldsymbol{\theta}|\boldsymbol{y}), \tag{2.5}$$

into the conditional posterior $\pi(\boldsymbol{x}|\boldsymbol{\theta}, \boldsymbol{y})$ over the latent field $\boldsymbol{x}$ and the marginal posterior

$$\pi(\boldsymbol{\theta}|\boldsymbol{y}) = \frac{\pi(\boldsymbol{y}|\boldsymbol{\theta}, \boldsymbol{x})\pi(\boldsymbol{x}|\boldsymbol{\theta})\pi(\boldsymbol{\theta})}{\pi(\boldsymbol{x}|\boldsymbol{\theta}, \boldsymbol{y})\pi(\boldsymbol{y})} \propto \frac{\pi(\boldsymbol{y}|\boldsymbol{\theta}, \boldsymbol{x})\pi(\boldsymbol{x}|\boldsymbol{\theta})\pi(\boldsymbol{\theta})}{\pi(\boldsymbol{x}|\boldsymbol{\theta}, \boldsymbol{y})} \tag{2.6}$$

over the hyper-parameters $\boldsymbol{\theta}$. In [16], they classify inverse problems into problems with known or unknown conditional posterior distributions, and conclude that if $\pi(\boldsymbol{x}|\boldsymbol{\theta}, \boldsymbol{y}) = \pi(\boldsymbol{y}|\boldsymbol{x}, \boldsymbol{\theta})\pi(\boldsymbol{x}|\boldsymbol{\theta})/\pi(\boldsymbol{y}|\boldsymbol{\theta})$ has a known form, the normalising constant is available $\int \pi(\boldsymbol{y}|\boldsymbol{x}, \boldsymbol{\theta})\pi(\boldsymbol{x}|\boldsymbol{\theta})\mathrm{d}\boldsymbol{x} = \pi(\boldsymbol{y}|\boldsymbol{\theta}) \propto \pi(\boldsymbol{\theta}|\boldsymbol{y})/\pi(\boldsymbol{\theta})$ and one can almost surely determine the $\boldsymbol{\theta}$-dependence of the marginal posterior $\pi(\boldsymbol{\theta}|\boldsymbol{y})$.

This approach, known as the marginal and then conditional (MTC) method, is particularly advantageous when $\boldsymbol{x} \in \mathbb{R}^n$ is high-dimensional, while $\boldsymbol{\theta} \in \mathbb{R}^{n_{\boldsymbol{\theta}}}$ is low-dimensional, so that $n_{\boldsymbol{\theta}} \ll n$ and evaluation $\pi(\boldsymbol{\theta}|\boldsymbol{y})$ is cheap. Applying the law of total expectation [17], Eq. (2.3) becomes

$$\mathbb{E}_{\boldsymbol{x}|\boldsymbol{y}}[h(\boldsymbol{x})] = \mathbb{E}_{\boldsymbol{\theta}|\boldsymbol{y}}\left[\mathbb{E}_{\boldsymbol{x}|\boldsymbol{\theta},\boldsymbol{y}}[h(\boldsymbol{x}_{\boldsymbol{\theta}})]\right] = \int \mathbb{E}_{\boldsymbol{x}|\boldsymbol{\theta},\boldsymbol{y}}\left[h(\boldsymbol{x}_{\boldsymbol{\theta}})\right]\, \pi(\boldsymbol{\theta}|\boldsymbol{y})\, \mathrm{d}\boldsymbol{\theta}, \tag{2.7}$$

where, in the case of a linear-Gaussian hierarchical Bayesian model, both the marginal distribution and the inner expectation $\mathbb{E}_{\boldsymbol{x}|\boldsymbol{\theta},\boldsymbol{y}}\left[h(\boldsymbol{x}_{\boldsymbol{\theta}})\right]$ are well defined see next subsection. Furthermore, the central limit theorem states that the sample mean $\boldsymbol{\mu}_{\text{samp}}^{(i)}$, of independent sample sets $\mathcal{M}_i$ for $i = 1, \ldots, n$ of any distribution, converges in distribution to a normal distribution so that

$$\sqrt{n}(\boldsymbol{\mu}_{\text{samp}}^{(i)} - \boldsymbol{\mu}_{\text{int}}) \xrightarrow{\mathcal{D}} \mathcal{N}(0, \sigma^2)[18], \tag{2.8}$$

and if $\sigma^2 < \infty$ the Monte-Carlo error $\boldsymbol{\mu}_{\text{samp}}^{(i)} - \boldsymbol{\mu}_{\text{int}}$ is bounded.

Integrated Autocorrelation time

To assess the error σ^2 of chain $\mathcal{M}_i$, we ignore systematic error due to initialisation bias (burn-in period), but we have to take into account that samples produced by any system or algorithm are correlated. To derive the integrated autocorrelation time (IATC), we follow the lecture notes [19]. In general, the error of a Monte-Carlo-based estimate from a sample set $\mathcal{M}_i = \{\boldsymbol{x}^{(1)}, \dots, \boldsymbol{x}^{(k)}, \dots, \boldsymbol{x}^{(s)}, \dots, \boldsymbol{x}^{(N)}\} \sim \pi(\boldsymbol{x}|\boldsymbol{y})$ is:

$$(\sigma^{(i)})^2 = \mathrm{var}(\boldsymbol{\mu}^{(i)}_{\mathrm{samp}}) = \mathrm{var}(\mathrm{E}_{\boldsymbol{x}|\boldsymbol{y}}[h(\boldsymbol{x})]) = \left(\frac{1}{N}\sum_{k=1}^{N} h(\boldsymbol{x}^{(k)}) - \boldsymbol{\mu}^{(i)}\right)^2 . \tag{2.9}$$

Expanding this summation, we see that

$$\left(\frac{1}{N}\sum_{k=1}^{N} h(\boldsymbol{x}^{(k)}) - \boldsymbol{\mu}^{(i)}\right)^2 = \frac{\mathrm{var}(\boldsymbol{\mu}^{(i)}_{\mathrm{samp}})}{N^2}\sum_{k,s=1}^{N} \rho(k-s)\,, \tag{2.10}$$

with the normalised auto correlation coefficient $\rho(k-s) = \Gamma(k-s)/\Gamma(0)$ at lag $k-s$, where the auto correlation coefficient $\Gamma(k-s) = \big(h(\boldsymbol{x}^{(k)}) - \boldsymbol{\mu}^{(i)}\big)\big(h(\boldsymbol{x}^{(s)}) - \boldsymbol{\mu}^{(i)}\big)$ and $\Gamma(0) = \mathrm{var}(\boldsymbol{\mu}^{(i)}_{\mathrm{samp}})$ for $k = s$. Typically $\Gamma(t)$ decays exponentially so that $\Gamma(t) \overset{t\to\infty}{\propto} \exp\{-t/\tau\}$ and for positive τ and $N \gg \tau$ we can approximate

$$(\sigma^{(i)})^2 \approx \frac{\mathrm{var}(h(\boldsymbol{x}))}{N}\underbrace{\sum_{t=-\infty}^{\infty}\rho(t)}_{:=2\tau_{\mathrm{int}}} = \mathrm{var}(h(\boldsymbol{x}))\frac{2\tau_{\mathrm{int}}}{N}\,, \tag{2.11}$$

where define the IATC as in [19, pp. 103-105]. See Appendix A.2 and [20] for a more detailed derivation. The IACT provides a good estimate of how many steps the sampling algorithm needs to take to produce one independent sample, accordingly we define the effective sample size as $\frac{2\tau_{\mathrm{int}}}{N}$.

Linear-Gaussian hierarchical Bayesian model

In case of normally distributed noise $\boldsymbol{\eta} \sim \mathcal{N}(0, \boldsymbol{\Sigma}(\boldsymbol{\theta}))$, with zero mean and covariance $\boldsymbol{\Sigma}(\boldsymbol{\theta})$, and a linear model $\boldsymbol{A}$, the data is given as

$$\boldsymbol{y} = \boldsymbol{A}\boldsymbol{x} + \boldsymbol{\eta}\,, \tag{2.12}$$

and we can derive the marginal and conditional posterior distribution explicitly. We define our hierarchical Bayesian model as

$$\boldsymbol{y}|\boldsymbol{x}, \boldsymbol{\theta} \sim \mathcal{N}(\boldsymbol{A}\boldsymbol{x}, \boldsymbol{\Sigma}(\boldsymbol{\theta})) \tag{2.13a}$$

$$\boldsymbol{x}|\boldsymbol{\theta} \sim \mathcal{N}(\boldsymbol{\mu}, \boldsymbol{Q}(\boldsymbol{\theta})^{-1}) \tag{2.13b}$$

$$\boldsymbol{\theta} \sim \pi(\boldsymbol{\theta}), \tag{2.13c}$$

with a Gaussian likelihood function $\pi(\boldsymbol{y}|\boldsymbol{x},\boldsymbol{\theta})$, the prior mean $\boldsymbol{\mu}$, prior precision $\boldsymbol{Q}(\boldsymbol{\theta})$ and a hyper-prior distribution $\pi(\boldsymbol{\theta})$. To derive the marginal posterior and the conditional posterior distribution, we consider the joint multivariate Gaussian distribution

$$\begin{pmatrix}\boldsymbol{x}\\ \boldsymbol{y}\end{pmatrix} \sim \mathcal{N}\left[\begin{pmatrix}\boldsymbol{\mu}\\ \boldsymbol{A\mu}\end{pmatrix}, \begin{pmatrix}\boldsymbol{Q}(\boldsymbol{\theta})+\boldsymbol{A}^T\boldsymbol{\Sigma}(\boldsymbol{\theta})^{-1}\boldsymbol{A} & -\boldsymbol{A}^T\boldsymbol{\Sigma}(\boldsymbol{\theta})^{-1}\\ \boldsymbol{\Sigma}(\boldsymbol{\theta})^{-1}\boldsymbol{A} & \boldsymbol{\Sigma}(\boldsymbol{\theta})^{-1}\end{pmatrix}^{-1}\right], \tag{2.14}$$

where we provide the joint precision matrix as in [21]. Immediately, we formulate the conditional posterior as

$$\boldsymbol{x}|\boldsymbol{y},\boldsymbol{\theta} \sim \mathcal{N}(\boldsymbol{\mu}+(\boldsymbol{Q}(\boldsymbol{\theta})+\boldsymbol{A}^T\boldsymbol{\Sigma}(\boldsymbol{\theta})^{-1}\boldsymbol{A})^{-1}(\boldsymbol{y}-\boldsymbol{A\mu}),(\boldsymbol{Q}(\boldsymbol{\theta})+\boldsymbol{A}^T\boldsymbol{\Sigma}(\boldsymbol{\theta})^{-1}\boldsymbol{A})^{-1}). \tag{2.15}$$

Then the marginal posterior distribution over the hyper-parameters can be derived as in Eq. 2.6, where, as noted in [12], the parameter $\boldsymbol{x}$ cancels and we arrive at

$$\begin{aligned}\pi(\boldsymbol{\theta}|\boldsymbol{y}) \propto &\sqrt{\frac{\det(\boldsymbol{\Sigma}(\boldsymbol{\theta})^{-1})\det(\boldsymbol{Q}(\boldsymbol{\theta}))}{\det(\boldsymbol{Q}(\boldsymbol{\theta})+\boldsymbol{A}^T\boldsymbol{\Sigma}(\boldsymbol{\theta})^{-1}\boldsymbol{A})}}\exp\Big\{-\frac{1}{2}(\boldsymbol{y}-\boldsymbol{A\mu})^T\\ &[\boldsymbol{\Sigma}(\boldsymbol{\theta})^{-1}-\boldsymbol{\Sigma}(\boldsymbol{\theta})^{-1}\boldsymbol{A}(\boldsymbol{Q}(\boldsymbol{\theta})+\boldsymbol{A}^T\boldsymbol{\Sigma}(\boldsymbol{\theta})^{-1}\boldsymbol{A})^{-1}\boldsymbol{A}^T\boldsymbol{\Sigma}(\boldsymbol{\theta})^{-1}](\boldsymbol{y}-\boldsymbol{A\mu})\Big\}\pi(\boldsymbol{\theta}).\end{aligned} \tag{2.16}$$

Having the marginal posterior distribution available breaks up the correlation structure between $\boldsymbol{x}$ and $\boldsymbol{\theta}$, see Appendix A.1, and makes the marginal and then conditional (MTC) approach so efficient [12]. This scheme evaluates the marginal posterior values first and then conditions on hyper-parameters to draw posterior samples $\boldsymbol{x} \sim \pi(\boldsymbol{x}|\boldsymbol{y},\boldsymbol{\theta})$ or to evaluate expectation and variance of $\pi(\boldsymbol{x}|\boldsymbol{y})$ by integration over the marginal posterior.

2.2 Sampling Methods

In this section we present the underlying methodology of the sampling methods used in this thesis and show how these methods draw samples
$\mathcal{M} = \{(\boldsymbol{x},\boldsymbol{\theta})^{(1)},\dots,(\boldsymbol{x},\boldsymbol{\theta})^{(k)},\dots,(\boldsymbol{x},\boldsymbol{\theta})^{(N)}\} \sim \pi(\boldsymbol{x},\boldsymbol{\theta}|\boldsymbol{y})$ from the desired target distribution, so that we can calculate sample-based estimates as in Eq. 2.4. Here, $\mathcal{M}$ denotes a Markov chain, where each new sample $(\boldsymbol{x},\boldsymbol{\theta})^{(k)}$ is only affected by the previous one, $(\boldsymbol{x},\boldsymbol{\theta})^{(k-1)}$. Markov chain Monte Carlo (MCMC) methods generate such a chain $\mathcal{M}$ using random (Monte Carlo) proposals $(\boldsymbol{x},\boldsymbol{\theta})^{(k)} \sim q(\cdot|(\boldsymbol{x},\boldsymbol{\theta})^{(k-1)})$ according to a proposal distribution conditioned on the previous sample (Markov), where ergodicity of the chain $\mathcal{M}$ is a sufficient criterion for using sample-based estimates [7, 13].

The ergodicity theorem in [7] states that, if a Markov chain $\mathcal{M}$ is aperiodic, irreducible, and reversible, then it converges to a unique stationary equilibrium distribution. In other words, if the chain can reach any state from any other state (irreducibility), is not stuck

in periodic cycles (aperiodicity), and is reversible (detailed balance condition [7]). Then the chain converges to the desired target distribution with $\mathcal{M} \sim \pi(\boldsymbol{x}, \boldsymbol{\theta}|\boldsymbol{y})$. In practice, one can inspect the trace $\pi(\boldsymbol{x}^{(k)}, \boldsymbol{\theta}^{(k)}|\boldsymbol{y})$ for $k = 1, \ldots, N$ and visually assess convergence and mixing properties of the chain to evaluate ergodicity. The sampling methods used in this thesis possess proven ergodic properties, and we therefore refer the reader to the corresponding literature for further details.

2.2.1 Sampling from the Marginal Posterior

As in Eq. 2.5, when using the MTC method we sample from $\pi(\boldsymbol{\theta}|\boldsymbol{y})$ first and then determine the full conditional $\pi(\boldsymbol{x}|\boldsymbol{\theta}, \boldsymbol{y})$ as in Eq. 2.7. To sample from $\pi(\boldsymbol{\theta}|\boldsymbol{y})$, we use a Metropolis-within-Gibbs (MWG) sampler as described in [12]. We apply the MWG sample for the two-dimensional case only, with $\boldsymbol{\theta} = (\theta_1, \theta_2)$, where we perform a Metropolis step in the θ_1 direction and a Gibbs step in the θ_2 direction. Ergodicity for this approach is proven in [22].

The Metropolis-within-Gibbs algorithm begins with an initial guess $\boldsymbol{\theta}^{(t)}$ at $t = 0$. We then propose a new sample $\theta_1 \sim q(\theta_1|\theta_1^{(t-1)})$, conditioned on the previous state, using a symmetric proposal distribution $q(\theta_1|\theta_1^{(t-1)}) = q(\theta_1^{(t-1)}|\theta_1)$, which is a special case of the Metropolis-Hastings algorithm [22]. We accept and set $\theta_1^{(t)} = \theta_1$ with the acceptance probability

$$\alpha(\theta_1|\theta_1^{(t-1)}) = \min\left\{1, \frac{\pi(\theta_1|\theta_2^{(t-1)}, \boldsymbol{y})\, \cancel{q(\theta_1^{(t-1)}|\theta_1)}}{\pi(\theta_1^{(t-1)}|\theta_2^{(t-1)}, \boldsymbol{y})\, \cancel{q(\theta_1|\theta_1^{(t-1)})}}\right\} \tag{2.17}$$

or reject and keep $\theta_1^{(t)} = \theta_1^{(t-1)}$, which we do by comparing α to a uniform random number $u \sim \mathcal{U}(0, 1)$.

Next, we perform a Gibbs step in the θ_2 direction, where Gibbs sampling is again a special case of the Metropolis-Hastings algorithm with acceptance probability equal to one, and draw the next sample $\theta_2^{(t)} \sim \pi(\cdot|\theta_1^{(t)}, \boldsymbol{y})$, conditioned on the current value $\theta_1^{(t)}$.

We repeat this procedure N' times and ensure convergence independently of the initial sample (irreducibility) by discarding the initial $N_{\text{burn-in}}$ samples after a so-called burn-in period, resulting in a Markov chain of length $N = N' - N_{\text{burn-in}}$.

2.2.2 T-walk Sampler as a Black Box

If the parameters $\boldsymbol{x}$ are functionally dependent on the hyper-parameters $\boldsymbol{\theta}$, i.e., $\boldsymbol{x} = \boldsymbol{x}(\boldsymbol{\theta})$, we can sample directly from the marginal posterior $\pi(\boldsymbol{\theta}|\boldsymbol{y})$ using the t-walk algorithm by Christen and Fox [23]. The t-walk is employed as a black-box sampler, requiring the specification of the number of samples, burn-in period, support region, and the target distribution. Convergence to the target distribution is guaranteed by construction of the algorithm.

Algorithm 1: Metropolis within Gibbs

1: Initialise and suppose two dimensional vector $\boldsymbol{\theta}^{(0)} = (\theta_1^{(0)}, \theta_2^{(0)})$
2: **for** $k = 1, \ldots, N'$ **do**
3: Propose $\theta_1 \sim q(\cdot|\theta_1^{(t-1)}) = q(\theta_1^{(t-1)}|\cdot)$
4: Compute

$$\alpha(\theta_1|\theta_1^{(t-1)}) = \min\left\{1, \frac{\pi(\theta_1|\theta_2^{(t-1)}, \boldsymbol{y})\cancel{q(\theta_1^{(t-1)}|\theta_1)}}{\pi(\theta_1^{(t-1)}|\theta_2^{(t-1)}, \boldsymbol{y})\cancel{q(\theta_1|\theta_1^{(t-1)})}}\right\}$$

5: Draw $u \sim \mathcal{U}(0, 1)$
6: **if** $\alpha \geq u$ **then**
7: Accept and set $\theta_1^{(t)} = \theta_1$
8: **else**
9: Reject and keep $\theta_1^{(t)} = \theta_1^{(t-1)}$
10: **end if**
11: Draw $\theta_2^{(t)} \sim \pi(\cdot|\theta_1^{(t)}, \boldsymbol{y})$
12: **end for**
13: Output: $\boldsymbol{\theta}^{(0)}, \ldots, \boldsymbol{\theta}^{(k)}, \ldots, \boldsymbol{\theta}^{(N)} \sim \pi(\boldsymbol{\theta}|\boldsymbol{y})$

2.3 Numerical Approximation Methods - Tensor Train (TT)

Instead of sampling from a target distribution $\pi(\boldsymbol{x})$ we can approximate that distribution on a d-dimensional grid with far fewer function evaluation compared to sampling methods using a tensor train (TT) approximation $\tilde{\pi}(\boldsymbol{x}) \approx \pi(\boldsymbol{x})$, with $\boldsymbol{x} \in \mathbb{R}^d$. First, we provide a short overview of probability spaces and their associated measures, as a foundation for calculating marginal probability distributions from the tensor train format. Then we explain how we calculate marginal distribution and generate samples via the inverse Rosenblatt transform (IRT). Note that we follow the notation of Cui et al. [24] to introduce this methodology.

Assume that the triple $(\Omega, \mathcal{F}, \mathbb{P})$ defines a probability space, where Ω denotes the complete sample space, $\mathcal{F}$ is a σ-algebra consisting of a collection of countable subsets $\{A_n\}_{n\in\mathbb{N}}$ with $A_n \subseteq \Omega$, and $\mathbb{P}$ is a probability measure defined on $\mathcal{F}$. The formal conditions for $\mathbb{P}$ to be a probability measure, and for $\mathcal{F}$ to be a σ-algebra over Ω, are given in Appendix A.3. We denote

$$\mathbb{P}(A) = \int_A \mathrm{d}\mathbb{P} \tag{2.18}$$

as the probability of an event $A \in \mathcal{F}$. By applying the Radon-Nikodym theorem [25], we can change variables

$$\mathbb{P}(A) = \int_A \frac{\mathrm{d}\mathbb{P}}{\mathrm{d}\boldsymbol{x}}\,\mathrm{d}\boldsymbol{x} = \int_A \pi(\boldsymbol{x})\,\mathrm{d}\boldsymbol{x}, \tag{2.19}$$

where $\mathrm{d}\boldsymbol{x}$ is a reference measure on the same probability space, commonly referred to as the Lebesgue measure. The Radon-Nikodym derivative $\frac{\mathrm{d}\mathbb{P}}{\mathrm{d}\boldsymbol{x}}$ of $\mathbb{P}$ with respect to $\boldsymbol{x}$ is

often interpreted as the probability density function (PDF) $\pi(\boldsymbol{x})$. Thus, we say that $\mathbb{P}$ has a density $\pi(\boldsymbol{x})$ with respect to $\boldsymbol{x}$ [26, Chapter 10].

Now, let $X : \Omega \longrightarrow \mathbb{R}^d$ be a d-dimensional random variable mapping from the probability space $(\Omega, \mathcal{F}, \mathbb{P})$ to the measurable space $(\mathbb{R}^d, \mathcal{X})$, where $\mathcal{X}$ is a collection of subsets in $\mathbb{R}^d$. Then the associated PDF $\pi(\boldsymbol{x})$ is a joint density of X, induced by the probability measure on Ω [25, 27]. As in [24], we can define the parameter space as the Cartesian product $\mathcal{X} = \mathcal{X}_1 \times \mathcal{X}_2 \times \cdots \times \mathcal{X}_d$ with $x_k \in \mathcal{X}_k \subseteq \mathbb{R}$ and $\boldsymbol{x} = (x_1, \ldots, x_k, \ldots, x_d)$. The marginal density function for the k-th component is then given by

$$f_{X_k}(x_k) = \frac{1}{z} \int_{\mathcal{X}_1} \cdots \int_{\mathcal{X}_d} \lambda(\boldsymbol{x})\, \pi(\boldsymbol{x})\, \mathrm{d}x_1 \cdots \mathrm{d}x_{k-1}\, \mathrm{d}x_{k+1} \cdots \mathrm{d}x_d, \tag{2.20}$$

where we integrate over all dimensions except the k-th, and z is a normalisation constant. Here, we introduce a weight function $\lambda(x)$, which can be useful for quadrature rules [28], to which [24] refer to as a "product-form Lebesgue-measurable weighting function" and define it as

$$\lambda(\mathcal{X}) = \prod_{i=1}^{d} \lambda_i(\mathcal{X}_i), \quad \text{where} \quad \lambda_i(\mathcal{X}_i) = \int_{\mathcal{X}_i} \lambda_i(x_i)\, \mathrm{d}x_i. \tag{2.21}$$

In the tensor train (TT) format, the integral in Eq. 2.20 for the marginal probability can be computed at a low computational cost as $\pi(\boldsymbol{x})$ is approximated by

$$\tilde{\pi}(\boldsymbol{x}) = \tilde{\pi}_1(x_1)\tilde{\pi}_2(x_2) \cdots \tilde{\pi}_d(x_d) \in \mathbb{R},$$

which is a sequence of matrix multiplications, with $\tilde{\pi}_k(x_k) \in \mathbb{R}^{r_{k-1} \times r_k}$ for a fixed point $\boldsymbol{x} = (x_1, \ldots, x_d)$ on a predefined d-dimensional discrete univariate grid over the parameter space $\mathcal{X}$. We call $\tilde{\pi}_k \in \mathbb{R}^{r_{k-1} \times n \times r_k}$ a TT-core with ranks $r_{k-1} = r_k = r$, where the outer ranks are $r_0 = r_d = 1$, representing each dimension on n grid points and connecting to neighbouring dimensions through its ranks. This enables us to approximate $\pi(\mathcal{X}) \approx \tilde{\pi}_1 \tilde{\pi}_2 \cdots \tilde{\pi}_d$ over the whole parameter space $\mathcal{X}$ using $2nr + (d-2)nr^2$ evaluation points, as illustrated in Figure 2.2, instead of n^d function evaluation. Consequently, the marginal target distribution

$$\begin{aligned} f_{X_k}(x_k) \approx \frac{1}{z} \Big| & \left(\int_{\mathbb{R}} \lambda_1(x_1)\tilde{\pi}_1(x_1)\, \mathrm{d}x_1 \right) \cdots \left(\int_{\mathbb{R}} \lambda_{k-1}(x_{k-1})\tilde{\pi}_{k-1}(x_{k-1})\, \mathrm{d}x_{k-1} \right) \\ & \lambda_k(x_k)\tilde{\pi}_k(x_k) \\ & \left(\int_{\mathbb{R}} \lambda_{k+1}(x_{k+1})\tilde{\pi}_{k+1}(x_{k+1})\, \mathrm{d}x_{k+1} \right) \cdots \left(\int_{\mathbb{R}} \lambda_d(x_d)\tilde{\pi}_d(x_d)\, \mathrm{d}x_d \right) \Big| \end{aligned} \tag{2.22}$$

is computed by integrating over all TT cores except π_k, as in [29], including a normalisation constant z [24].

In practice, tensor train approximations may suffer from numerical instability, in particular because it is not advantageous to approximate the target function $\pi(\boldsymbol{x})$ in

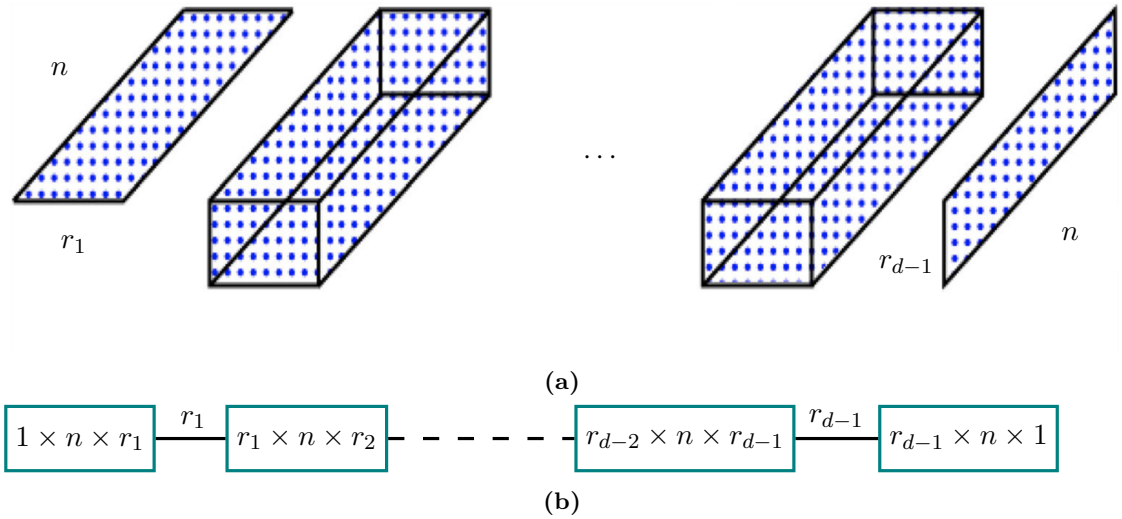

Figure 2.2: Here, we visualise the tensor train cores as two- and three-dimensional matrices. Each core has a length n, corresponding to the number of grid points in one dimension, and the cores are connected through ranks r_k. More specifically, a core $\tilde{\pi}_k$ has dimensions $r_{k-1} \times n \times r_k$, with outer ranks $r_0 = r_d = 1$. Using the TT-format enables us to represent a d-dimensional grid with only $2nr + (d-2)nr^2$ evaluation points instead of n^d grid points. Figure (a) is adapted from [30].

e.g. the logarithmic space. Hence, Cui et al. [24] approximate the square root of the probability density

$$\sqrt{\pi(\boldsymbol{x})} \approx \tilde{g}(\boldsymbol{x}) = \boldsymbol{G}_1(x_1), \dots, \boldsymbol{G}_k(x_k), \dots, \boldsymbol{G}_d(x_d)\,, \tag{2.23}$$

which ensures positivity. Here, each TT-core is given by

$$G_k^{(\alpha_{k-1},\alpha_k)}(x_k) = \sum_{i=1}^{n_k} \phi_k^{(i)}(x_k) \boldsymbol{A}_k[\alpha_{k-1}, i, \alpha_k], \quad k = 1, \dots, d, \tag{2.24}$$

where $\boldsymbol{A}_k \in \mathbb{R}^{r_{k-1} \times n_k \times r_k}$ is the k-th coefficient tensor and $\{\phi_k^{(i)}(x_k)\}_{i=1}^{n_k}$ are the basis functions corresponding to the k-th coordinate. The approximated unnormalised density is written as:

$$\pi(\boldsymbol{x}) \approx \xi + \tilde{g}(\boldsymbol{x})^2, \tag{2.25}$$

where ξ is a positive constant added according to the ratio of the Lebesgue weighted L2-norm error and the Lebesgue weighting, see Eq. 2.21, such that

$$0 \leq \xi \leq \frac{1}{\lambda(\mathcal{X})} \|\tilde{g} - \sqrt{\pi}\|^2_{L^2_\lambda(x)}. \tag{2.26}$$

This leads to the normalised target function

$$f_X(\boldsymbol{x}) \approx \frac{1}{z} \left(\lambda(\boldsymbol{x})\xi + \lambda(\boldsymbol{x})\tilde{g}(\boldsymbol{x})^2\right), \tag{2.27}$$

which is the normalisation constant $z = \int_{\mathcal{X}} f_X(\boldsymbol{x})\mathrm{d}\boldsymbol{x}$. Given the tensor train approximation of $\sqrt{\pi}$, the marginal function $f_{X_k}(x_k)$ can be expressed as

$$\begin{aligned} f_{X_k}(x_k) \approx \frac{1}{z}\Bigg(& \xi \prod_{i=1}^{k-1} \boldsymbol{\lambda}_i(\mathcal{X}_i) \prod_{i=k+1}^{d} \boldsymbol{\lambda}_i(\mathcal{X}_i) \\ & + \left(\int_{\mathbb{R}} \boldsymbol{\lambda}_1(x_1)\boldsymbol{G}_1^2(x_1)\,\mathrm{d}x_1\right) \cdots \left(\int_{\mathbb{R}} \boldsymbol{\lambda}_{k-1}(x_{k-1})\boldsymbol{G}_{k-1}^2(x_{k-1})\,\mathrm{d}x_{k-1}\right) \\ & \boldsymbol{\lambda}_k(x_k)\boldsymbol{G}_k^2(x_k) \\ & \left(\int_{\mathbb{R}} \boldsymbol{\lambda}_{k+1}(x_{k+1})\boldsymbol{G}_{k+1}^2(x_{k+1})\,\mathrm{d}x_{k+1}\right) \cdots \left(\int_{\mathbb{R}} \boldsymbol{\lambda}_d(x_d)\boldsymbol{G}_d^2(x_d)\,\mathrm{d}x_d\right)\Bigg). \end{aligned} \tag{2.28}$$

2.3.1 Marginal Functions

TT-approximations are handy when approximating integrals, as marginal functions can be easily computed which may simplify the integration significantly. We compute those by a procedure, to which Cui et al. [24] refer to as backwards marginalisation, see Prop. 2, and to which I add the forward marginalisation, see Prob. 1. This is similar to the left and right orthogonalisation of TT-cores [31, 32]. The backwards marginalisation provides us with the coefficient matrices $\boldsymbol{B}_k$, while the forward marginalisation gives the coefficient matrices $\boldsymbol{B}_{\mathrm{pre},k}$. These matrices enable the efficient evaluation of marginal functions since they integrate over the coordinates either left or right of the k-th dimension, as in [24]. In doing so, we define the mass matrix $\boldsymbol{M}_k \in \mathbb{R}^{n_k \times n_k}$ as

$$\boldsymbol{M}_k[i,j] = \int_{\mathcal{X}_k} \phi_k^{(i)}(x_k)\phi_k^{(j)}(x_k)\boldsymbol{\lambda}(x_k)\,\mathrm{d}x_k, \quad i,j = 1,\ldots,n_k, \tag{2.29}$$

where $\{\phi_k^{(i)}(x_k)\}_{i=1}^{n_k}$ denotes the set of basis functions for the k-th coordinate. The proposition used to compute $\boldsymbol{B}_k$, stated in Proposition 1, is adapted directly from [24].

Proposition 1 (Backwards Marginalisation as in [24])**:** Starting with the last coordinate $k = d$, we set $\boldsymbol{B}_d = \boldsymbol{A}_d$. The following procedure can be used to obtain the coefficient tensor $\boldsymbol{B}_{k-1} \in \mathbb{R}^{r_{k-2} \times n_{k-1} \times r_{k-1}}$, which we need for defining the marginal function $f_{X_k}(x_k)$:

1. Use the Cholesky decomposition of the mass matrix, $\boldsymbol{L}_k \boldsymbol{L}_k^\top = \boldsymbol{M}_k \in \mathbb{R}^{n_k \times n_k}$, to construct a tensor $\boldsymbol{C}_k \in \mathbb{R}^{r_{k-1} \times n_k \times r_k}$:

$$\boldsymbol{C}_k[\alpha_{k-1}, \tau, l_k] = \sum_{i=1}^{n_k} \boldsymbol{B}_k[\alpha_{k-1}, i, l_k] \boldsymbol{L}_k[i, \tau] \text{[24, Eq. ()]}. \tag{2.30}$$

2. Unfold $\boldsymbol{C}_k$ along the first coordinate and compute the thin QR decomposition, so that $\boldsymbol{C}_k^{(R)} \in \mathbb{R}^{r_{k-1} \times (n_k r_k)}$:

$$\boldsymbol{Q}_k \boldsymbol{R}_k = (\boldsymbol{C}_k^{(R)})^\top. \tag{2.31}$$

3. Compute the new coefficient tensor:

$$\boldsymbol{B}_{k-1}[\alpha_{k-2}, i, l_{k-1}] = \sum_{\alpha_{k-1}=1}^{r_{k-1}} \boldsymbol{A}_{k-1}[\alpha_{k-2}, i, \alpha_{k-1}] \boldsymbol{R}_k[l_{k-1}, \alpha_{k-1}]. \tag{2.32}$$

Proposition 2 (Forward Marginalisation)**:** Starting with the first coordinate $k = 1$, we set $\boldsymbol{B}_{\text{pre},1} = \boldsymbol{A}_1$. The following procedure can be used to obtain the coefficient tensor $\boldsymbol{B}_{\text{pre},k+1} \in \mathbb{R}^{r_k \times n_{k+1} \times r_{k+1}}$ for defining the marginal function $f_{X_k}(x_k)$:

1. Use the Cholesky decomposition of the mass matrix, $\boldsymbol{L}_k \boldsymbol{L}_k^\top = \boldsymbol{M}_k \in \mathbb{R}^{n_k \times n_k}$, to construct a tensor $\boldsymbol{C}_k \in \mathbb{R}^{r_{k-1} \times n_k \times r_k}$:

$$\boldsymbol{C}_{\text{pre},k}[\alpha_{k-1}, \tau, l_k] = \sum_{i=1}^{n_k} \boldsymbol{L}_k[i, \tau] \boldsymbol{B}_{\text{pre},k}[\alpha_{k-1}, i, l_k]. \tag{2.33}$$

2. Unfold $\boldsymbol{C}_{\text{pre},k}$ along the first coordinate and compute the thin QR decomposition, so that $\boldsymbol{C}_{\text{pre},k}^{(R)} \in \mathbb{R}^{(r_{k-1} n_k) \times r_k}$:

$$\boldsymbol{Q}_{pre,k} \boldsymbol{R}_{\text{pre},k} = (\boldsymbol{C}_{\text{pre},k}^{(R)}). \tag{2.34}$$

3. Compute the new coefficient tensor $\boldsymbol{B}_{\text{pre},k+1} \in \mathbb{R}^{r_{k-1} \times n_k \times r_k}$:

$$\boldsymbol{B}_{\text{pre},k+1}[l_{k+1}, i, \alpha_{k+1}] = \sum_{\alpha_k=1}^{r_k} \boldsymbol{R}_{\text{pre},k}[l_{k+1}, \alpha_k] \boldsymbol{A}_{k+1}[\alpha_k, i, \alpha_{k+1}]. \tag{2.35}$$

After computing the coefficient tensors $\boldsymbol{B}_{\text{pre},k+1}$ as in Prop. 2 and $\boldsymbol{B}_{k+1}$ from Prop. 1, the marginal PDF of k-th dimension can be expressed as

$$f_{X_k}(x_k) \approx \frac{1}{z} \left(\xi \prod_{i=1}^{k-1} \lambda_i(X_i) \prod_{i=k+1}^{d} \lambda_i(X_i) + \sum_{l_{k-1}=1}^{r_{k-1}} \sum_{l_k=1}^{r_k} \left(\sum_{i=1}^{n} \phi_k^{(i)}(x_k) \boldsymbol{D}_k[l_{k-1}, i, l_k] \right)^2 \right) \lambda_k(x_k), \tag{2.36}$$

where $\boldsymbol{D}_k \in \mathbb{R}^{r_{k-1}\times n\times r_k}$ and $\boldsymbol{R}_{\text{pre},k-1} \in \mathbb{R}^{r_{k-1}\times r_{k-1}}$ and $\boldsymbol{B}_k \in \mathbb{R}^{r_{k-1}\times n\times r_k}$

$$\boldsymbol{D}_k[l_{k-1}, i, l_k] = \sum_{\alpha_{k-1}=1}^{r_{k-1}} \boldsymbol{R}_{\text{pre},k-1}[l_{k-1}, \alpha_{k-1}]\boldsymbol{B}_k[\alpha_{k-1}, i, l_k]. \tag{2.37}$$

For the first dimension, $f_{X_1}(x_1)$ can be expressed as

$$f_{X_1}(x_1) \approx \frac{1}{z}\left(\xi \prod_{i=2}^{d} \lambda_i(\mathcal{X}_i) + \sum_{l_1=1}^{r_1}\left(\sum_{i=1}^{n} \phi_1^{(i)}(x_1)\boldsymbol{D}_1[i, l_1]\right)^2\right)\lambda_1(x_1), \tag{2.38}$$

where $\boldsymbol{D}_1[i, l_1] = \boldsymbol{B}_1[\alpha_0, i, l_1]$ and $\alpha_0 = 1$, and similarly in the last dimension

$$f_{X_d}(x_d) \approx \frac{1}{z}\left(\xi \prod_{i=1}^{d-1} \lambda_i(\mathcal{X}_i) + \sum_{l_{n-1}=1}^{r_{d-1}}\left(\sum_{i=1}^{n} \phi_1^{(i)}(x_1)\boldsymbol{D}_d[l_{n-1}, i]\right)^2\right)\lambda_d(x_d), \tag{2.39}$$

where $\boldsymbol{D}_d[l_{n-1}, i] = \boldsymbol{B}_{\text{pre},d}[l_{n-1}, i, \alpha_{n+1}]$ and $\alpha_{d+1} = 1$. Note that we calculate the normalisation numerically within the process of finding the marginals so that $\sum f_{X_k}(x_k) = 1$.

2.3.2 Sampling from the TT Approximation

If instead of evaluating integrals we like to draw samples from the approximated function we do this via the inverse Rosenblatt transform (IRT), as in [29], to preserve the correlation structure. Since we approximate the square root of the target function, Cui et. al. [24] call that the squared inverse Rosenblatt transform (SIRT).

Algorithm 2: Squared Inverse Rosenblatt Transform (SIRT)

Input: seeds $\{\boldsymbol{u}^{(1)}, \ldots, \boldsymbol{u}^{(N)}\} \sim \mathcal{U}(0,1)^d$ and $\boldsymbol{B}_1, \ldots, \boldsymbol{B}_d$ from Prob. 1
for $s = 1, \ldots, N$ **do**
  for $k = 1, \ldots, d$ **do**
    compute normalised PDF $f_{X_k|X_{<k}}(x_k|x_{k-1}^{(s)}, \ldots, x_1^{(s)})$, Eq. 2.42
    compute cumulative distribution function $F_{X_k}(x_k)$, Eq. 2.40
    project sample $x_k^{(s)} = F_{X_k}^{-1}(u_k^{(s)})$
    interpolate $\boldsymbol{G}_k(x_k^{(s)})$, Eq. 2.41
    update $\boldsymbol{G}_{\leq k}(x_{\leq k}^{(s)}) = \boldsymbol{G}_{<k}(x_{<k}^{(s)})\boldsymbol{G}_k(x_k^{(s)})$
  end for
end for
Output: samples $\{\boldsymbol{x}^{(1)}, \ldots, \boldsymbol{x}^{(N)}\}$, where each $\boldsymbol{x}^{(s)} \in \mathbb{R}^d$ for $s = 1, \ldots, N$

We start by calculating the Backward marginals $\boldsymbol{B}_1, \ldots, \boldsymbol{B}_d$ as in Prob 1 and draw N uniformly distributed seeds $\{\boldsymbol{u}^{(1)}, \ldots, \boldsymbol{u}^{(N)}\} \sim \mathcal{U}(0,1)^d$, where each $\boldsymbol{u}^{(s)}$ is d-dimensional for $s = 1, \ldots, N$. Then we calculate the first marginal $f_{X_1}(x_1)$ as in Eq. 2.38 and normalise with $z = \int_{\mathcal{X}_1} f_{X_1}(x_1)dx_1$. Next, we compute the cumulative distribution function (CDF)

$$F_{X_k}(x_k) \approx \int_{-\infty}^{x_k} f_{X_k|X_{<k}}(\tilde{x}_k|x_{k-1}, \ldots, x_1)d\tilde{x}_k \tag{2.40}$$

for the first dimension $k = 1$ and then project the seed on the parameter space $x_k^{(s)} = F_{X_k}^{-1}(u_k^{(s)})$. Once that is done, we use a piecewise polynomial interpolation

$$\boldsymbol{G}_k(x_k^{(s)}) \approx \frac{x_k^{(s)} - x_k^{(i)}}{x_k^{(i+1)} - x_k^{(i)}} \boldsymbol{G}_k(x_k^{(i+1)}) + \frac{x_k^{(i+1)} - x_k^{(s)}}{x_k^{(i+1)} - x_k^{(i)}} \boldsymbol{G}_k(x_k^{(i)}) \tag{2.41}$$

for $x_k^{(i)} \leq x_k^{(s)} \leq x_k^{(i+1)}$ in between two grid points i and $i+1$ as in [29]. Through $\boldsymbol{G}_k(x_k^{(s)}) \in \mathbb{R}^{1 \times r_{k-1}}$ we condition on the previous samples, which denotes the product of all approximated tensors of the previous $k-1$ samples to preserve the correlation structure. Then we marginalise over the dimensions $k+1, \ldots, d$ via $\boldsymbol{B}_k$ so that the next "conditional marginal" is given as:

$$f_{X_k|X_{<k}}(x_k|x_{k-1}^{(s)}, \ldots, x_1^{(s)}) \approx \frac{1}{z}\Bigg(\xi \prod_{i=1}^{k-1} \boldsymbol{\lambda}_i(X_i) \prod_{i=k+1}^{d} \boldsymbol{\lambda}_i(X_i) + \sum_{l_k=1}^{r_k} \Bigg(\sum_{i=1}^{n} \phi_k^{(i)}(x_k^{(s)}) \Bigg(\sum_{\alpha_{k-1}=1}^{r_{k-1}} \boldsymbol{G}_{<k}^{(\alpha_{k-1})}(x_{<k}^{(s)}) \boldsymbol{B}_k[\alpha_{k-1}, i, l_k] \Bigg) \Bigg)^2 \Bigg) \boldsymbol{\lambda}_k(x_k) \tag{2.42}$$

We repeat the procedure for each $u_k^{(s)} \in \boldsymbol{u}^{(s)}$ to gain samples $\boldsymbol{x}^{(s)} \sim f_X(x)$, see algorithmic box 3 for a summarised version.

MH - correction step

Algorithm 3: MH correction step

Input: samples $\{\boldsymbol{x}^{(1)}, \ldots, \boldsymbol{x}^{(N+1)}\}$, where each $\boldsymbol{x}^{(s)} \in \mathbb{R}^d$ for $s = 1, \ldots, N+1$
for $s = 1, \ldots, N$ **do**
  compute MH ratio $\frac{w^{(s+1)}}{w^{(s)}} = \frac{\pi(\boldsymbol{x}^{(s+1)})}{\pi(\boldsymbol{x}^{(s)})} \frac{f_X(\boldsymbol{x}^{(s)})}{f_X(\boldsymbol{x}^{(s+1)})}$
  compute acceptance probability $\alpha = \min(w^{(s+1)}/w^{(s)}, 1)$
  Draw $u \sim \mathcal{U}(0,1)$
  if $\alpha \geq u$ **then**
    Accept and set $\boldsymbol{x}_{\text{MH}}^{(s+1)} = \boldsymbol{x}^{(s+1)}$
  else
    Reject and keep $\boldsymbol{x}_{\text{MH}}^{(s+1)} = \boldsymbol{x}^{(s)}$
  end if
end for
Output: corrected sample chain $\{\boldsymbol{x}_{\text{MH}}^{(1)}, \ldots, \boldsymbol{x}_{\text{MH}}^{(N)}\}$, where each $\boldsymbol{x}_{\text{MH}}^{(s)} \in \mathbb{R}^d$ for $s = 1, \ldots, N$

Since the samples using the SIRT scheme are samples from an approximation it is sensible to correct those using a Metropolis-Hastings importance sampler. In doing so we compute the acceptance probability $\alpha = \min(w^{(s+1)}/w^{(s)}, 1)$, where

$$w(x) = \frac{\pi(\boldsymbol{x})}{f_X(\boldsymbol{x})} = \frac{\pi(\boldsymbol{x})}{\gamma + \tilde{g}(\boldsymbol{x})^2} \tag{2.43}$$

is the importance ratio. In practise we calculate the importance ratio in the log space, where $\log f_X(\boldsymbol{x}) = \log f_{X_1}(x_1) + \log f_{X_2|X_1}(x_2|x_1) + \cdots + \log f_{X_k|X_{<k}}(x_k|x_{k-1}, \ldots, x_1)$ is given as in Eq. 2.42. This leads to the corrected chain $\{\boldsymbol{x}_{\mathrm{MH}}^{(1)}, \ldots, \boldsymbol{x}_{\mathrm{MH}}^{(N)}\} \sim \pi(\boldsymbol{x})$.

2.3.3 On the Error in the TT Approximation

A straight forward way to asses the error from the TT approximation is to calculate the relative root mean squared error

$$\left(\frac{\int_{\mathcal{X}}(\pi(\boldsymbol{x}) - (\gamma + \tilde{g}(\boldsymbol{x})^2))^2 \boldsymbol{\lambda}(\boldsymbol{x})\mathrm{d}\boldsymbol{x}}{\int_{\mathcal{X}} \pi(\boldsymbol{x})^2 \boldsymbol{\lambda}(x)\mathrm{d}\boldsymbol{x}}\right)^{1/2} = \frac{\|\pi(\boldsymbol{x}) - (\gamma + \tilde{g}(\boldsymbol{x})^2)\|_{L^2_{\boldsymbol{\lambda}}(\mathcal{X})}}{\|\pi(\boldsymbol{x})\|_{L^2_{\boldsymbol{\lambda}}(\mathcal{X})}}. \tag{2.44}$$

We can approximate the this integral as

$$\left(\frac{1}{N}\sum_{i=1}^{N}\left(\pi(\boldsymbol{x}^{(i)}) - (\gamma + \tilde{g}(\boldsymbol{x}^{(i)})^2)\right)^2 \boldsymbol{\lambda}(\boldsymbol{x})\right)^{1/2} \approx \left(\int_{\mathcal{X}}\left(\pi(\boldsymbol{x}) - (\gamma + \tilde{g}(\boldsymbol{x})^2)\right)^2 \boldsymbol{\lambda}(x)\mathrm{d}\boldsymbol{x}\right)^{1/2} \tag{2.45}$$

and similarly $\int_{\mathcal{X}} \pi(\boldsymbol{x})^2 \boldsymbol{\lambda}(\boldsymbol{x})\mathrm{d}\boldsymbol{x}$.

Absolute Error Bound

One way to assess the error between two distributions is to calculate the Wasserstein distance, because the Kantorovich-Rubinstein duality, as in [33, 34], says that the 1-Wasserstein distance is equal to the upper bound of differences in expectations of a function h between two probability distributions.

We define the 1-Wasserstein distance as

$$W_1(\pi, \tilde{\pi}) = \inf_{\nu \in \Pi(\pi, \tilde{\pi})} \int_{\mathcal{X}\times\mathcal{X}} c(\boldsymbol{x}, \tilde{\boldsymbol{x}})\, \nu(\boldsymbol{x}, \tilde{\boldsymbol{x}}) d\boldsymbol{x} d\tilde{\boldsymbol{x}}\,, \tag{2.46}$$

where ν couples $\boldsymbol{x}$ and $\tilde{\boldsymbol{x}}$ so that the integral over the distance $c(\boldsymbol{x}, \tilde{\boldsymbol{x}})$ weighted by the probability measures π and $\tilde{\pi}$ is the greatest lower bound of all integrals with respect to a ν in the set of all couplings $\Pi(\pi, \tilde{\pi})$. Often ν is called a transport plan, where $c(\boldsymbol{x}, \tilde{\boldsymbol{x}})$ is the (ground) cost function, and $\nu(\boldsymbol{x}, \tilde{\boldsymbol{x}})$ is related to the mass which has to be transported and the 1-Wasserstein distance is the earth mover distance. On the other hand (Kantorovich-Rubinstein duality), we can describe the 1-Wasserstein distance

$$W_1(\pi, \tilde{\pi}) = \sup_{\|h(\boldsymbol{x}) - h(\tilde{\boldsymbol{x}})\|_{L^2} \leq \|\boldsymbol{x} - \tilde{\boldsymbol{x}}\|_{L^2}} \left\{ \int_{\mathcal{X}} h(\boldsymbol{x}) d\pi(\boldsymbol{x}) - \int_{\mathcal{X}} h(\tilde{\boldsymbol{x}}) d\tilde{\pi}(\tilde{\boldsymbol{x}}) \right\} \tag{2.47}$$

$$= \sup_{\|h(\boldsymbol{x}) - h(\tilde{\boldsymbol{x}})\|_{L^2} \leq \|\boldsymbol{x} - \tilde{\boldsymbol{x}}\|_{L^2}} \left\{ \mathop{\mathbb{E}}_{\boldsymbol{x}\sim\pi}\left[h(\boldsymbol{x})\right] - \mathop{\mathbb{E}}_{\tilde{\boldsymbol{x}}\sim\tilde{\pi}}\left[h(\tilde{\boldsymbol{x}})\right] \right\}. \tag{2.48}$$

as the lowest upper bound of differences in expecations of the 1-Lipschitz function h in between the two distributions π and $\tilde{\pi}$, with distance measure $c(\boldsymbol{x}, \tilde{\boldsymbol{x}}) = \|\boldsymbol{x} - \tilde{\boldsymbol{x}}\|_{L^2}$

for $\mathcal{X} \in \mathbb{R}^d$. For two sample sets $\{\boldsymbol{x}^{(1)}, \dots, \boldsymbol{x}^{(N)}\} \sim \pi$ and $\{\tilde{\boldsymbol{x}}^{(1)}, \dots, \tilde{\boldsymbol{x}}^{(M)}\} \sim \tilde{\pi}$ the calculation of the Wasserstein distance becomes an optimisation problem, that is to find the best permutation (order) of samples weighted by their distribution value according to an appropriate distance measure [35]. This gives us an upper bound of the absolute error in between the expected value of any 1-Lipschitz function h, e.g the upper bound of absolute differences in means of π and $\tilde{\pi}$.

2.4 Affine Map

The forward map, which we introduce in Ch. 3, poses a weakly non-linear forward problem, which we could tackle by treating the problem as a linear problem and then iteratively updating the non-linear part after each parameter sample. Instead, we approximate the non-linear model using an affine map $\boldsymbol{M} : \boldsymbol{A}_L \to \boldsymbol{A}_{NL}$, which maps from the linear model to the non-linear model, so that we set $\boldsymbol{A} = \boldsymbol{M}\boldsymbol{A}_{NL} \approx \boldsymbol{A}_{NL}$. Here, we give a brief introduction to affine maps and present our approach to calculating the affine map deterministically. Alternatively, one can also determine this map using other methods, e.g. machine learning methods or matrix inversion [].

An affine map is any linear map between two vector spaces or affine spaces, where an affine space does not need to preserve a zero origin, see [36, Def. 2.3.1]. In other words, an affine map does not need to map to the origin of the associated vector space or be a linear map on vector spaces, including a translation, or, in the words of my supervisor, C. F., an affine map is a Taylor series of first order. For more information on affine spaces and maps, we refer to the books [36, 37]

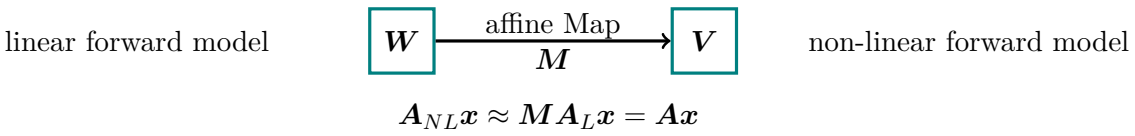

$$\boldsymbol{A}_{NL}\boldsymbol{x} \approx \boldsymbol{M}\boldsymbol{A}_L\boldsymbol{x} = \boldsymbol{A}\boldsymbol{x}$$

Figure 2.3: This Figure shows the schematic representation of the affine map $\boldsymbol{M}$, which approximates the non-linear forward model from the linear forward model. Here, V contains values produced by the linear forward model, and W contains the corresponding values from the non-linear forward model. Both V and W are affine subspaces over the same field. The affine map $\boldsymbol{M}$ projects elements from the linear forward model space V onto their counterparts in the non-linear forward model space W.

Consequently, to map between the linear and non-linear forward map, we generate two affine subspaces $\boldsymbol{V}$ and $\boldsymbol{W}$ over the same field. Assume we draw samples $\{\boldsymbol{x}^{(1)}, \dots, \boldsymbol{x}^{(j)}, \dots, \boldsymbol{x}^{(m)}\} \sim \pi(\boldsymbol{x}|\boldsymbol{y})$ then the affine subspace associated with the linear forward model is

$$\boldsymbol{W} = \begin{bmatrix} | & & | & & | \\ \boldsymbol{A}_L\boldsymbol{x}^{(1)} & \cdots & \boldsymbol{A}_L\boldsymbol{x}^{(j)} & \cdots & \boldsymbol{A}_L\boldsymbol{x}^{(m)} \\ | & & | & & | \end{bmatrix} \in \mathbb{R}^{m \times m} \tag{2.49}$$

and with the non-linear forward model is

$$\boldsymbol{V} = \begin{bmatrix} | & & | & & | \\ \boldsymbol{A}_{NL}\boldsymbol{x}^{(1)} & \cdots & \boldsymbol{A}_{NL}\boldsymbol{x}^{(j)} & \cdots & \boldsymbol{A}_{NL}\boldsymbol{x}^{(m)} \\ | & & | & & | \end{bmatrix} = \begin{bmatrix} — & v_1 & — \\ & \vdots & \\ — & v_j & — \\ & \vdots & \\ — & v_m & — \end{bmatrix} \in \mathbb{R}^{m\times m}. \tag{2.50}$$

Then the affine map

$$\boldsymbol{V}\boldsymbol{W}^{-1} = \boldsymbol{M} = \begin{bmatrix} — & r_0 & — \\ & \vdots & \\ — & r_j & — \\ & \vdots & \\ — & r_m & — \end{bmatrix} \in \mathbb{R}^{m\times m}, \tag{2.51}$$

can be found by either matrix inversion of $\boldsymbol{W}$ or alternatively if the noise free data points in $\boldsymbol{A}_{NL}\boldsymbol{x}^{(j)}$ are independent of each other by row wise by solving $v_j = r_j\boldsymbol{W}$ for r_j.

2.5 Regularisation

As mentioned in the introduction, the currently most used method to analyse data in atmospheric physics is regularisation-based. Since we want to show that our methods are computationally comparable if not faster, and provide more information than regularisation, we choose a linear-Gaussian Bayesian framework closest to our regulariser, see section 4.2.

The Tikhonov regularisation approach provides one solution $\boldsymbol{x}_\lambda$ that minimises both the data misfit norm

$$\|\boldsymbol{y} - \boldsymbol{A}\boldsymbol{x}\| \tag{2.52}$$

and a regularisation semi-norm

$$\lambda \|\boldsymbol{T}\boldsymbol{x}\| , \tag{2.53}$$

for a given regularisation parameter $\lambda > 0$ as described in [12], with a linear forward model matrix $\boldsymbol{A}$, the data $\boldsymbol{y}$, a regularisation operator $\boldsymbol{T}$. The regularisation parameter weights the semi-norm and penalises $\boldsymbol{x}$ according to that. If λ is large, then the effect of the data on the solution $\boldsymbol{x}_\lambda$ is small or negligible. If λ is small, the solution $\boldsymbol{x}_\lambda$ will be dominated by the noisy data, resulting in an overfitted $\boldsymbol{x}_\lambda$. We refer to [38] and [7] for a more comprehensive analysis of the effects of the regularisation parameter on the solution, e.g. due to small singular values of the forward model.

For a fixed λ, the regularised solution

$$\boldsymbol{x}_\lambda = \arg\min_{\boldsymbol{x}} \|\boldsymbol{y} - \boldsymbol{A}\boldsymbol{x}\|^2 + \lambda \|\boldsymbol{T}\boldsymbol{x}\|^2 \tag{2.54}$$

is obtained by taking the derivative with respect to $\boldsymbol{x}$:

$$\nabla_{\boldsymbol{x}} \left\{ (\boldsymbol{y} - \boldsymbol{A}\boldsymbol{x})^T (\boldsymbol{y} - \boldsymbol{A}\boldsymbol{x}) + \lambda \boldsymbol{x}^T \boldsymbol{T}^T \boldsymbol{T}\boldsymbol{x} \right\} = 0 \tag{2.55}$$

$$\iff \quad \nabla_{\boldsymbol{x}} \left\{ \boldsymbol{y}^T\boldsymbol{y} + \boldsymbol{x}^T \boldsymbol{A}^T \boldsymbol{A}\boldsymbol{x} - 2\boldsymbol{y}^T \boldsymbol{A}\boldsymbol{x} + \lambda \boldsymbol{x}^T \boldsymbol{T}^T \boldsymbol{T}\boldsymbol{x} \right\} = 0 \tag{2.56}$$

$$\iff \quad 2\boldsymbol{A}^T\boldsymbol{A}\boldsymbol{x} - 2\boldsymbol{A}^T\boldsymbol{y} + 2\lambda \boldsymbol{T}^T\boldsymbol{T}\boldsymbol{x} = 0, \tag{2.57}$$

also know as the "regularised normal equations" $\boldsymbol{A}^T\boldsymbol{y} = \boldsymbol{A}^T\boldsymbol{A}\boldsymbol{x} + \lambda \boldsymbol{T}^T\boldsymbol{T}\boldsymbol{x}$ [39]. Solving this equation yields the regularised solution

$$\boldsymbol{x}_\lambda = (\boldsymbol{A}^T\boldsymbol{A} + \lambda \boldsymbol{L})^{-1} \boldsymbol{A}^T\boldsymbol{y}\,, \tag{2.58}$$

where we define $\boldsymbol{L} \coloneqq \boldsymbol{T}^T\boldsymbol{T}$, which typically represents a discrete matrix approximation of a differential operator choice [7]. For example

$$\boldsymbol{T} = \frac{1}{h} \begin{bmatrix} -1 & 1 & & & \\ 0 & -1 & 1 & & \\ & \ddots & \ddots & \ddots & \\ & & 0 & -1 & 1 \\ & & & 0 & -1 \end{bmatrix} \tag{2.59}$$

is the first order derivative with equal spacing h as in [7] then

$$\boldsymbol{L} = \frac{1}{h^2} \begin{bmatrix} 1 & -1 & & & \\ -1 & 2 & -1 & & \\ & \ddots & \ddots & \ddots & \\ & & -1 & 2 & -1 \\ & & & -1 & 2 \end{bmatrix} \tag{2.60}$$

is the second order derivative with Neumann boundary conditions, see [40].

In practice, $\boldsymbol{x}_\lambda$ is computed for a range of λ-values and evaluated based on the trade-off between the data misfit and the regularisation semi-norm. The optimal value of λ corresponds to the point of maximum curvature of the so-called L-curve [41], where the data misfit norm versus the regularisation semi-norm is plotted, see Fig. 4.14.

Additionally one can think about regularisation as a Lagrange multiplier $\mathcal{L}(\boldsymbol{x}, \lambda) :- \lambda \boldsymbol{x}^T\boldsymbol{L}\boldsymbol{x} + \|\boldsymbol{y} - \boldsymbol{A}\boldsymbol{x}\|$, which minimises $\boldsymbol{x}_\lambda = \arg\min_{\boldsymbol{x}} \boldsymbol{x}^T\boldsymbol{L}\boldsymbol{x}$ with respect to a constant $\|\boldsymbol{y} - \boldsymbol{A}\boldsymbol{x}\|$, see [12, fn. 6] and [42, Fig. 2.13]. So every solution $\boldsymbol{x}_\lambda$ is an extremum (the most regularised solution for a given data misfit norm) and almost every sample of the posterior, which represents a feasible solution given the data, has a higher $\boldsymbol{x}^T\boldsymbol{L}\boldsymbol{x}$ value and lays above the L-Curve.

3
Forward Model

In this chapter, we present the forward model on which we apply all our methodology. We follow the Michelson Interferometer for Passive Atmospheric Sounding (MIPAS) handbook [43] and simulate data according to a cloud-free atmosphere in local thermodynamic equilibrium and assume a measurement instrument with infinite spectral resolution and no pointing errors.

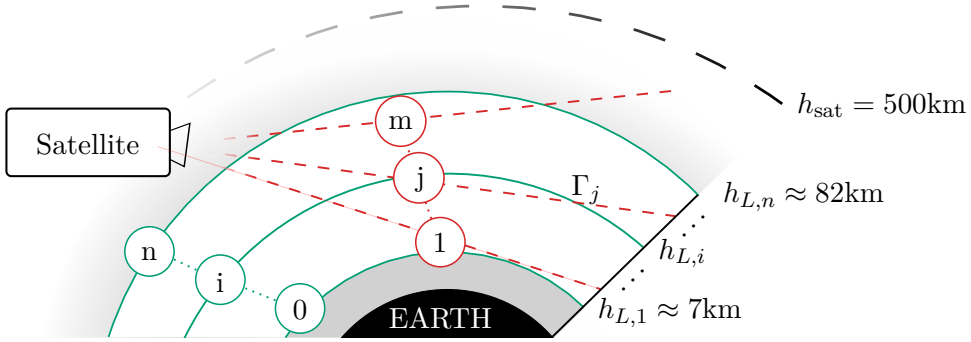

Figure 3.1: Schematic of measurement and analysis geometry, not to scale. The stationary satellite, at a constant height h_{sat} above Earth, takes $m = 30$ measurements along its line-of-sight defined by the line Γ_j. Each measurement has a limb height ℓ_j, $j = 1, 2, \ldots, m$ defined as the closest distance of Γ_j to the Earth's surface. Between $h_{L,0} \approx 7$km and $h_{L,n} \approx 82$km, the stratosphere is discretised into $n = 34$ layers as illustrated by the solid green lines.

A satellite at a constant height h_{sat} points through the atmosphere (limb-sounding) and measures thermal radiation of gas molecules along its straight line of sight Γ_j, see Figure 3.1. One measurement of the thermal radiation of one specific molecule, in our case ozone, denoted by the ozone volume mixing ratio (VMR) $x(r)$ at distance r from

the satellite, at the wave number ν, is given by the path integral

$$y_j = \int_{\Gamma_j} B(\nu, T) k(\nu, T) \frac{p(T)}{k_{\mathrm{B}} T(r)} x(r) \tau(r) \mathrm{d}r + \eta_j \tag{3.1}$$

$$\tau(r) = \exp\Big\{ - \int_{r_{\mathrm{obs}}}^{r} k(\nu, T) \frac{p(T)}{k_B T(r')} x(r') \mathrm{d}r' \Big\}, \tag{3.2}$$

which is the radiative transfer equation (RTE) [43]. For more information on the processes within the atmosphere for ozone, we refer to [44]. We define a tangent height h_{ℓ_j} and Γ_j for each $j = 1, 2, \ldots, m$, so that the data vector $\boldsymbol{y} \in \mathbb{R}^m$ including some noise η_j. Within the atmosphere, the number density $p(T)/(k_{\mathrm{B}} T(r))$ of molecules is dependent on the pressure $p(T)$, the temperature $T(r)$, and the Boltzmann constant k_{B}. The factor $\tau(r) \leq 1$ accounts for re-absorption of the radiation along the line-of-sight, which makes the RTE non-linear. The absorption constant

$$k(\nu, T) = L(\nu, T_{\mathrm{ref}}) \frac{Q(T_{\mathrm{ref}})}{Q(T)} \frac{\exp\{-c_2 E''/T\}}{\exp\{-c_2 E''/T_{\mathrm{ref}}\}} \frac{1 - \exp\{-c_2 \nu / T\}}{1 - \exp\{-c_2 \nu / T_{\mathrm{ref}}\}} \tag{3.3}$$

is dependent on the line intensity $L(\nu, T_{\mathrm{ref}})$ at reference temperature $T_{\mathrm{ref}} = 296K$, the lower-state energy of the transition E'', the second radiation constant $c2 = 1.4387769\mathrm{cmK}$ all provided by the HITRAN database [45]. Since we assume that the measurement deceive has negligible frequency window we neglect line broadening around ν_0 for the calculations of $L(\nu, T_{\mathrm{ref}})$, which would normally be modelled as a convolution of the normalised Lorentz profile (collisional/pressure broadening) and the normalised Doppler (thermal broadening) profile [43]. Additionally, since we target one specific molecule, we simplify the calculation of $k(\nu, T)$, which usually involves summing the individual absorption constants for each targeted molecule weighted by the respective volume mixing ratio [43]. The total internal partition function for the lower-state energy is given as:

$$Q(T) = g'' \exp\{-\frac{c_2 E''}{T}\}, \tag{3.4}$$

with the statistical weight g'' (also called the degeneracy factor) accounting for the molecule's non-rotational and rotational energy states, see [46]. Under the assumption of local thermodynamic equilibrium (LTE), the black body radiation acts as a source function

$$B(\nu, T) = \frac{2hc^2\nu^3}{\exp\{\frac{hc\nu}{k_B T}\} - 1}, \tag{3.5}$$

with Planck's constant h and velocity of light c. For fundamentals on the Radiative transfer equation we recommend [47, Chapter 1], and for a more comprehensive model we refer to [48]

To enable matrix-vector multiplication, we discretise the atmosphere in n layers, where the i^{th} layer is defined by two spheres of radii $h_{L,i-1} < h_{L,i}$, for $i = 1, \ldots, n$, with $h_{L,0}$ and

$h_{L,n}$. Then we can discretise the ozone, pressure and temperature profiles as a function of height, where in between the heights $h_{L,i-1}$ and $h_{L,i}$, each of the ozone concentration x_i, the pressure p_i, the temperature T_i, as well as all other height dependent parameters are assumed to be constant. Above $h_{L,n}$ and below $h_{L,0}$, the ozone concentration is set to zero, so no signal can be obtained. Depending on the parameter of interest, which is either the ozone volume mixing ratio $\boldsymbol{x} = \{x_1, x_2, \ldots, x_n\} \in \mathbb{R}^n$ or the fraction of pressure and temperature $\boldsymbol{p/T} = \{p_1/T_1, p_2/T_2, \ldots, p_n/T_n\} \in \mathbb{R}^n$ we rewrite the integral in Eq. (3.1) for one noise free measurement, using the trapezoidal rule, as a vector-vector multiplication $\boldsymbol{A_j}(\boldsymbol{x}, \boldsymbol{p}, \boldsymbol{T})\,\boldsymbol{x}$ or $\boldsymbol{A_j}(\boldsymbol{x}, \boldsymbol{p}, \boldsymbol{T})\,\boldsymbol{p/T}$, where the non-linear absorption $\tau(r)$ is included in $\boldsymbol{A_j}(\boldsymbol{x}, \boldsymbol{p}, \boldsymbol{T}) \in \mathbb{R}^n$ which is the j-th row of the matrix $\boldsymbol{A}(\boldsymbol{x}, \boldsymbol{p}, \boldsymbol{T})$. Then given a noise vector $\boldsymbol{\eta} \in \mathbb{R}^m$ the data vector

$$\boldsymbol{y} = \boldsymbol{A}_{NL}\,\boldsymbol{x} + \boldsymbol{\eta} = \boldsymbol{A}_{NL}\,\frac{\boldsymbol{p}}{\boldsymbol{T}} + \boldsymbol{\eta} \tag{3.6}$$

is based on a matrix-vector multiplication. Here we define the non-linear forward model matrix as $\boldsymbol{A}_{NL} \coloneqq \boldsymbol{A}(\boldsymbol{x}, \boldsymbol{p}, \boldsymbol{T}) \in \mathbb{R}^{m \times n}$ for simplicity, so that $\boldsymbol{A}_{NL}\boldsymbol{x}$ or $\boldsymbol{A}_{NL}\boldsymbol{p/T}$ implies the construction of $\boldsymbol{A}_{NL}$ and similarly for $\boldsymbol{A}_L$, which denotes the linear forward model matrix and neglects abortion (e.g. set $\tau = 1$ in Eq. (3.2)). Further, we classify the inverse problem as weakly non-linear, see e.g. Fig. 4.13, as neglecting the absorption changes the measurements only slightly.

3.1 Singular Value Decomposition of the Forward Model

Before simulating some data, we provide a quick and intuitive way of assessing if the data collection is effective, how much information is passed through the forward model, depending on how we measure and how the signal-to-noise ratio affects that information. One way of doing this is via a singular value decomposition (SVD) of the forward model matrix

$$\boldsymbol{A} = \sum_{i=1}^{r} \boldsymbol{u}_i \sigma_i \boldsymbol{v}_i^T = \boldsymbol{U}\boldsymbol{\Sigma}\boldsymbol{V}^T \tag{3.7}$$

where $r = \min\{m, n\}$ for a forward model $\boldsymbol{A} \in \mathbb{R}^{m \times n}$. Consider noise free measurements $\boldsymbol{Ax}$ for a satellite at a fixed height of $h_{\text{sat}} = 500\text{km}$ above sea level, where $\boldsymbol{x}$ is the ozone VMR, then the SVD gives us information on how information is picked up from the parameter space by the forward model, described through the right singular values $\boldsymbol{v}_i$. The singular values σ_i, ordered in size from the largest σ_1 to the smallest σ_r, weight that information from the right singular values to the left singular values $\boldsymbol{u}_i$, which project onto the data space. If we have lots of high-valued singular values, we can say that the

forward model is informative and vice versa. The right singular vectors indicate which structures of the parameter space are picked up by the model.

Further, for very small singular values $\sigma_i \ll \sigma_1/\text{SNR}$ below the root mean square (rms) noise level or the noise standard deviation (std.), we can introduce an effective rank $r_{\text{eff}} \leq r$. Then information of parameter space spanned by $\{\boldsymbol{v}_{r_{\text{eff}}+1}, \ldots, \boldsymbol{v}_r\}$ is not passed through the forward model and the data is noise dominated in the corresponding data space, see Figure 3.6. This is based on the rough assumption that if we define the signal-to-noise ratio (SNR) as

$$\text{SNR} := \frac{\max(y)}{\text{std. noise}} = \frac{\text{peak signal}}{\text{rms noise}} \text{[49]} \tag{3.8}$$

then the maximum singular value $\max(y) \approx \sigma_1$ and the information transmitted through the forward model corresponds roughly to the singular values $\sigma_i \gtrsim \max(y)/\text{SNR}$. See [7] for a more comprehensive analysis.

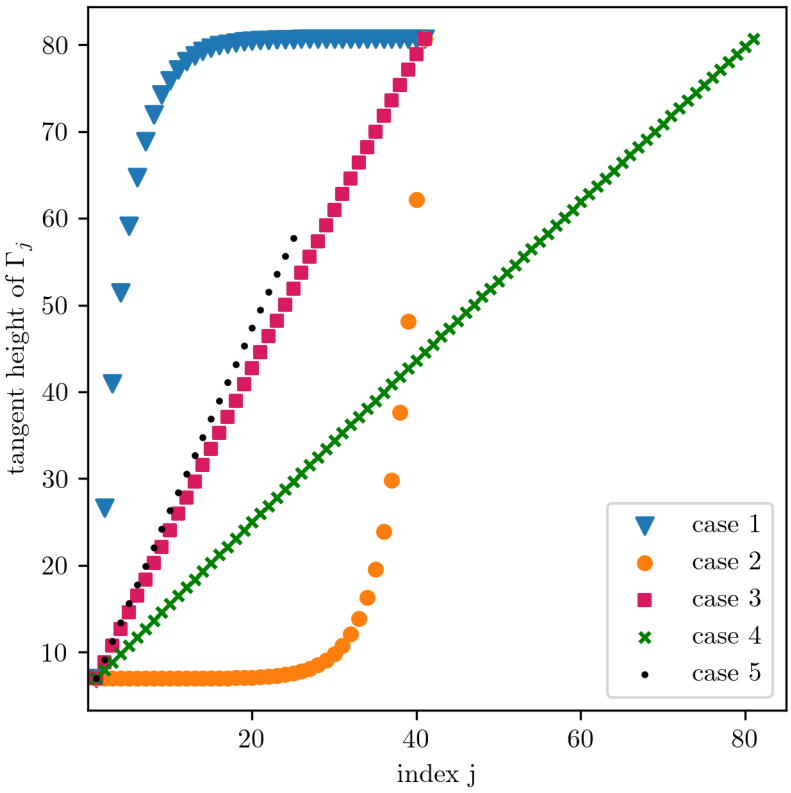

Figure 3.2: We plot the tangent heights for different cases of measurements.

Next, we plot the singular values for 5 different measurement scenarios, where we either measure at equidistance spaced tangent heights or collect more data from high signal regions at low altitudes, to see which of the tested cases is most effective. We assess the number of singular values above and below a certain SNR visually. Our objective

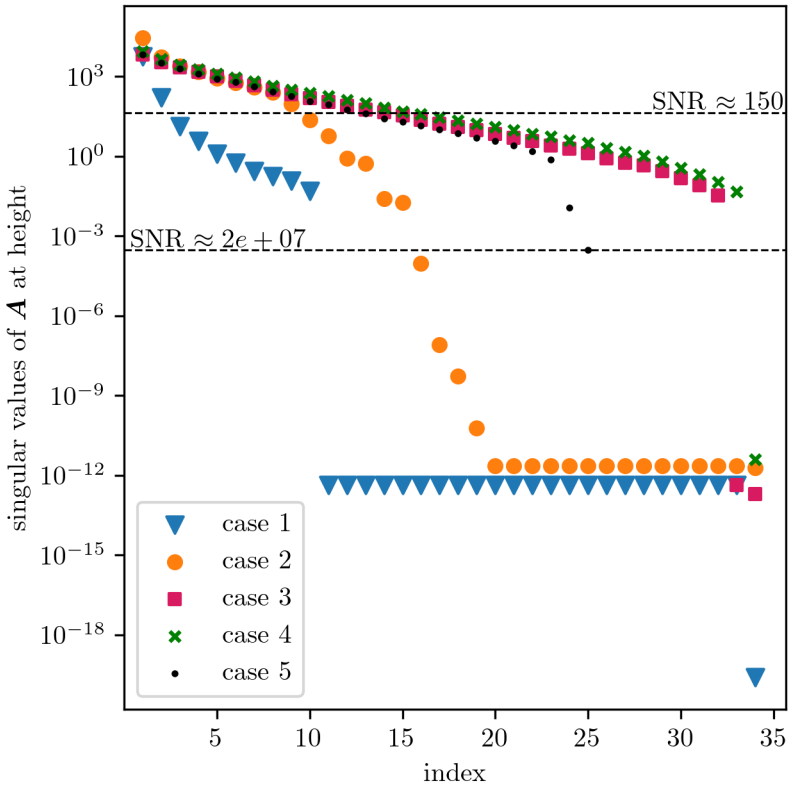

Figure 3.3: We plot the singular values of the forward model matrix for different sequences of measurements. The corresponding tangent heights of the test cases are plotted in Fig. 3.2. The dotted vertical line marks where the singular values are dominated by noise according to a SNR.

is to measure ozone $\boldsymbol{x}$ so our forward model $\boldsymbol{A}$ includes temperature and pressure, the latter is dominant, see Fig. 4.4, and decreases exponentially in height and hence does affect the information passed through the model. If the pressure is high, the noise is low, and if the pressure is low, the data is noise-dominated. We start with case 3 in Fig. 3.2 where measurements are spaced according to a pointing accuracy of 150arc sec, given to us by the team of the University of New South Wales Canberra Space [50]. The pointing accuracy determines how well the satellite can point in a certain direction and, hence, roughly the spacing in between two measurements. The corresponding singular values are plotted in Fig. 3.3, of which the first 25 decrease linearly in log-space and about 10-15 singular values lie above the SNR. In comparison, if we measure a lot of times in regions where the data is noise-dominated (high altitude), case 1, we do obtain more information since the singular values decrease rapidly. Measuring lots of times at low altitudes, where the data is informative, and less at higher altitudes, case 2, does not seem optimal either, as we observe one larger singular value, but the other singular values decrease faster compared to case 3. Now, if we double the number of measurements compared to case 3, see case 4, we do get slightly larger singular values, but not significantly so that it

would be worth the engineering effort required to achieve that. The measurements with equidistance-spaced tangent height seem to be most informative. By exploratory analysis, we find that we can tolerate a slightly larger distance between tangent heights (pointing accuracy of 175arc sec) than required by [50], see case 5. In that case, we also stop measuring when the signal is too noisy and decrease the number of measurements taken without losing information. We note that if one wanted to obtain all information provided by the forward model, we would need a signal-to-noise ratio of roughly 10^7.

In principle, we show that it does not depend on how one measures, one can not get more information by measuring more in regions where the information content is low or high. This contradicts the current measurement setup on the AURA MLS [8], which reports high noise in lower atmospheric regions, due to thermal radiation from the earth, and measures more in those regions.

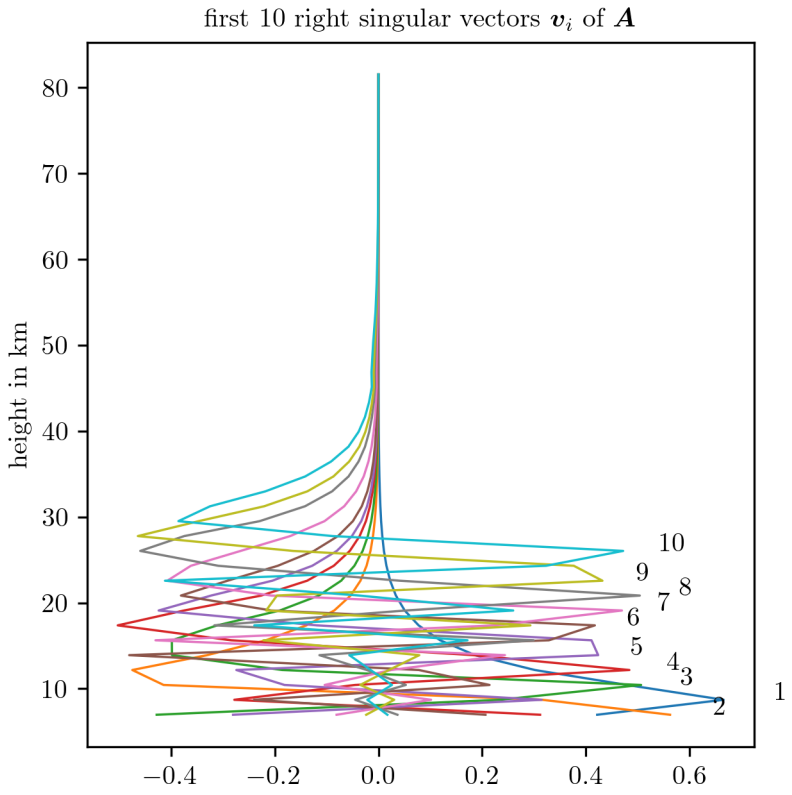

Figure 3.4: We plot the first 10 right singular vectors of the forward model matrix for case 5 sequence of measurements, see Fig. 3.3. These singular vectors correspond to high singular values of the forward model, see Fig. 3.3.

Consequently, we proceed with case 5 and plot the right singular vectors of the forward model versus height in the atmosphere to see where our model is most informative, or which structures of the parameter space are picked up by the model. The first 10 right singular vectors, in Fig. 3.4, corresponding to the 10 largest singular values, pick up

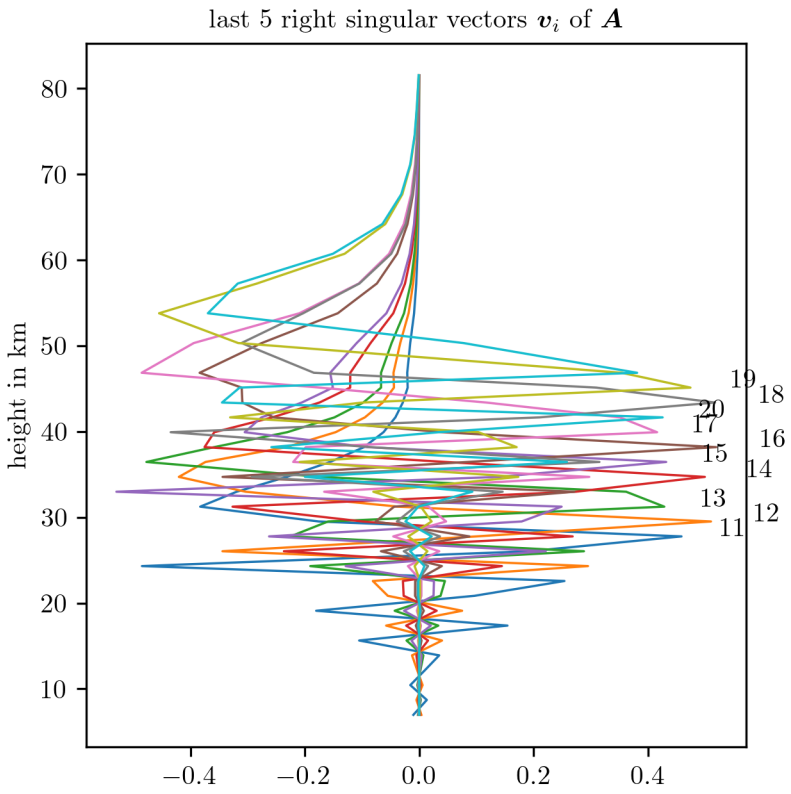

Figure 3.5: We plot the right singular vectors with index $i = 11, \ldots, 19$ of the forward model matrix for case 5 sequence of measurements, see Fig. 3.3. These singular vectors correspond to singular values around the noise level of the measurement, see Fig. 3.3.

structures in lower atmospheric regions. So we can assume that, given some data, we will be able to provide good reconstructions of the parameter in lower altitudes. Next, we plot the right singular vectors corresponding to the singular values σ_j for $j = 11, \ldots, 20$ in Fig. 3.5, where the nose starts to dominate the data. These singular values lie in regions around the SNR, see Fig. 3.3, and pick up values in the middle of the atmosphere. Consequently, we expect a higher uncertainty of reconstructed parameter values in the middle atmospheric regions. The singular vectors corresponding to the last 5 singular values pick up structures in higher altitudes, but since the singular values are very small, we will not be able to retrieve those structures. More specifically, the retrieved parameter values at higher altitudes will be fully determined by the prior or, in the case of regularisation, by the regulariser [7].

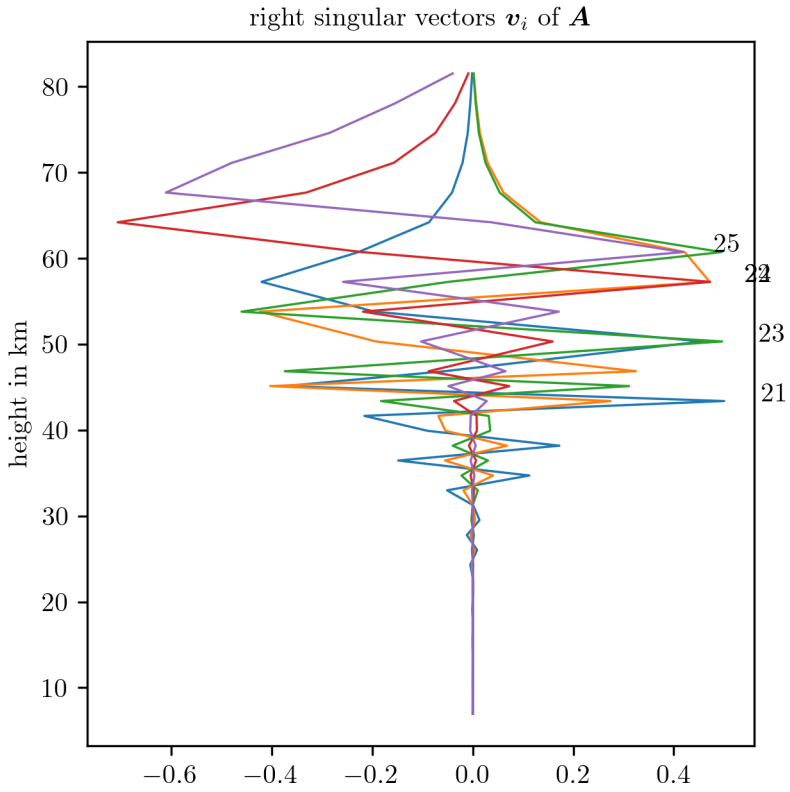

Figure 3.6: We plot the last 5 right singular vectors of the forward model matrix for the case 5 sequence of measurements, as displayed in Fig. 3.2. These singular vectors correspond to small singular values of the forward model, see Fig. 3.3.

4
Results and Conclusions

In this chapter, we use the forward model to generate data given an underlying ground truth and then guide the reader through the process of setting up a Bayesian framework and ultimately to obtaining the posterior distributions of parameters of interest, such as ozone concentration or pressure and temperature profiles. Once we simulated some data, we established a choice of prior distributions within our Bayesian model, see Sec. 4.2, and formulate the posterior distributions for ozone and pressure over temperature, respectively. In doing so, we sample from the marginal posterior for ozone and compare that to the tensor-train (TT) approximation. Based on the linear forward model $\boldsymbol{A}_L$ we calculate the mean and the covariance matrix of the full conditional posterior of ozone and generate an affine subspace with samples from that distribution. Then we approximate the non-linear forward model $\boldsymbol{A}_{NL} \approx \boldsymbol{M}\boldsymbol{A}_{NL}$, with the affine map$\boldsymbol{M}$, see Sec. 4.4. We repeat the marginal and then conditional (MTC) scheme to provide a posterior distribution of ozone VMR based on the approximate forward model as well as posterior pressure and temperature profiles, and compare to a ground truth. Lastly, we evaluate some errors occurring during the process. All programming and analysis are done in Python on a MacBook Pro from 2019 with a 2.4 GHz quad-core Intel Core i5 processor.

4.1 Simulate Data based on a Ground Truth

We take a ground truth ozone VMR at distinct pressure values generated from some data [9] of the MLS on the aura satellite within the Antarctic region and with a peak in high altitude, see Fig. 4.11, which seems to be a typical night time profile [44].

We target Ozone at a frequency of 235.71 Ghz, which lies within the region where the MLS observers ozone [51, 52]. The corresponding wave number is $\nu = 7.86\text{cm}^{-1}$. We

recursively calculate the geometric height with the hydrostatic equilibrium equation

$$\frac{\mathrm{d}p}{p} = \frac{-gM}{R^* T}\mathrm{d}h\,, \tag{4.1}$$

with the acceleration due to gravity

$$g = g_0\left(\frac{r_0}{r_0 + h}\right), \tag{4.2}$$

where the polar radius pf the earth is $r_0 \approx 6356\,\mathrm{km}$, the gravitation at sea level is $g_0 \approx 9.81\mathrm{m/s}^2$, $R^* = 8.31432 \times 10^{-3}\mathrm{Nm/kmol/K}$ and the mean molecular weight of the air is $M = 28.97\mathrm{kg/kmol}$ [53]. This holds up to a geometric height of 86km, where we ignore a 0.04% non-linear change in M from 80km to 86km in geometric altitude.

Following [53] we form a temperature function

$$T(h) = \begin{cases} T_0 & , \quad h = 0 \\ T_0 + a_0 h & , \quad 0 \leq h < h_{T,1} \\ T_0 + a_0 h_{T,1} & , \quad h_{T,1} \leq h < h_{T,2} \\ T_0 + a_0 h_{T,1} + a_1(h_{T,2} - h_{T,1}) + a_2(h - h_{T,2}) & , \quad h_{T,2} \leq h < h_{T,3} \\ T_0 + a_0 h_{T,1} + a_1(h_{T,2} - h_{T,1}) + a_2(h_{T,3} - h_{T,2}) & \\ \quad + a_3(h - h_{T,3}) & , \quad h_{T,3} \leq h < h_{T,4} \\ T_0 + a_0 h_{T,1} + a_1(h_{T,2} - h_{T,1}) + a_2(h_{T,3} - h_{T,2}) & \\ \quad + a_3(h_{T,4} - h_{T,3}) + a_4(h - h_{T,4}) & , \quad h_{T,4} \leq h < h_{T,5} \\ T_0 + a_0 h_{T,1} + a_1(h_{T,2} - h_{T,1}) + a_2(h_{T,3} - h_{T,2}) & \\ \quad + a_3(h_{T,4} - h_{T,3}) + a_4(h_{T,5} - h_{T,4}) + a_5(h - h_{T,5}) & , \quad h_{T,5} \leq h < h_{T,6} \\ T_0 + a_0 h_{T,1} + a_1(h_{T,2} - h_{T,1}) + a_2(h_{T,3} - h_{T,2}) & \\ \quad + a_3(h_{T,4} - h_{T,3}) + a_4(h_{T,5} - h_{T,4}) + a_5(h_{T,6} - h_{T,5}) & \\ \quad + a_6(h - h_{T,6}) & , \quad h_{T,6} \leq h \lesssim 86 \end{cases}$$

with gradient and height values provided by [53], see Tab. 4.1. This acts as the ground truth temperature profile, see Fig. 4.5.

Then we can compute a data vector $\boldsymbol{y} = \boldsymbol{A}_{NL} + \boldsymbol{\nu}$, with $m = 30$ measurements according to the radiative transfer equation (RTE), see Eq. 3.1 which we solve using the trapezoidal integration rule, determined by the satellite pointing accuracy of 175arc sec, see Fig. 3.2. We assume an atmosphere between $h_{L,1} = 7\mathrm{km}$ and $h_{L,n} = 83.3\mathrm{km}$ with $n = 34$ equidistant layers. The height value $h_{L,i}$ for each layer $i = 1, \ldots, n$ is defined by the pressure values from [9] and the hydrostatic equilibrium equation, see Eq. 4.1. We calculate the absorption constant $k(\nu, T)$ as in Eq. 3.2, following the *HITRAN* database [45], which provides the line intensity $L(\nu, T_{\mathrm{ref}})$ for the isotopologue $^{16}O_3$ with the AFGL

subscript i	geometric height $h_{T,i}$ in km	gradient a_i
0	0	-6.5
1	11	0
2	20.1	1
3	32.2	2.8
4	47.4	0
5	51.4	-2.8
6	71.8	-2

Table 4.1: Definition of height depending temperature gradients.

Code 666. This gives us a non-linear forward model matrix $\boldsymbol{A}_{NL} = \boldsymbol{A}(\boldsymbol{x}, \boldsymbol{p}, \boldsymbol{T}) \in \mathbb{R}^{m \times n}$, where $\boldsymbol{x} \in \mathbb{R}^n$ is vector related to the ozone VMR, $\boldsymbol{p} \in \mathbb{R}^n$ is the vector describing the pressure values and $\boldsymbol{T} \in \mathbb{R}^n$ the temperature values.

Lastly we add normally distributed $\boldsymbol{\nu} \sim \mathcal{N}(0, \gamma^{-1}\boldsymbol{I})$ noise so that the SNR is 150, see Eq. 3.8, similar to [55], where a signal with a maximal spectral intensity of around 100K and a noise range of 0.4 to 1.6K is reported. We would like to note that the methods used in this thesis, will work with different SNR or other frequencies.

When we plot the data in Fig. 4.1, we see that, as mentioned in Section 3.1, the data is noise dominated in higher altitudes. Now, given the data, we like to determine the posterior distributions over ozone $\boldsymbol{x}$, pressure $\boldsymbol{p}$ and temperature $\boldsymbol{T}$ at different heights.

4.2 Setup a hierarchical Bayesian Framework

Since the forward model described in Ch. 3 is weakly non-linear we will set up a linear Bayesian hierarchical framework first based on the linear forward model $\boldsymbol{A}_L$ and then later the approximated version $\boldsymbol{A}_{NL}\boldsymbol{M}\boldsymbol{A}_L$. Furthermore, the noise is normally distributed, so we establish a linear-Gaussian Bayesian hierarchical framework, aiming to recover an ozone profile and a pressure over temperature profile. In doing so, we first draw a directed acyclic graph (DAG) to visualise the measurement and modelling process and determine hyper-parameters and correlations between parameters. Then we define prior distributions over all parameters as well as a likelihood function so that we can formulate the posterior distribution.

We draw a DAG for the measurement and modelling process, where the hyper-hyper-parameters $\theta_\gamma, \theta_\delta, \theta_{p_0}, \theta_b, \theta_{\boldsymbol{h}}, \theta_{T_0}, \theta_{\boldsymbol{a}}$ in the top row of Fig. 4.2 determine the hyper-prior distributions $\pi(\gamma, \delta, p_0, b, \boldsymbol{h}_T, \boldsymbol{T}_0, \boldsymbol{a})$ statistically (solid line). Then the hyper-parameters determine the parameters $\boldsymbol{p}/\boldsymbol{T}$ deterministically. The temperature function $\boldsymbol{T} = (T_0, \boldsymbol{a}, \boldsymbol{h}_T)$, Eq. 4.3, is determined through $\boldsymbol{a}$ the temperature gradients at heights $\boldsymbol{h}$,

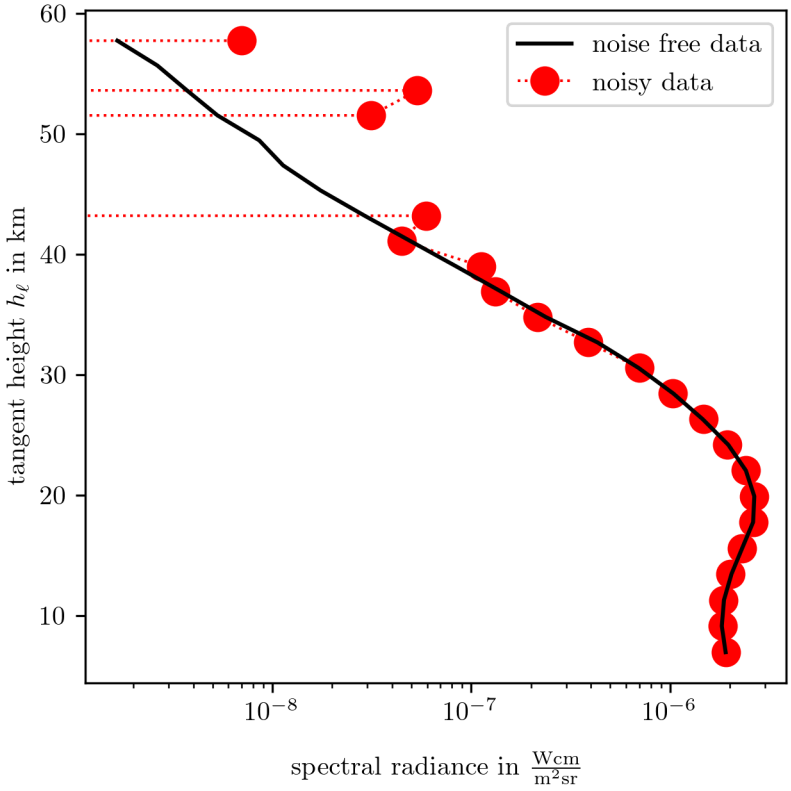

Figure 4.1: Logarithmic plot of data points at different tangent height. Note that negative values are not appearing and we see that at noise is dominating at high altitudes.

see Tab. 4.1, where h_0 is set to zero as we model temperature variability at the sea-level temperature trough the an additional input T_0. Note that we define an exponential pressure function, Eq. 4.16, later in Sec. **??** so that $\boldsymbol{p}(p_0, b)$ is defined through the hyper-parameters p_0 (pressure at sea-level) and b (exponential gradient). Since we do not parametrise the ozone profile, we assume a certain smoothness defined through the smoothness hyper-parameter δ and a precision matrix $\boldsymbol{Q}(\delta)$ which statistically defines a distribution over $\boldsymbol{x}$ (solid lines). The parameters $\boldsymbol{x}, \boldsymbol{p}, \boldsymbol{T}$ progress deterministically, see RTE in Eq. 3.1, into the forward model $\boldsymbol{A}_{NL}$ and generate a space of all possible noise free data $\boldsymbol{\Omega}$. From that space of all measurable $\boldsymbol{\Omega}$ we pick one data set to which we add some noise $\boldsymbol{\eta} \sim \mathcal{N}(0, \boldsymbol{\Sigma})$, which is modelled through the hyper-parameter γ and the precision matrix $\boldsymbol{\Sigma} = \gamma^{-1}\boldsymbol{I}$ so that we obtain the noisy data vector $\boldsymbol{y}$. Since the noise is normally distributed, so is the likelihood function $\pi(\boldsymbol{y}|\boldsymbol{x}, \boldsymbol{p}, \boldsymbol{T})$. Then the joint posterior distribution

$$\pi(p_0, b, \boldsymbol{h_T}, \boldsymbol{a}, \delta, \gamma, \boldsymbol{x}|\boldsymbol{y}) \propto \pi(\boldsymbol{y}|\boldsymbol{x}, \boldsymbol{p}, \boldsymbol{T})\pi(p_0, b, \boldsymbol{h_T}, \boldsymbol{a}, \delta, \gamma) \tag{4.3}$$

over all 17 hyper-parameters and the parameter $\boldsymbol{x} \in \mathbb{R}^{45}$ is 62 dimensional. Ideally, we characterise the joint posterior, but this is computationally not feasible. Instead,

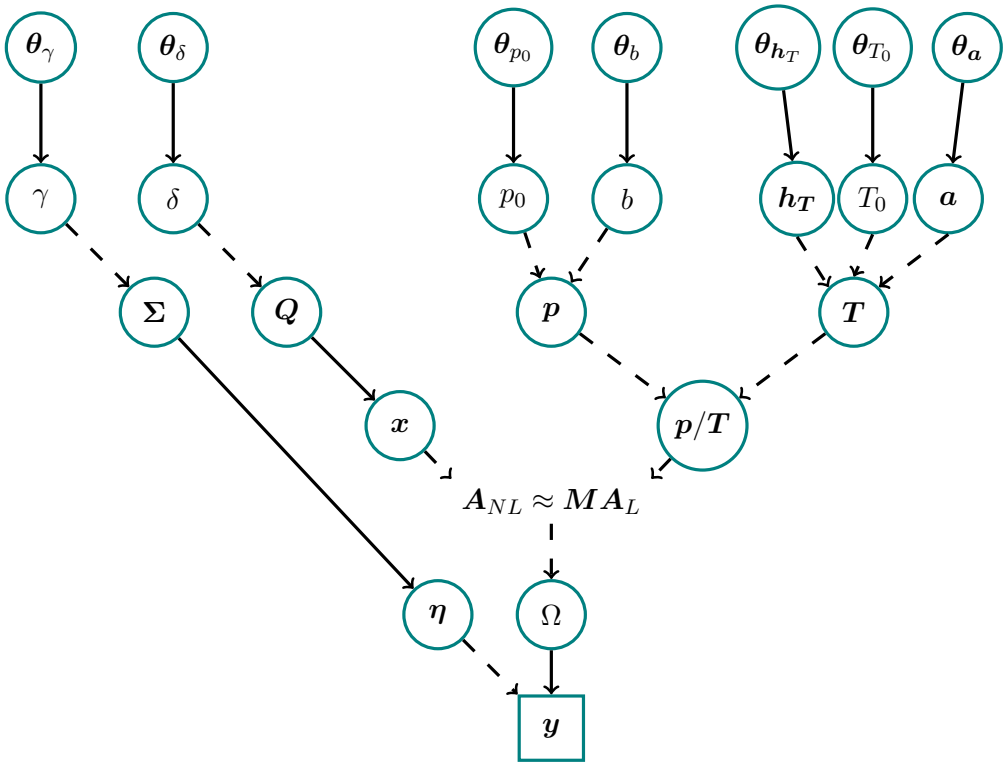

Figure 4.2: Complete directed acyclic graph of the forward model. The hyper-parameters at the top deterministically (dotted line) describe the parameters $(\boldsymbol{p}/\boldsymbol{T})$ or the noise covariance $\boldsymbol{\Sigma} = \gamma^{-1}\boldsymbol{I}$ of the random (solid line) noise $\boldsymbol{\eta} \sim \mathcal{N}(0, \gamma^{-1}\boldsymbol{I})$ and precision matrix $\boldsymbol{Q} = \delta\boldsymbol{L}$ of the distribution of $\boldsymbol{x} \sim \mathcal{N}(0, \delta\boldsymbol{L})$, where $\boldsymbol{L}$ is a graph Laplacian as in Eq. 4.6. We can group the noise precision γ and the smoothness parameter δ to define the marginal posterior over those hyper-parameters and then condition on them for the conditional posterior distribution,for further details see Fig. **??**. In this whole process where we condition on the pressure $\boldsymbol{p}$ and temperature $\boldsymbol{T}$, which we retrieve separately, see Fig. **??**. The hyper-parameters h_0, p_0, b deterministically describe the pressure function in Eq. 4.16, note that we only need three parameters here since $h_0 < h_{L,0}$ and $\boldsymbol{h} = \{h_1, h_2, h_3, h_4, h_5, h_6\}$, $\boldsymbol{a} = \{a_0, a_1, a_2, a_3, a_4\}$ and T_0 determine the temperature function. The parameters $\boldsymbol{x}$ and $\boldsymbol{p}/\boldsymbol{T}$ determine the space of all measurable noise free data $\boldsymbol{\Omega}$ through the forward model $\boldsymbol{A}(\boldsymbol{x}, \boldsymbol{p}, \boldsymbol{T})$ from which we randomly observe data set plus some random noise.

we factorise the posterior into

$$\pi(p_0, b, \boldsymbol{h_T}, \boldsymbol{a}, \delta, \gamma, \boldsymbol{x}|\boldsymbol{y}) = \pi(\delta, \gamma, \boldsymbol{x}|p_0, b, \boldsymbol{h_T}, \boldsymbol{a}, \boldsymbol{y})\pi(p_0, b, \boldsymbol{h_T}, \boldsymbol{a}|\delta, \gamma, \boldsymbol{x}, \boldsymbol{y})\,, \tag{4.4}$$

where we either condition on ozone $\boldsymbol{x}$ and the smoothness hyper-parameter δ as well as the noise hyper-parameter γ or on the fraction $\boldsymbol{p}/\boldsymbol{T}$, pressure over temperature, and its hyper-parameters. Again as in Sec. 3 for brevity we write $\pi(p_0, b, \boldsymbol{h_T}, \boldsymbol{a}|\gamma, \boldsymbol{y})$ and $\pi(\delta, \gamma, \boldsymbol{x}|\boldsymbol{y})$, which implies that we conditioned on $\boldsymbol{x}$ or $\boldsymbol{p}$ and $\boldsymbol{T}$. Next, we need to specify the prior distribution, which we summarise in Tab. 4.2, to formulate the posterior distributions.

4.2.1 Ozone conditioned on Pressure and Temperature

In this section, we choose prior distributions and describe the approach to evaluate the posterior distribution for ozone $\pi(\delta, \gamma, \boldsymbol{x}|\boldsymbol{y})$, including the noise hyper-parameter

		TT bounds			
model parameters	priors	lower	upper	τ_{int}	Context
γ	$\mathcal{T}(1, 10^{-10})$	$5\,10^{-8}$	$4.5\,10^{-7}$	9 ± 0.1	$\boldsymbol{y}$
δ	$\mathcal{T}(1, 10^{-10})$	-	-	1.5 ± 0.1	$\boldsymbol{x}$
λ	-	500	10^4	3.5 ± 0.3	$\boldsymbol{x}$
$\boldsymbol{x}$	$\mathcal{N}(0, \delta\boldsymbol{L})$	-	-		$\boldsymbol{x}$
p_0	$\mathcal{N}(1243, 5)$	1229	1259	550 ± 9	$\boldsymbol{p/T}$
T_0	$\mathcal{N}(288.15, 4.5)$	275	302	2446 ± 76	$\boldsymbol{p/T}$
$h_{T,1}$	$\mathcal{N}(11, 0.5)$	9.5	12.5	1820 ± 49	$\boldsymbol{p/T}$
b	$\mathcal{N}(0.167, 5\,10^{-4})$	0.165	0.171	2813 ± 92	$\boldsymbol{p/T}$
$h_{T,3}$	$\mathcal{N}(32.3, 2.5)$	25.2	39.8	394 ± 5	$\boldsymbol{p/T}$
a_0	$\mathcal{N}(-6.5, 0.01)$	-6.53	-6.47	330 ± 4	$\boldsymbol{p/T}$
$h_{T,2}$	$\mathcal{N}(20.1, 1.6)$	17.7	22.3	454 ± 7	$\boldsymbol{p/T}$
a_1	$\mathcal{N}(0, 0.1)$	-0.3	0.3	508 ± 8	$\boldsymbol{p/T}$
a_2	$\mathcal{N}(1, 0.01)$	0.97	1.03	341 ± 5	$\boldsymbol{p/T}$
a_3	$\mathcal{N}(2.8, 0.1)$	2.5	3.1	316 ± 4	$\boldsymbol{p/T}$
$h_{T,4}$	$\mathcal{N}(47.4, 5)$	45.9	48.9	324 ± 4	$\boldsymbol{p/T}$
a_4	$\mathcal{N}(0, 0.1)$	-0.3	0.3	335 ± 4	$\boldsymbol{p/T}$
$h_{T,5}$	$\mathcal{N}(51.4, 5)$	49.9	52.9	319 ± 4	$\boldsymbol{p/T}$
a_5	$\mathcal{N}(-2.8, 0.1)$	-3.1	-2.5	335 ± 4	$\boldsymbol{p/T}$
$h_{T,6}$	$\mathcal{N}(71.8, 3)$	62.5	80.8	347 ± 5	$\boldsymbol{p/T}$
a_6	$\mathcal{N}(-2, 0.01)$	-2.03	-1.97	320 ± 4	$\boldsymbol{p/T}$

Table 4.2: Summary of relevant parameter characteristics, bounds and sampling statistics. We denote $\mathcal{N}(\mu, \sigma)$ as the Gaussian and $\mathcal{T}(\alpha = \text{scale}, \beta = \text{rate})$ as the gamma distribution. The IACT τ_{int} is estimated as in [56] from posterior samples based on the approximated forward map.

γ. Assuming Gaussian noise $\boldsymbol{\eta} \sim \mathcal{N}(0, \gamma^{-1}\boldsymbol{I})$, we define a linear-Gaussian Bayesian hierarchical model [12]

$$\boldsymbol{y}|\boldsymbol{x}, \gamma \sim \mathcal{N}(\boldsymbol{A}\boldsymbol{x}, \gamma^{-1}\boldsymbol{I}) \tag{4.5a}$$

$$\boldsymbol{x}|\delta \sim \mathcal{N}(0, \delta\boldsymbol{L}) \tag{4.5b}$$

$$\delta, \gamma \sim \pi(\delta, \gamma), \tag{4.5c}$$

with a normally distributed likelihood $\pi(\boldsymbol{y}|\boldsymbol{x}, \gamma)$ including the forward model matrix $\boldsymbol{A}$ and prior distributions $\pi(\boldsymbol{x}|\delta)$ and $\pi(\delta, \gamma)$, the noise covariance matrix $\gamma^{-1}\boldsymbol{I}$, the prior precision matrix $\delta\boldsymbol{L}$ and the prior mean set to $\mathbf{0}$. The chosen Bayesian model is very similar to a regularisation problem, since we like to show that regularisation is depreciated, and we are able to receive much more meaningful results compared to a regularisation approach.

Prior Modelling

To complete the Bayesian framework, we have to define prior distributions over the hyper-parameters and parameters. Ideally, we define the prior distributions as uninformative as possible, and include functional dependencies and physical properties.

First, we set the precision matrix of the prior distribution $\boldsymbol{x}|\delta$ to

$$\delta \boldsymbol{L} = \delta \begin{bmatrix} 2 & -1 & & & \\ -1 & 2 & -1 & & \\ & \ddots & \ddots & \ddots & \\ & & -1 & 2 & -1 \\ & & & -1 & 2 \end{bmatrix} \tag{4.6}$$

which is the 1-dimensional Graph Laplacian as in [12, 40] with Dirichlet boundary condition. This matrix will also act as the regulariser later in the Regularisation section, see Sec. 2.5. For δ and γ we pick relatively uninformative gamma distributions so that $\gamma \sim \mathcal{T}(\boldsymbol{\theta}_\gamma)$ and $\delta \sim \mathcal{T}(\boldsymbol{\theta}_\delta)$, where $\boldsymbol{\theta}_\gamma = \boldsymbol{\theta}_\delta = (1, 10^{-10})$, see Fig. 4.15. These gamma distributions have another advantage when sampling from the marginal posterior distribution $\pi(\gamma, \delta|\boldsymbol{y})$, where $\pi(\gamma|\lambda, \boldsymbol{y}) \sim \mathcal{T}(\cdot)$ with the regularisation parameter $\lambda = \delta/\gamma$. We plot the corresponding prior ozone profiles according to $\boldsymbol{x} \sim \mathcal{N}(0, \delta\boldsymbol{L})$ in Fig. **??** and like to note that we should not include negative ozone values but are currently not able to include e.g. a truncated multivariate normal prior distribution for $\boldsymbol{x}$.

Marginal and Conditional Posterior

As noted in Sec. 2.1, we factorise the posterior

$$\pi(\boldsymbol{x}, \gamma, \delta|\boldsymbol{y}) \propto \pi(\boldsymbol{y}|\boldsymbol{x}, \gamma, \delta)\pi(\boldsymbol{x}, \gamma, \delta) \tag{4.7}$$

into

$$\pi(\boldsymbol{x}, \gamma, \delta|\boldsymbol{y}) = \pi(\boldsymbol{x}|\gamma, \delta, \boldsymbol{y})\pi(\gamma, \delta|\boldsymbol{y}) \tag{4.8}$$

the marginal posterior $\pi(\gamma, \delta|\boldsymbol{y})$ and conditional posterior $\pi(\boldsymbol{x}|\gamma, \delta, \boldsymbol{y})$. Fox and Norton call this method the marginal and then conditional method (MTC) [12], where we break the correlation structure between $\boldsymbol{x}$ and γ, δ as illustrated in Fig. **??** and Fig. A.1 by marginalising over $\boldsymbol{x}$ and evaluating this marginal posterior first and *then* the conditional posterior.

For the linear-Gaussian Bayesian hierarchical model specified in Eq. 4.17, the marginal posterior distribution over the hyper-parameters is given by

$$\pi(\lambda, \gamma|\boldsymbol{y}) \propto \lambda^{n/2}\gamma^{m/2} \exp\left\{-\frac{1}{2}g(\lambda) - \frac{\gamma}{2}f(\lambda)\right\}\pi(\lambda, \gamma), \tag{4.9}$$

with $\lambda = \delta/\gamma$, and

$$f(\lambda) = \boldsymbol{y}^T\boldsymbol{y} - (\boldsymbol{A}^T\boldsymbol{y})^T(\boldsymbol{A}^T\boldsymbol{A} + \lambda\boldsymbol{L})^{-1}(\boldsymbol{A}^T\boldsymbol{y})\,, \tag{4.10a}$$

$$\text{and } g(\lambda) = \log\det(\boldsymbol{A}^T\boldsymbol{A} + \lambda\boldsymbol{L})\,, \tag{4.10b}$$

see [12, Lemma 2]. When considering $\boldsymbol{x}$ and $\boldsymbol{y}$ as a joint multivariate normal distribution or a joint Gaussian Markov random field $(\boldsymbol{x}^T, \boldsymbol{y}^T)^T$, then $\boldsymbol{x}$ conditioned on the hyper-parameters γ, δ and the data $\boldsymbol{y}$ is the normally distributed conditional posterior distribution

$$\boldsymbol{x}|\delta,\gamma,\boldsymbol{y} \sim \mathcal{N}\big(\underbrace{(\boldsymbol{A}^T\boldsymbol{A} + \delta/\gamma\boldsymbol{L})^{-1}\boldsymbol{A}^T\boldsymbol{y}}_{\boldsymbol{x}_\lambda}, \underbrace{(\gamma\boldsymbol{A}^T\boldsymbol{A} + \delta\boldsymbol{L})}_{\gamma\boldsymbol{B}_\lambda}{}^{-1}\big)\,, \tag{4.11}$$

see [12, 15, 21] for more information. In this thesis, we compute the mean

$$\mu_{\boldsymbol{x}|\boldsymbol{y}} = \int \boldsymbol{x}_\lambda \pi(\lambda|\boldsymbol{y})\mathrm{d}\lambda \approx \sum \boldsymbol{x}_{\lambda_i}\pi(\lambda_i|\boldsymbol{y})\,, \tag{4.12}$$

and covariance

$$\Sigma_{\boldsymbol{x}|\boldsymbol{y}} = \int \gamma^{-1}\pi(\gamma|\boldsymbol{y})\,\mathrm{d}\gamma \int \boldsymbol{B}_\lambda^{-1}\,\pi(\lambda|\boldsymbol{y})\,\mathrm{d}\lambda \approx \sum {\gamma_i}^{-1}\pi(\gamma_i|\boldsymbol{y}) \sum \boldsymbol{B}_{\lambda_i}^{-1}\pi(\lambda_i|\boldsymbol{y}) \tag{4.13}$$

as weighted expectations, by quadrature [57, Sec. 2.1], with $\sum\pi(\lambda_i|\boldsymbol{y}) = \sum\pi(\gamma_i|\boldsymbol{y}) = 1$. If that is too costly, the randomise-then-optimise (RTO) [12, 58] may be a feasible alternative to sample from Eq. 4.11.

Most of the computational effort lies in the evaluation of $f(\lambda)$ and $g(\lambda)$, see marginal posterior in Eq. 4.9. In Fig. 4.3 we see that $f(\lambda)$ and $g(\lambda)$ are well behaved within the region of interest. Consequently we approximate $f(\lambda) \approx \tilde{f}(\lambda)$ with a 3rd order Taylor series around the mode λ_0 of $\pi(\lambda,\gamma|\boldsymbol{y})$. We also note that $\tilde{g}(\lambda) \approx g(\lambda)$ behaves linearly around λ_0 in the log-space. As a result of these observations, the approximations are implicitly given by

$$f^{(r)}(\lambda_0) = (-1)^{r+1}r!(\boldsymbol{A}^T\boldsymbol{y})^T(\boldsymbol{B}_0^{-1}\boldsymbol{L})^r\boldsymbol{B}_0^{-1}\boldsymbol{A}_L^T\boldsymbol{y} \tag{4.14}$$

$$\text{and } \log\tilde{g}(\lambda) = (\log\lambda - \log\lambda_0)\frac{\log g(\lambda_{\max}) - \log g(\lambda_0)}{\log\lambda_{\max} - \log\lambda_0} + \log g(\lambda_0) \tag{4.15}$$

with $\boldsymbol{B}_0 = \boldsymbol{A}^T\boldsymbol{A} + \lambda_0\boldsymbol{L}$. We plot the approximations in Fig. 4.3 and elaborate on approximation errors in sec 4.8

4.2.2 Pressure and Temperature Ratio conditioned on Noise and Ozone

First, we observe that we can describe the pressure values in between $h_{L,0} = 7$km and $h_{L,n} = 83.3$km with an exponential function

$$p(h) = \exp\{-b\,h\}\,p_0 \quad , h_{L,n} \le h \le h_{L,0} \tag{4.16}$$

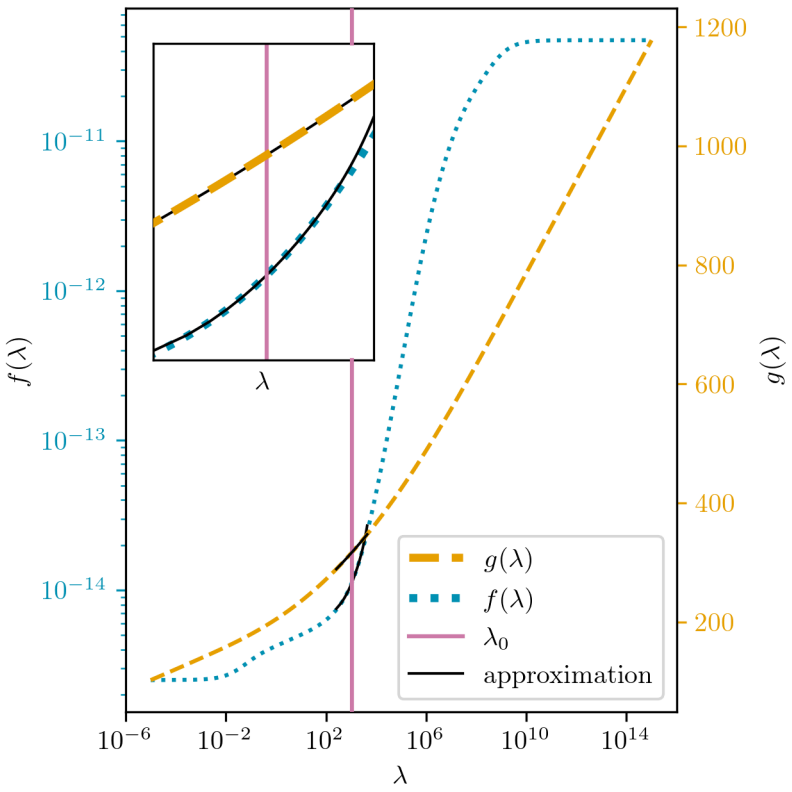

Figure 4.3: Plot of the functions $f(\lambda)$ and $g(\lambda)$ from the marginal posterior for a wide range of $\lambda = \delta/\gamma$. We plot the third order Taylor series in black around the mode of the marginal posterior (vertical line) for the sampling range of λ within the MWG algorithm.

so that we parametrize the pressure $\boldsymbol{p}$ with the hyperparameters p_0, b. Then, within the hierarchical Bayesian framework

$$\boldsymbol{y}|\boldsymbol{p}, \boldsymbol{T}, \gamma \sim \mathcal{N}(\boldsymbol{A}\,\boldsymbol{p}/\boldsymbol{T}, \gamma^{-1}\boldsymbol{I}) \tag{4.17a}$$

$$\boldsymbol{a} \sim \mathcal{N}(\boldsymbol{\mu_a}, \boldsymbol{\Sigma_a}) \tag{4.17b}$$

$$\boldsymbol{h_T} \sim \mathcal{N}(\boldsymbol{\mu_T}, \boldsymbol{\Sigma}_{\boldsymbol{h}_T}) \tag{4.17c}$$

$$T_0 \sim \mathcal{N}(\mu_{T_0}, \sigma_{T_0}) \tag{4.17d}$$

$$p_0 \sim \mathcal{N}(\mu_{p_0}, \sigma_{p_0}) \tag{4.17e}$$

$$b \sim \mathcal{N}(\mu_b, \sigma_b) \tag{4.17f}$$

we define a normally distributed likelihood (due to Gaussian noise) and priors, where the hyper-prior means and variances relate to the DAG in Fig. 4.2 so that $\boldsymbol{\theta_a} = (\boldsymbol{\mu_a}, \boldsymbol{\Sigma_a})$, $\boldsymbol{\theta}_{\boldsymbol{h}_T} = (\boldsymbol{\mu_T}, \boldsymbol{\Sigma}_{\boldsymbol{h}_T})$, $\boldsymbol{\theta}_{T_0} = (\mu_{T_0}, \sigma_{T_0})$, $\boldsymbol{\theta}_{p_0} = (\mu_{p_0}, \sigma_{p_0})$, and $\boldsymbol{\theta}_b = (\mu_b, \sigma_b)$. Note that we do not include h_0, from Tab. 4.1, in $\boldsymbol{h}_T$ since we model temperature variability at sea level through T_0.

Prior Modelling

We summarise the mean and variance in Tab. 4.2 and plot samples from the prior distribution against the ground truth for the pressure $\boldsymbol{p}$ and temperature $\boldsymbol{T}$ separately in Fig. 4.6 and 4.5 and jointly as $\boldsymbol{p}/\boldsymbol{T}$ in Fig. 4.5. We plot the prior samples against the ground truth for $1/\boldsymbol{K}$ in Fig. **??**.

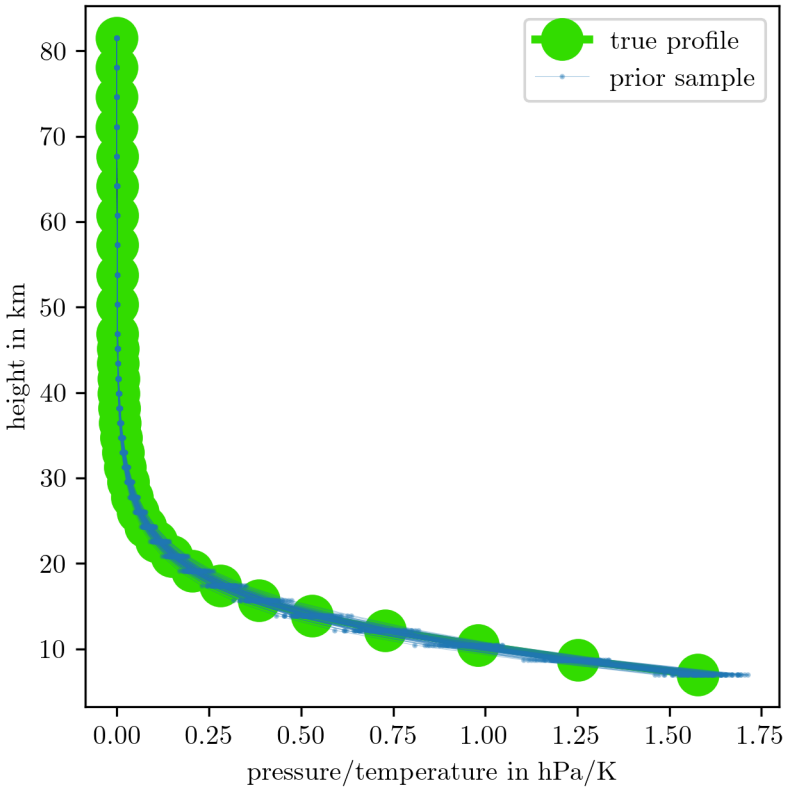

Figure 4.4: We draw samples from the hyper-prior distribution of $h_0, b, p_0, h_1, h_2, h_3, h_4, h_5, h_6, a_0, a_1, a_2, a_3, a_4$ and T_0 as defined in table 4.2 and then calculate $\boldsymbol{p}/\boldsymbol{T}$ according to the functions in Eq. 4.16 and 4.3.

We carefully choose the hyper-prior distributions $\boldsymbol{h_T}$ so that the individal distributions for heights $h_1, h_2, h_3, h_4, h_5, h_6$ do not overlap, see Fig. **??**. Additionally, we define the sampling space and the grid for the TT approximation accordingly. We remark that we can already observe in Fig. 4.4 that $\boldsymbol{p}/\boldsymbol{T}$ inherits the structure of the pressure function.

Posterior Distribution

Then we can define the posterior distribution

$$\pi(p_0, b, \boldsymbol{h_T}, \boldsymbol{c_T}, \boldsymbol{a_T} | \boldsymbol{y}, \gamma, \boldsymbol{x}) \propto \exp\Big\{ -\frac{\gamma}{2} \Big\| \boldsymbol{y} - \boldsymbol{A}\frac{\boldsymbol{p}}{\boldsymbol{T}} \Big\|^2 \Big\} \pi(p_0, b, \boldsymbol{h_T}, \boldsymbol{c_T}, \boldsymbol{a_T}) \,, \tag{4.18}$$

which is, conditioned on the noise hyper-parameter γ, the ozone profile $\boldsymbol{x}$ and the smoothness hyper-parameter δ, a 16 dimesnional distribution.

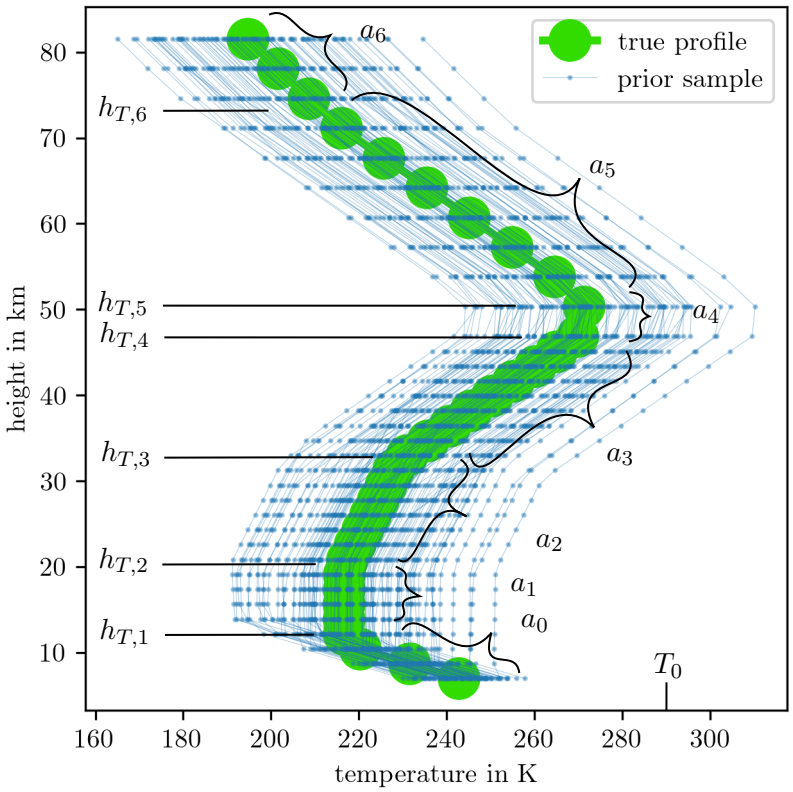

Figure 4.5: We draw samples from the hyper-prior distribution of $h_1, h_2, h_3, h_4, h_5, h_6, a_0, a_1, a_2, a_3, a_4$ and T_0 as defined in table 4.2 and then calculate $\boldsymbol{T}$ according to the function in Eq. 4.3.

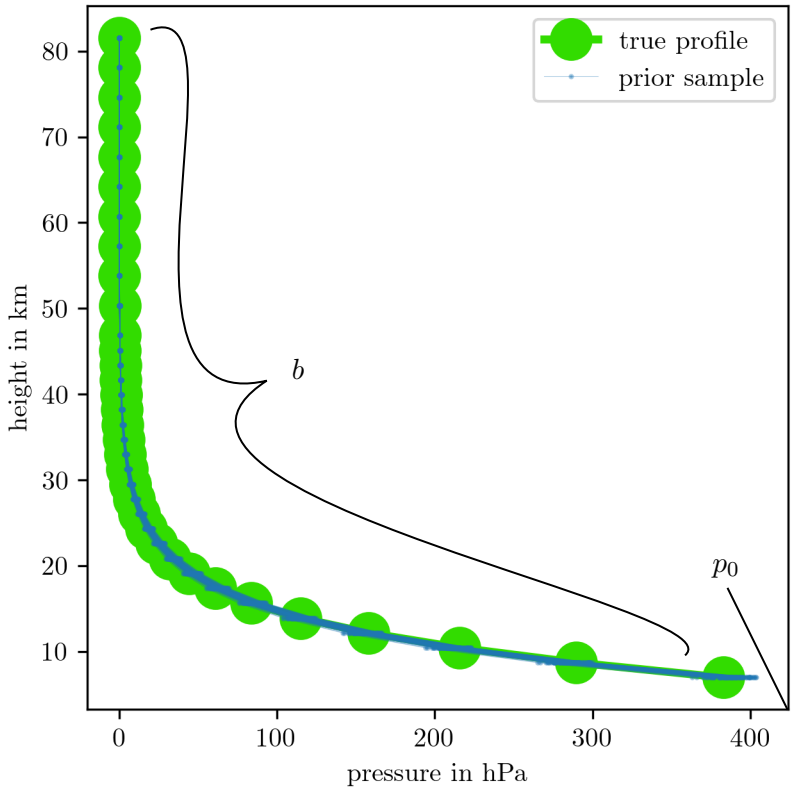

Figure 4.6: We draw samples from the hyper-prior distribution of h_0, b and p_0 as defined in table 4.2 and then calculate $\boldsymbol{p}$ according to the function in Eq. 4.16.

4.3 Posterior distribution of Ozone – linear Model

4.3.1 Sample from Marginal Posterior Distribution

We set $\boldsymbol{A} = \boldsymbol{A}_L$ and characterise the marginal posterior $\pi(\lambda, \gamma|\boldsymbol{y})$ as in Eq. 4.9 by employing a Metropolis within Gibbs (MWG) algorithm, see sec. **??**. More specifically, we implement a Metropolis random walk on the full conditional

$$\pi(\lambda|\gamma, \boldsymbol{y}) \propto \lambda^{n/2+\alpha_\delta-1} \exp\left\{-\frac{1}{2}g(\lambda) - \frac{\gamma}{2}f(\lambda) - \beta_\delta\gamma\lambda\right\} \tag{4.19}$$

and do a Gibbs step on

$$\gamma|\lambda, \boldsymbol{y} \sim \Gamma\left(\frac{m}{2} + \alpha_\delta + \alpha_\gamma, \frac{1}{2}f(\lambda) + \beta_\gamma + \beta_\delta\lambda\right) \tag{4.20}$$

to generate marginal posterior samples $(\lambda, \gamma)^{(1)}, \ldots, (\lambda, \gamma)^{(N)} \sim \pi(\lambda, \gamma|\boldsymbol{y})$. Note that, when changing variables from $\delta = \lambda\gamma$ to λ the hyper-prior distribution changes to $\pi(\lambda) \propto \lambda^{\alpha_\delta-1}\gamma^{\alpha_\delta} \exp(-\beta_\delta\lambda\gamma)$, due to $\mathrm{d}\delta/\mathrm{d}\lambda = \gamma$.

Hence we run a Metropolis random walk on $\pi(\lambda|\gamma, \boldsymbol{y})$, the proposal distribution $q(\lambda'|\lambda^{(k)}) \sim \mathcal{N}(\lambda^{(k)}, 0.8\lambda_0)$ conditioned on the previous sample $\lambda^{(k)}$, with $k = 1, \ldots, N$ is symmetric. Then, we accept or reject a new λ' sample by comparing the acceptance ratio

$$\log\left\{\frac{\pi(\lambda'|\gamma^{(k)}, \boldsymbol{y})}{\pi(\lambda^{(k)}|\gamma^{(k)}, \boldsymbol{y})}\right\} = \log\{\pi(\lambda'|\gamma^{(k)}, \boldsymbol{y})\} - \log\{\pi(\lambda^{(k)}|\gamma^{(k)}, \boldsymbol{y})\} \tag{4.21}$$

$$= \frac{n}{2}(\log\{\lambda'\} - \log\{\lambda^{(t-1)}\}) + \frac{1}{2}\Delta g + \frac{\gamma^{(t-1)}}{2}\Delta f + \beta_\delta\gamma^{(t-1)}\Delta\lambda\,, \tag{4.22}$$

where $\Delta\lambda = \lambda' - \lambda^{(k)}$ to a random uniform number in between 0 and 1. Note that since we calculate the acceptance ratio in the log space $\Delta f \approx \tilde{f}(\lambda') - \tilde{f}(\lambda^{(k)}) = \sum f^{(r)}(\lambda_0)\Delta\lambda' - \Delta\lambda^{(k)}$ is a 3rd order taylor approximaton, see Fig. 4.3, where $\Delta\lambda' = \lambda' - \lambda_0$ and $\Delta\lambda^{(k)} = \lambda^{(k)} - \lambda_0$. Similarly we approximate $\Delta g \approx \exp\log\tilde{g}(\lambda') - \exp\log\tilde{g}(\lambda^{(k)})$ as in Eq. 4.10. Lastly, a Gibbs step provides a new $\gamma^{(k+1)} \sim \gamma|\lambda^{(k+1)}, \boldsymbol{y}$, see Equation (4.20). See Algorithmic Box **??** for a summary of the general version.

We initialise the MWG at the mode $(\lambda^{(0)}, \gamma^{(0)}) = (\lambda_0, \gamma_0)$ and take for $N = 10000$ plus $N_{\text{burn-in}} = 100$ steps in less than 0.3s. The standard deviation of the normal proposal distribution is set to $\sigma_\lambda = 0.8\lambda_0$ so that the acceptance rate is ≈ 0.5 as suggested in []. The samples are plotted in Fig. 4.9 as a 2D scatter plot, as well as the trace of the MwG to show ergodicity. We calculate the integrated autocorrelation time (IACT) with the Python implementation of [], which gives us $\tau_{\text{int},\gamma} =$ and $\tau_{\text{int},\delta} =$.

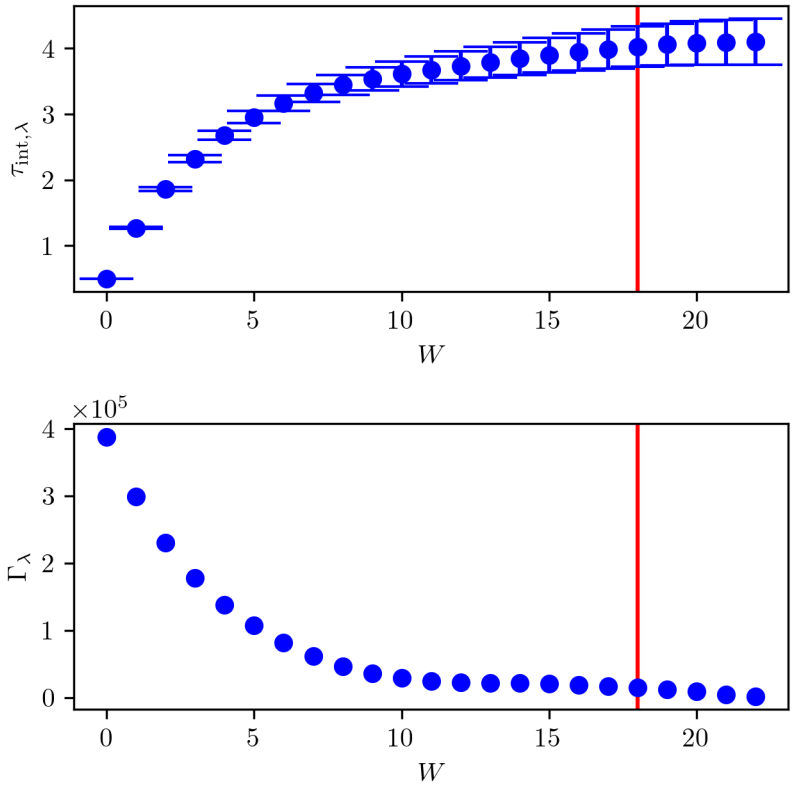

Figure 4.7

4.3.2 Tensor-train Approximation of the Marginal Posterior Distribution

Alternatively, we can approximate the marginal posterior with a tensor-train (TT) of the square root of the marginal posterior on a predefined grid. We define a grid similar to the sampling region of the MWG sampler with 25 grid points in each dimension and use the `tt.cross.rectcross.rect_cross.cross` function from the `ttpy`[59], Python package, based on the rect cross algorithm in [60]. We set the number of ranks to a constant value $r = 4$ and optimise over those ranks with one sweep to calculate the cores in less than 0.1s. To avoid underflow, we have to add a 'normalisation' constant $c = 460$ so that we approximate $\pi(\lambda|\gamma, \boldsymbol{y}) = \exp\{\log \pi(\lambda|\gamma, \boldsymbol{y}) + c\}$. Then we calculate the marginals $\pi(\lambda|\boldsymbol{y})$ and $\pi(\gamma|\boldsymbol{y})$ as described in section **??**, assuming an absolute error of 1 the constant $\xi = 1/\boldsymbol{\lambda}(\mathcal{X})$, with a diagonal mass matrix $\boldsymbol{M}_k = \text{diag}(\boldsymbol{\lambda}(X_k))$, where $\boldsymbol{\lambda}(X_k)$ is the length of the grid of the kth dimension also knows as the Lebesgue measure of a closed interval. We plot the TT approximation as a colour map on top of the obtained samples in the scatter plot in Fig. 4.9.

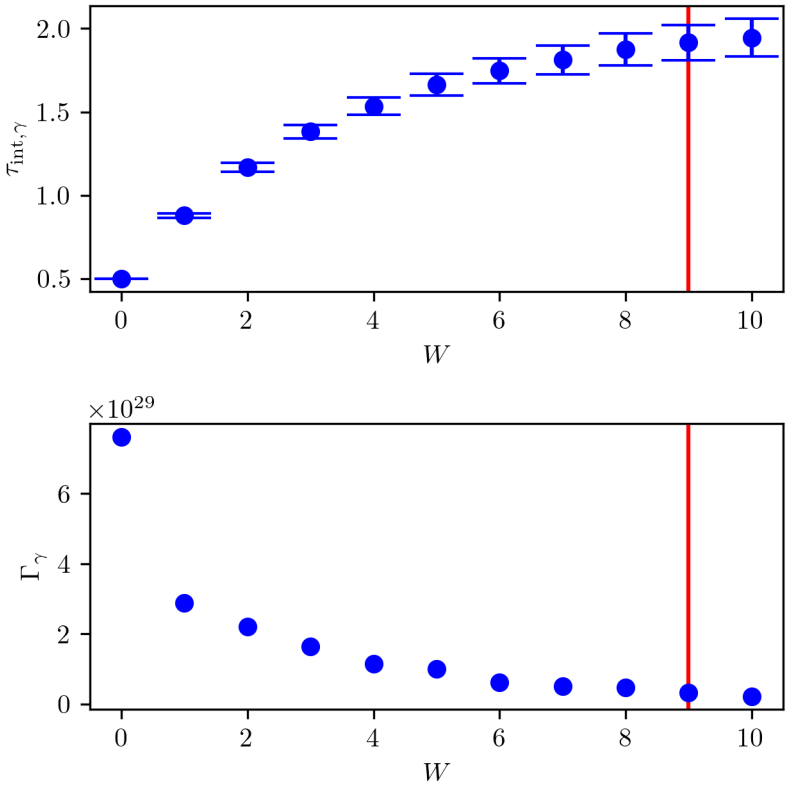

Figure 4.8

4.3.3 Full Conditional Posterior of Ozone

Based on the marginal posteror distribution $\pi(\gamma, \delta|\boldsymbol{y})$ we calculate the weighted mean and covariance of the conditional posterior $\pi(\boldsymbol{x}|\gamma, \delta, \boldsymbol{y})$ by quadrature as in Eq. 4.12 and Eq. 4.13.

By binning the output samples from the MWG, see Fig. 4.9, into a normalised histogram with 25 bins, we obtain function values for the marginal posterior. With the height of the histogram bars as quadrature weights, e.g. $\pi(\lambda_i|\boldsymbol{y})$, where λ_i is the centre of each bin we calculate the full conditional mean $\boldsymbol{\mu}_{\boldsymbol{x}|\boldsymbol{y}}$ and covariance matrix $\boldsymbol{\Sigma}_{\boldsymbol{x}|\boldsymbol{y}}$ as weighted expectations.

Alternatively we use the marginal distributions $\pi(\delta|\boldsymbol{y})$ and $\pi(\gamma|\boldsymbol{y})$ from the TT approximation of $\sqrt{\pi(\delta, \gamma|\boldsymbol{y})}$ to calculate weighted expectations of $\boldsymbol{\mu}_{\boldsymbol{x}|\boldsymbol{y}}$ and $\boldsymbol{\Sigma}_{\boldsymbol{x}|\boldsymbol{y}}$.

In practice, we have to invert $\boldsymbol{B}_\lambda$ and calculate $\boldsymbol{x}_\lambda$, see Eq. 4.11 25 times (TT grid size and number of bins). A feasible method is the Cholesky forward and backwards substitution [], which takes roughly 1s to compute the mean and variance. Note that we reject unphysical samples from the conditional posterior with negative ozone values and plot those in Fig. 4.11, including variance and mean.

Computation time is less than 0.2s.

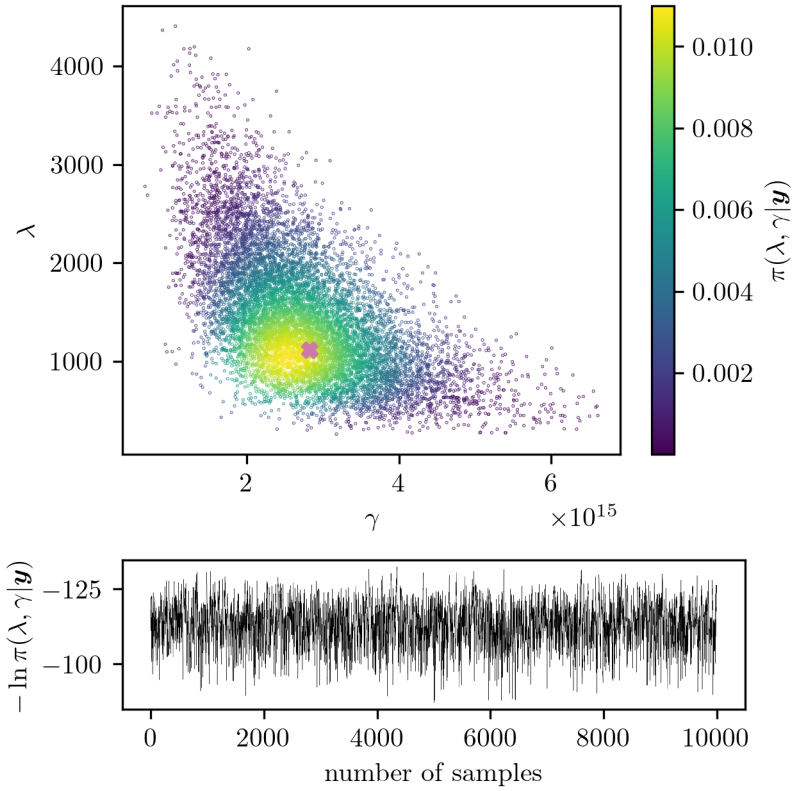

Figure 4.9: We scatter plot the samples of $\lambda = \delta/\gamma$ and γ from the marginal posterior $\pi(\lambda, \gamma|\boldsymbol{y})$ and colour code the samples using the TT approximation of $\pi(\lambda, \gamma|\boldsymbol{y})$. The mode of (λ_0, γ_0) of $\pi(\lambda, \gamma|\boldsymbol{y})$ provided by `scipy.optimize.fmin` is marked with the cross. To show ergodicity we plot the trace of the samples of the Metropolis-within-Gibbs sampler below.

4.4 Approximate non-linear Forward Model with Affine Map

With the posterior distributions formulated, we can now approximate the non-linear forward model with an affine map $\boldsymbol{M}$; we see Fig. 4.12 for the summarised strategy. We focus on the posterior distribution of ozone profiles by conditioning on pressure and temperature, as this is a quick process when using the MTC method. We approximate and sample from the marginal posterior $\pi(\gamma, \delta|\boldsymbol{y})$ and then characterise the full conditional posterior distribution $\pi(\boldsymbol{x}|\boldsymbol{y})$ based on the linear forward model $\boldsymbol{A}_L$, neglecting absorption, see Eq. 3.1. Given samples $\boldsymbol{x} \sim \pi(\boldsymbol{x}|\boldsymbol{y})$ from the full conditional posterior distribution, we can generate two affine subspaces based on the linear and non-linear model and find the mapping between those.

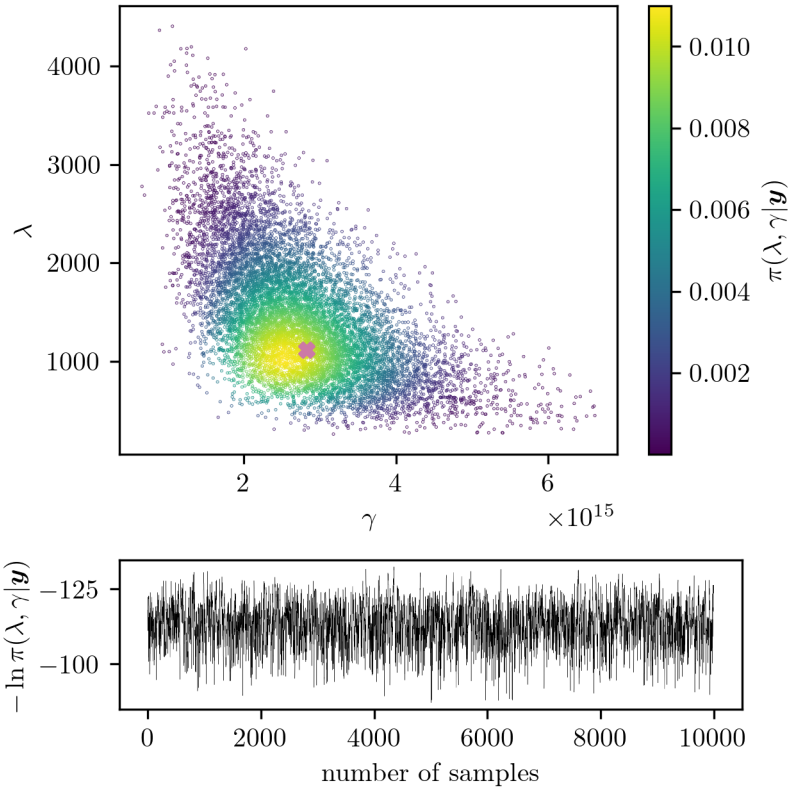

Figure 4.10

4.4.1 Asses approximated Forward Model

Given m samples $\boldsymbol{x}^j \sim \pi\boldsymbol{x}|\boldsymbol{y}$ for $j = 1, \ldots, m$ from the full conditional, as plotted in4.11, we are able approximate the non-linear forward model

$$\boldsymbol{A}_{NL} \approx \boldsymbol{M}\boldsymbol{A}_L = \boldsymbol{A}\,, \tag{4.23}$$

with the affine map $\boldsymbol{M}$ and the linear forward model $\boldsymbol{A}_L$. In doing so, we can generate two affine subspaces $\boldsymbol{W} = \{\boldsymbol{A}_L\boldsymbol{x}^1, \ldots, \boldsymbol{A}_L\boldsymbol{x}^m\}$ and $\boldsymbol{V} = \{\boldsymbol{A}_{NL}\boldsymbol{x}^1, \ldots, \boldsymbol{A}_{NL}\boldsymbol{x}^m\}$. We use the Python function `numpy.linalg.solve` to solve $\boldsymbol{M}\boldsymbol{W} = \boldsymbol{V}$ for each row of $\boldsymbol{M}$, see Sec. 2.4 for more details.

We asses the affine map by calculating the relative error$||\boldsymbol{M}\boldsymbol{W} - \boldsymbol{V}||/||\boldsymbol{M}\boldsymbol{W}||$ between the mapped noise free data and the noise free data of non-linear forward model for all of the m ozone samples, which approximnately 0.1% We display the approximation for one $\boldsymbol{x}$ sample in Fig. 4.13. Consequently, from here onwards, we use the approximated forward map $\boldsymbol{A} = \boldsymbol{M}\boldsymbol{A}_L$.

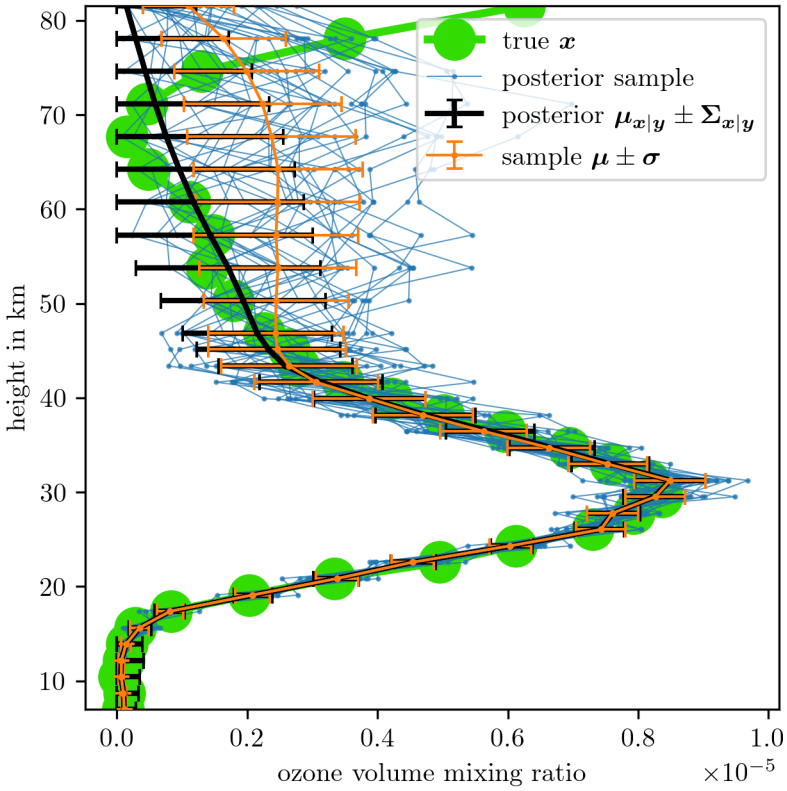

Figure 4.11: We draw samples from the conditional posterior distribution $\pi(\boldsymbol{x}|\lambda, \gamma, \boldsymbol{y})$ after characterising the marginal posterior $\pi(\lambda, \gamma|\boldsymbol{y})$ through sampling or TT approximation using the linear forward map $\boldsymbol{A}_L$. Note that we reject samples with unphysical negative values and effectively treat the conditional posterior as a truncated multivariate normal distribution. We will use those samples to find the affine map $\boldsymbol{M}$, see section 4.4

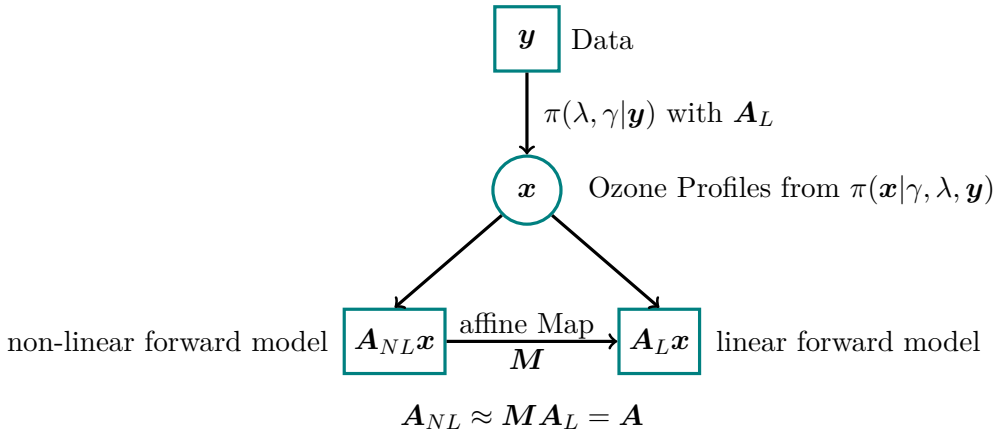

Figure 4.12: The strategy to find the affine map consist of evaluating the marginal posterior for ozone using the linear forward model. Then we draw ozone samples from the conditional posterior and calculate noise free data based on the linear and non-linear forward model. Next we find a mapping in between those two space so that we can approximate the non-linear forward model using an affine map and the linear forward model.

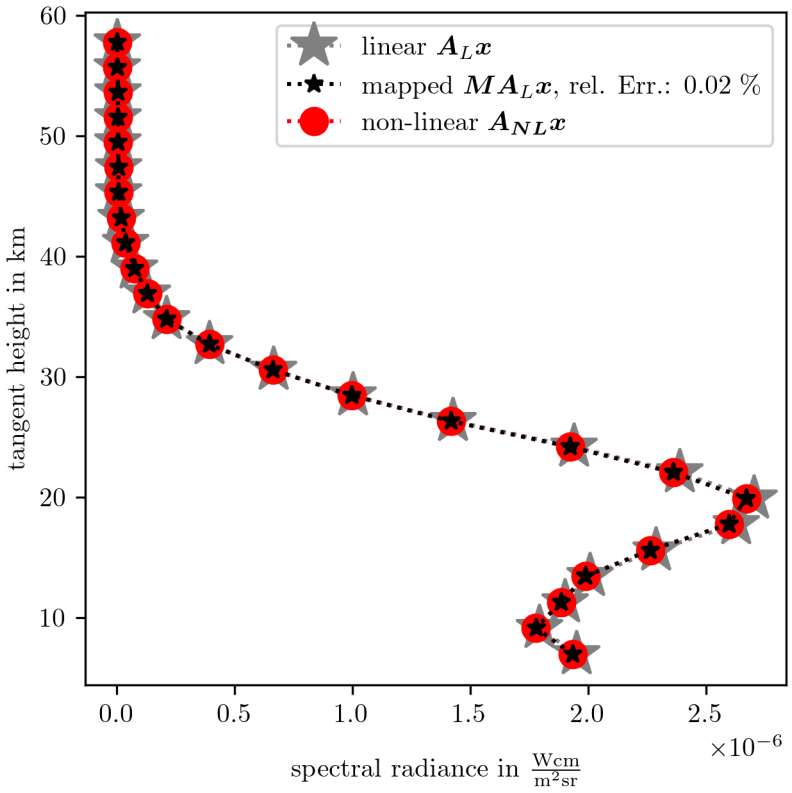

Figure 4.13: We asses how good we can map the linear forward model onto the non-linear forward model using the previous calculated affine map. The gray stars represent noise free linear data, where as the red circles present noise free non-linear data. Then we map the linear noise free data onto the non-linear noise free data and give the relative error in between the mapped noise free data and the non-linear data.

4.5 Solution by Regularisation

Since we like to compare the MTC method to regularisation methods, we calculate a solution by Tikhonov regularisation, as this is most similar to our chosen linear-Gaussian Bayesian framework. The Tikhonov regularised solution is defined as [61]

$$\boldsymbol{x}_\lambda = \arg\min_{\boldsymbol{x}} \|\boldsymbol{A}\boldsymbol{x} - \boldsymbol{y}\|_2^2 + \lambda \boldsymbol{x}^T \boldsymbol{L}\boldsymbol{x}\,, \tag{4.24}$$

with the regularisation parameter $\lambda = \delta/\gamma$. The regularised solution is typically calculated by solving the normal equations, see Sec. 2.5,

$$\boldsymbol{x}_\lambda = (\boldsymbol{A}^T\boldsymbol{A} + \lambda \boldsymbol{L})^{-1}\boldsymbol{A}^T\boldsymbol{y}\,. \tag{4.25}$$

To find the best regularised solution, we use the L-curve method [41]. Within this method we compute $\boldsymbol{x}_\lambda$, for 200 different λ values in between 1 to 10^7 and plot the solution semi norm $\sqrt{\boldsymbol{x}_\lambda^T \mathbf{L}\boldsymbol{x}_\lambda}$ against the data misfit norm $\|\boldsymbol{A}\boldsymbol{x}_\lambda - \boldsymbol{x}\|$, see Figure 4.14. The best regularised solution corresponding to the corner of the L-curve is located at the

point of maximum curvature, see triangle in Fig. 4.14, which we find with the kneedle algorithm [62] using the python function `kneed.KneeLocator` in less 0.1s.

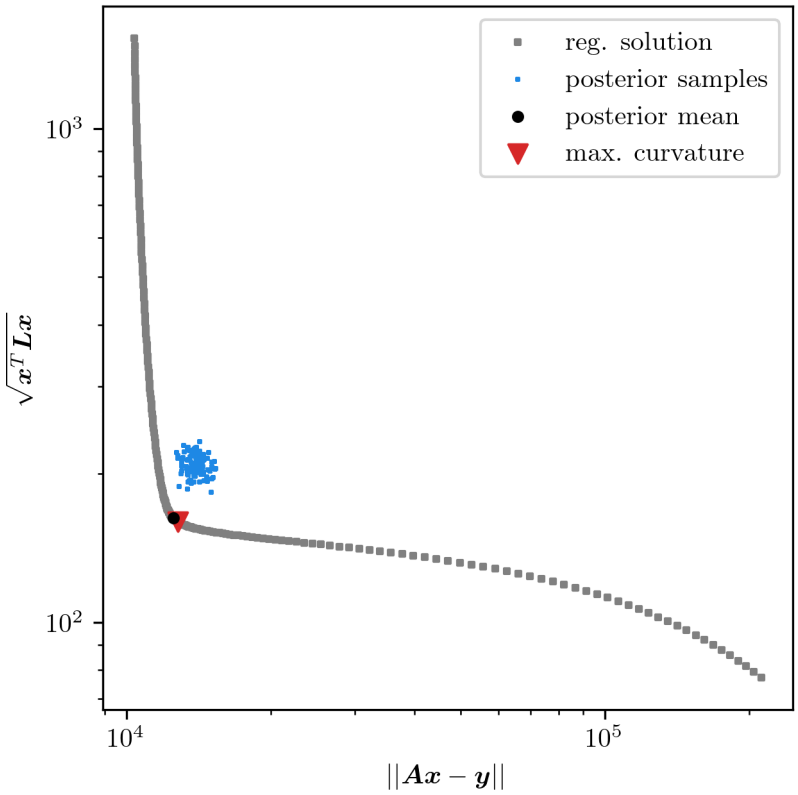

Figure 4.14: We calculate regularised solution as in Eq. **??** and plot the regularised semi norm $\sqrt{\boldsymbol{x}^T\boldsymbol{L}\boldsymbol{x}}$ against the data misfit norm $||\boldsymbol{A}\boldsymbol{x} - \boldsymbol{y}||$ to find the regularised solution at the point of maximum curvature of the so-called L-Curve. Additionally we calculate the data misfit norm and the regularised norm for the ozone posterior and for samples of the conditional posterior distribution. make box around Kneedle reagion

4.6 Posterior Distribution of Ozone – approximated Model

With the affine approximation

$$\boldsymbol{A} = \boldsymbol{M}\boldsymbol{A}_L \tag{4.26}$$

of the non-linear forward map, we use the same setup as in Sec. **??** and 4.3.3 to evaluate the marginal posterior and the conditional posterior.

4.6.1 Marginal Posterior

The marginal posterior is defined as in Eq. **??** but with $\boldsymbol{A} = \boldsymbol{M}\boldsymbol{A}_L$. We run the MWG algorithm for $N = 20000$ plus $N_{\text{burn-in}} = 100$ and plot the samples in Fig. 4.15 as well as the marginal approximations provided by the TT decomposition, where we use the same setup as in Sec. 4.3.2.

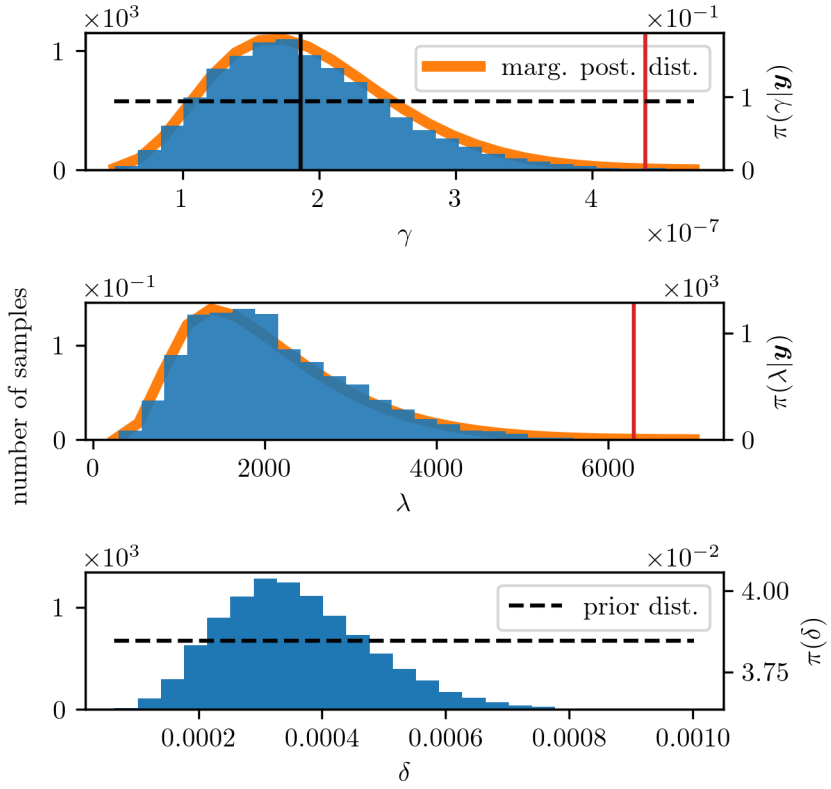

Figure 4.15: We plot the TT approximation of marginal posterior in orange and the samples as a histogram as well as the prior distribution with a dotted line. Note that we sample λ and γ using the Metropolis-within-Gibbs sampler and can calculate δ for every sample of the marginal posterior, we can not do this for the TT approximation. The regularised parameter corresponding to the regularised solution is marked thought the red vertical line at $\lambda_{\text{reg}} =$.

4.6.2 Conditional Posterior Variance and Mean

Next, we characterise the conditional posterior $\pi(\boldsymbol{x}|\gamma, \delta, \boldsymbol{y})$ as in Eq. 4.11. Again, we calculate the full conditional mean 4.12 and full conditional covariance matrix 4.13 as weighted expectation over a 25-point grid provided by either the marginal TT approximations or the histogram of samples. We plot the conditional mean and variance in Fig. 4.16 and the regularised solution and one sample from the posterior.

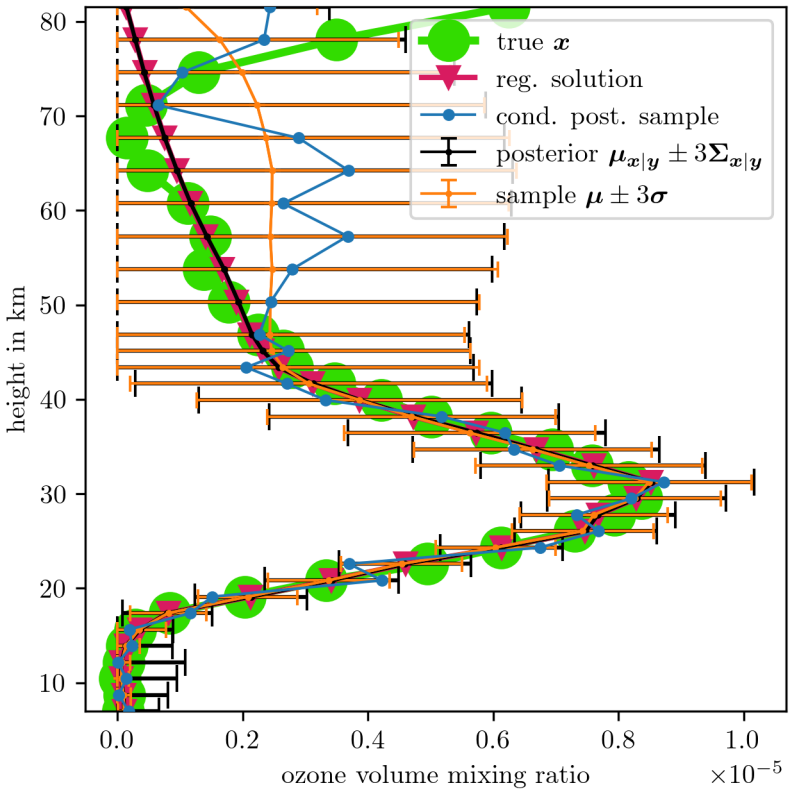

Figure 4.16: We plot the conditional posterior mean and variance in black and the regularised solution on top of the ground truth ozone profile in green. We use the updated forward map $\boldsymbol{MA}_L$

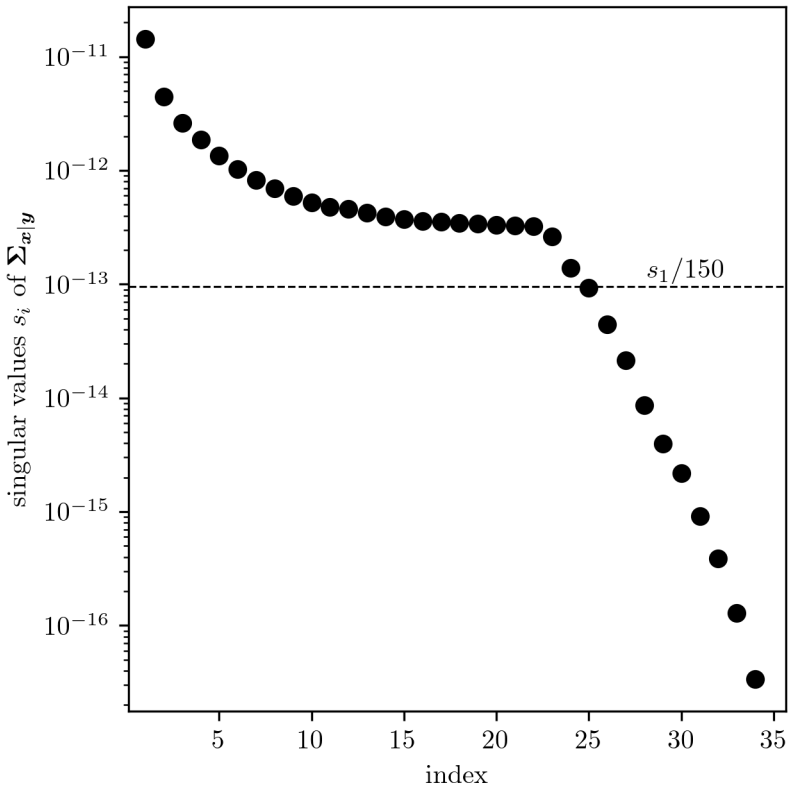
10^{-11}
10^{-12}
10^{-13}
10^{-14}
10^{-15}
10^{-16}
singular values s_i of $\mathbf{\Sigma}_{\boldsymbol{x}|\boldsymbol{y}}$
$s_1/150$
5
10
15
20
25
30
35
index

Figure 4.17

4.7 Posterior Distribution of Pressure and Temperature – approximated Forward Model

The aim now is to characterise the posterior

$$\pi(p_0, b, T_0, \boldsymbol{h_T}, \boldsymbol{a_T}|\boldsymbol{y}, \gamma, \boldsymbol{x}) \propto \exp\Big\{ -\frac{\gamma}{2}\left\|\boldsymbol{y} - \boldsymbol{A}\frac{\boldsymbol{p}}{\boldsymbol{T}}\right\|^2 + \ln \pi(p_0, b, T_0, \boldsymbol{h_T}, \boldsymbol{a_T})\Big\}, \tag{4.27}$$

conditioned on the ozone sample in Fig. 4.16 and a γ sample from the marginal posterior, and using the approximated forward model $\boldsymbol{A} = \boldsymbol{M}\boldsymbol{A}_L$. We will approximate this posterior with a TT and validate this approximation with samples from the posterior using the `t-walk` [23] implementation in Python [63]. "Conditioning on estimates gives poor predictive densities". [7]

Again, we define a grid with 25 grid points in each dimension, which also acts as the sampling space. Since we approximate a 16-dimensional function, we have to carefully choose a grid, as we do not want to approximate regions with low probability, and we like to keep the number of grid points low, as this increases computation time. We find the grid, see Tab. 4.2, iteratively by running the t-walk and then computing marginal distributions. Note that we bound the sampling space of the t-walk by the TT-grid. We run the `tt.cross.rectcross.rect_cross.cross` function from the `ttpy` python package [] with constant rank $r = 16$, equal to the dimension of the posterior. Next, we introduce a constant c in the posterior, which acts as a normalisation constant and is needed when approximating the square root of the posterior for pressure and temperature with a tensor-train (TT) to avoid underflow. Then the posterior becomes:

$$\pi(p_0, b, T_0, \boldsymbol{h_T}, \boldsymbol{a_T}|\boldsymbol{y}, \gamma, \boldsymbol{x}) \propto \exp\Big\{ -\frac{\gamma}{2}\left\|\boldsymbol{y} - \boldsymbol{A}\frac{\boldsymbol{p}}{\boldsymbol{T}}\right\|^2 + \ln \pi(p_0, b, T_0, \boldsymbol{h_T}, \boldsymbol{a_T}) + c\Big\}. \tag{4.28}$$

To find the constant c, we evaluate the logarithm of the posterior on 5000 random points and calculate the maximum $c_{\max} < 0$ of those 5000 points. Then we set the constant to a value which pushes the posterior close to the upper numerical limit of our machine, which is approximately e^{700}. Since we approximate the square root, we conservatively set the constant to $c = -c_{\text{diff}} + 325$. It takes roughly 3 to 4min for 15 sweeps by the `cross` to find the optimal tensors. Then we can compute the marginal as in Sec. 2.3, where we set $\xi = 1/\lambda(\mathcal{X})$.

For comparison, we run the t-walk on the posterior as defined in Eq. 4.27 for 5×10^6 steps plus a burn-in period of 10000, which takes around 7 mins on the same laptop. We plot the resulting histograms in Fig. 4.18 to 4.22; additionally, we plot the trace of the samples in Fig. **??**. The integrated autocorrelation times (IACT) for the hyper-parameters range from 0 to 1000 and are summarised in Tab. 4.2.

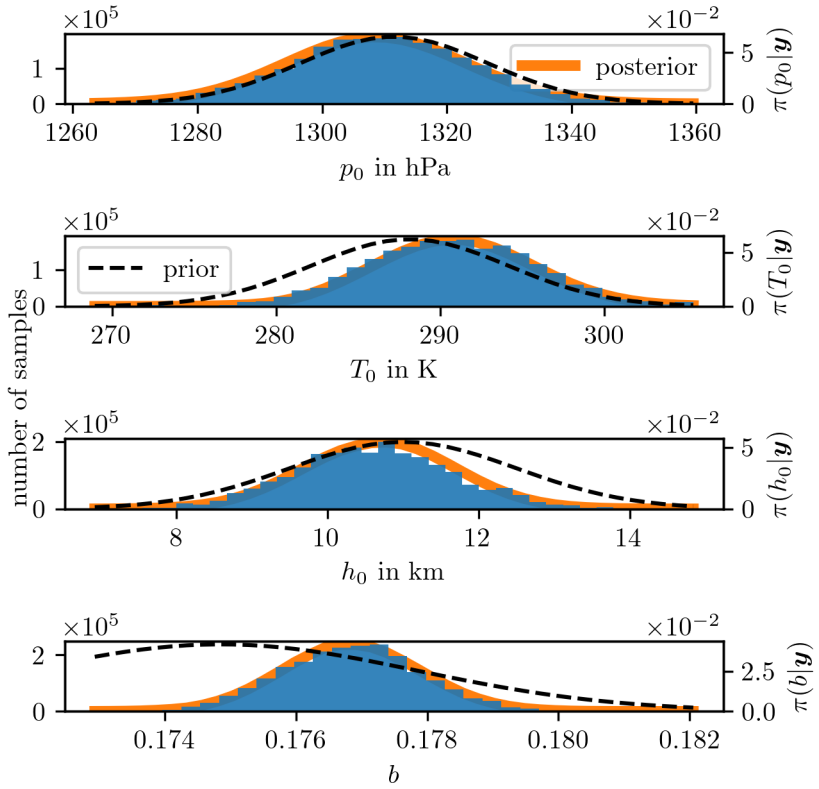

Figure 4.18: We plot the TT approximation of marginal posterior in orange and the samples as a histogram as well as the prior distribution with a dotted line.

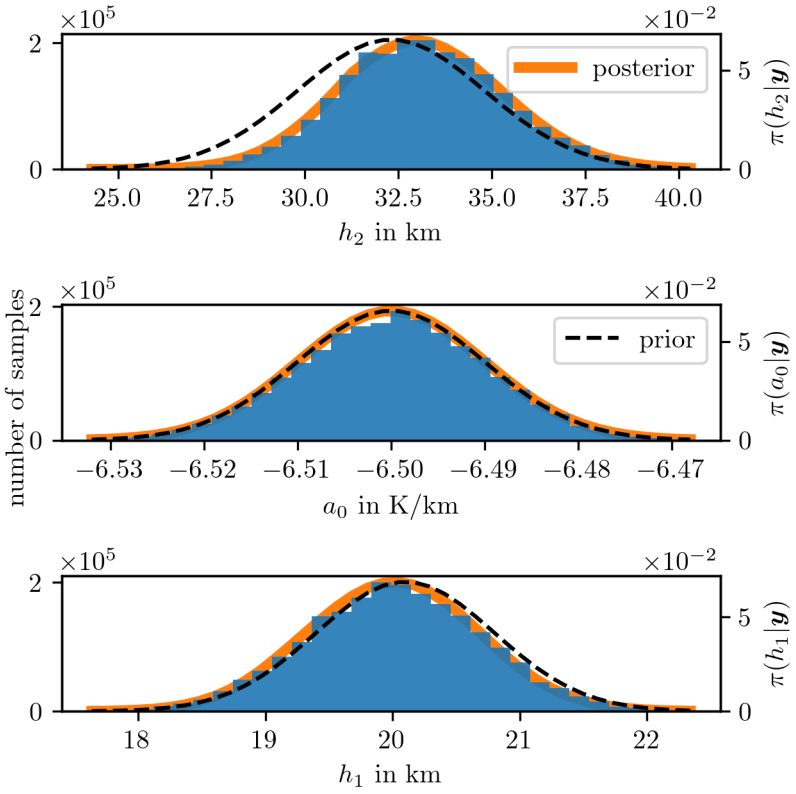

Figure 4.19: We plot the TT approximation of marginal posterior in orange and the samples as a histogram as well as the prior distribution with a dotted line.

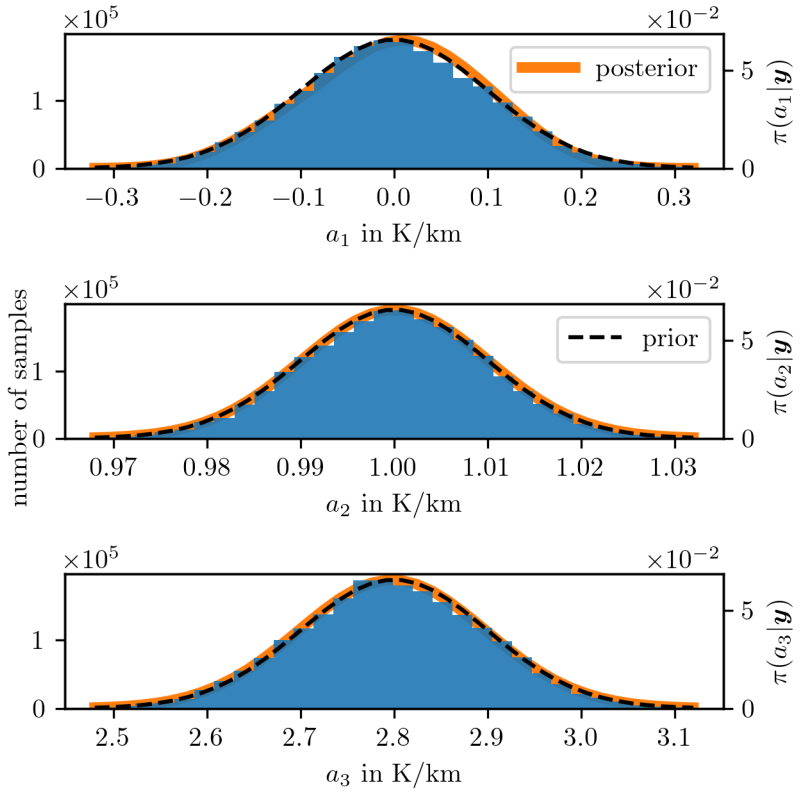

Figure 4.20: We plot the TT approximation of marginal posterior in orange and the samples as a histogram as well as the prior distribution with a dotted line.

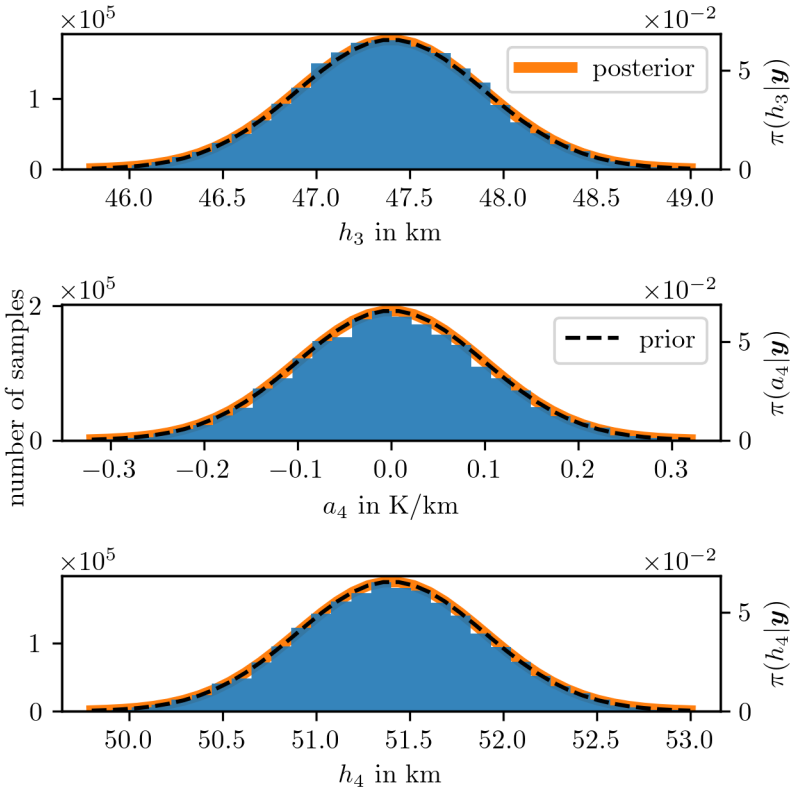

Figure 4.21: We plot the TT approximation of marginal posterior in orange and the samples as a histogram as well as the prior distribution with a dotted line.

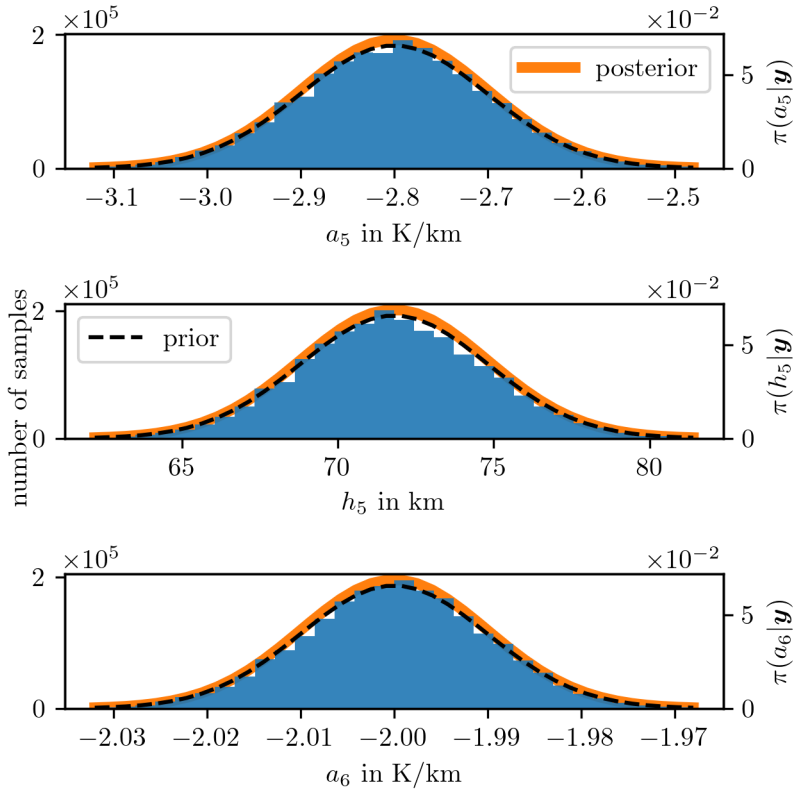

Figure 4.22: We plot the TT approximation of marginal posterior in orange and the samples as a histogram as well as the prior distribution with a dotted line.

To obtain temperature and pressure profiles, we can either take samples from the output of the t-walk or generate random values between 0 and 1 and compare them to the cumulative distribution functions. We plot the posterior temperature and pressure profiles in Fig. 4.23 and Fig. 4.24.

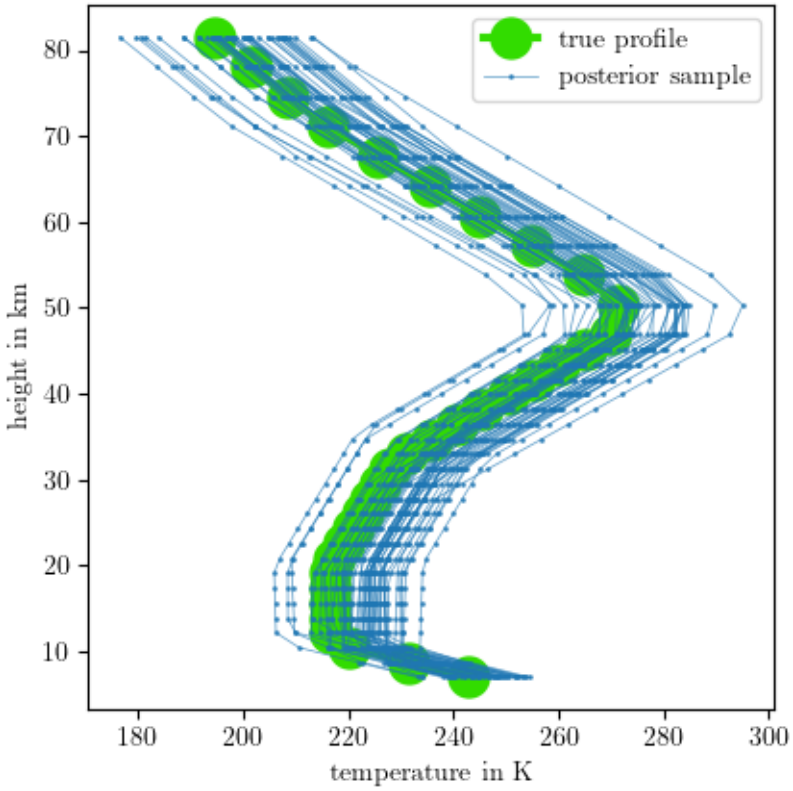

Figure 4.23: We take samples from the posterior distribution, as plotted in Figures 4.18 to 4.21 and plot the corresponding temperature function, see Eq: 4.3.

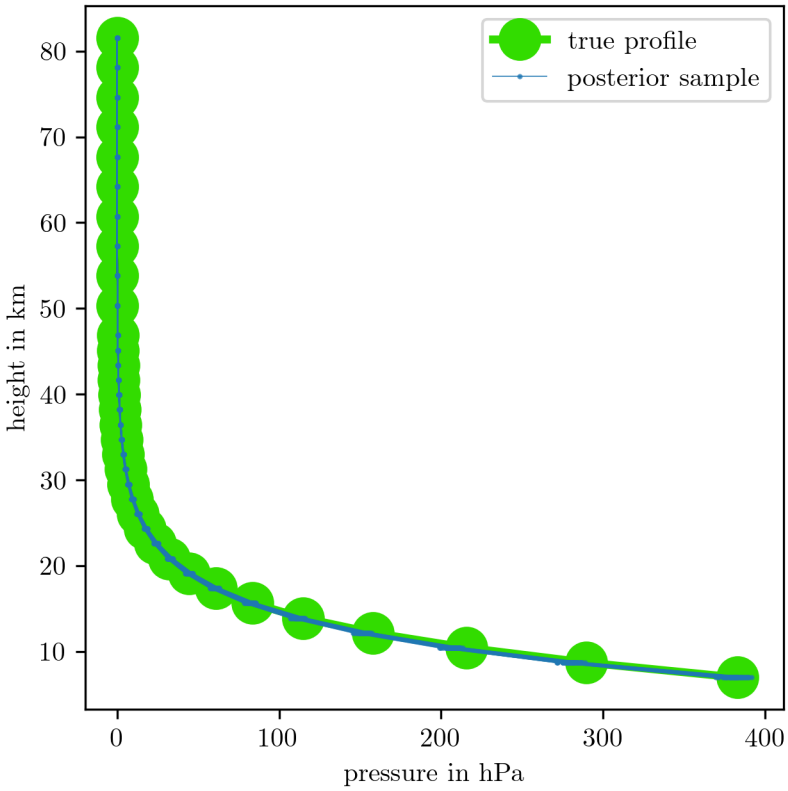

Figure 4.24: We take samples from the posterior distribution, as plotted in Fig. 4.22 and plot the corresponding pressure function, see Eq: 4.16.

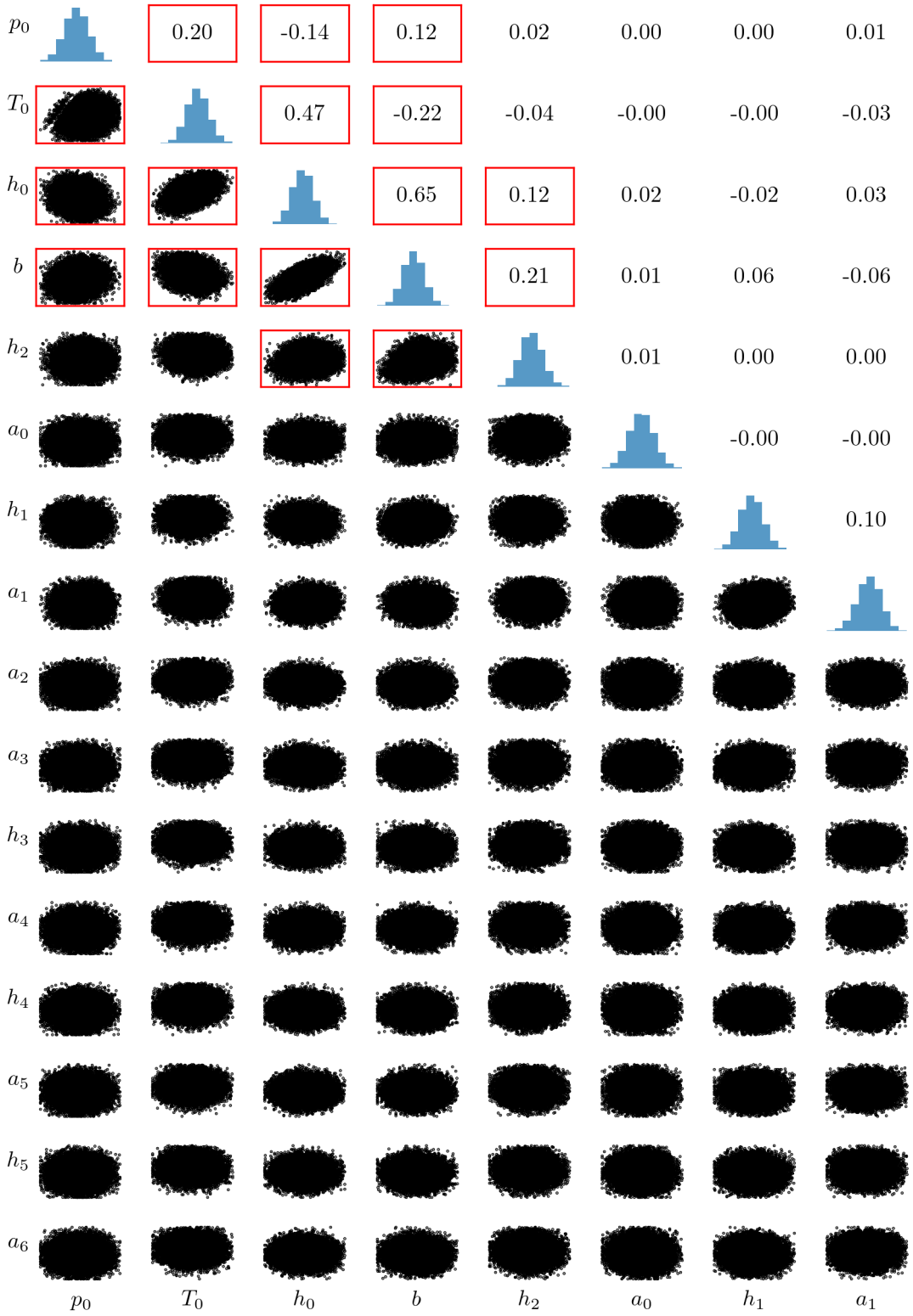

Figure 4.25: mffjnjf

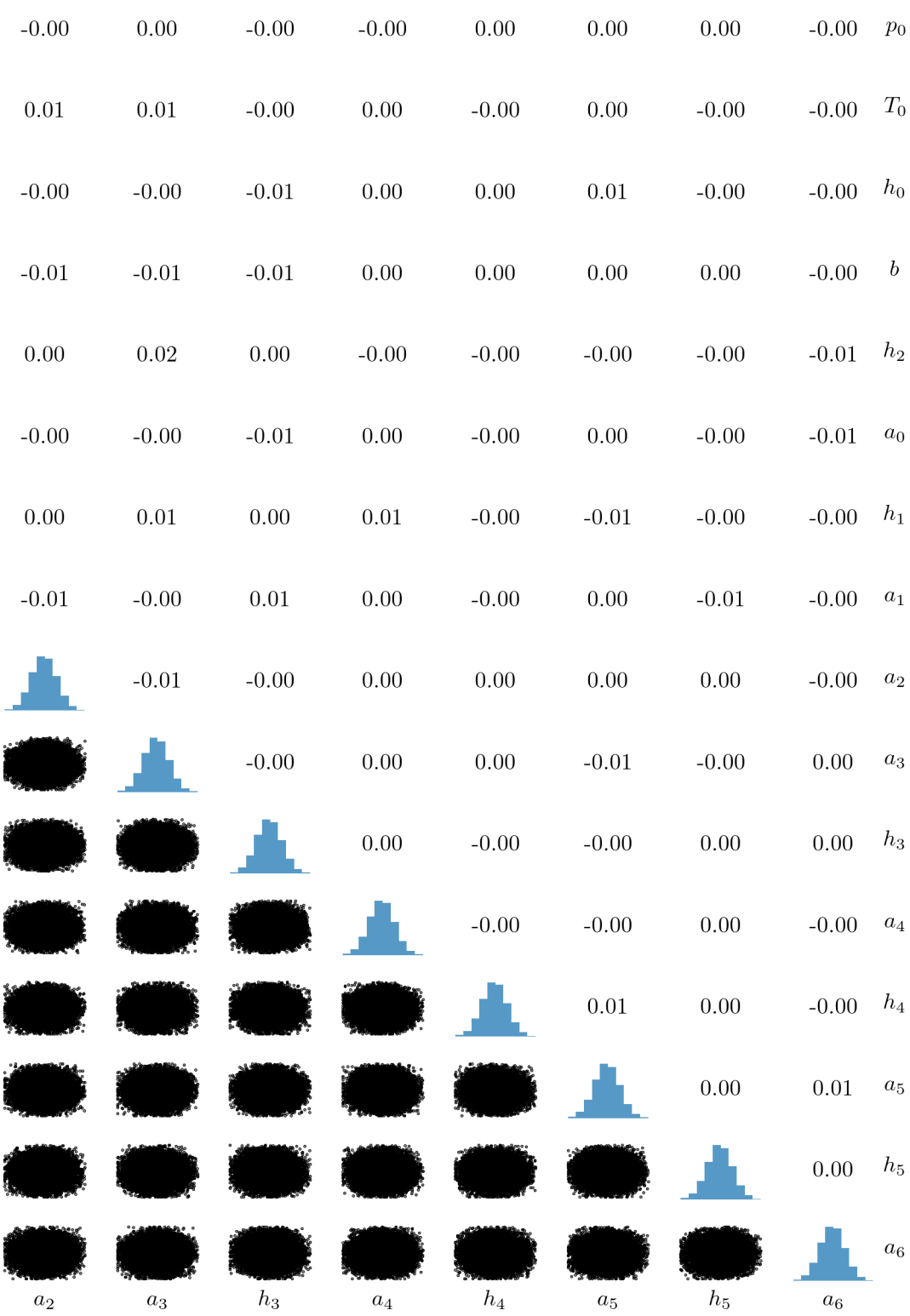
-0.00 0.00 -0.00 -0.00 0.00 0.00 0.00 -0.00 p_0
0.01 0.01 -0.00 0.00 -0.00 0.00 -0.00 -0.00 T_0
-0.00 -0.00 -0.01 0.00 0.00 0.01 -0.00 -0.00 h_0
-0.01 -0.01 -0.01 0.00 0.00 0.00 0.00 -0.00 b
0.00 0.02 0.00 -0.00 -0.00 -0.00 -0.00 -0.01 h_2
-0.00 -0.00 -0.01 0.00 -0.00 0.00 -0.00 -0.01 a_0
0.00 0.01 0.00 0.01 -0.00 -0.01 -0.00 -0.00 h_1
-0.01 -0.00 0.01 0.00 -0.00 0.00 -0.01 -0.00 a_1
-0.01 -0.00 0.00 0.00 0.00 0.00 -0.00 a_2
-0.00 0.00 0.00 -0.01 -0.00 0.00 a_3
0.00 -0.00 -0.00 0.00 0.00 h_3
-0.00 -0.00 0.00 -0.00 a_4
0.01 0.00 -0.00 h_4
0.00 0.01 a_5
0.00 h_5
a_6
a_2 a_3 h_3 a_4 h_4 a_5 h_5 a_6

fhgffg

4.8 Error analysis

In this section, we estimate errors due to the function approximations of $f(\lambda)$ and $g(\lambda)$ and how these errors propagate to the marginal posterior. Additionally, we approximate errors of the TT-approximation as well as Monte-Carlo errors when binning up the samples.

Error due to Approximation of f and g

When approximating the functions $f(\lambda)$ and $g(\lambda)$, we find that the 3rd-order Taylor series of $f(\lambda)$ and a linear approximation of $g(\lambda)$ in log-space give the smallest error. The Taylor series truncation error of $f(\lambda)$ is bounded by the fourth order Taylor series $E_f = \arg\max_{\lambda} f^{(4)}(\lambda_0)/4!\,(\lambda - \lambda_0)^4$ and corresponds to an relative error bounded by 20%. Since the maximum absolute error of the approximation $\arg\max_{\lambda} |\tilde{g}(\lambda) - g(\lambda)| \approx 1$ corresponds to an relative error of approximately 0.3% and is small compared to $E_f \approx 1e8$ we ignore the approximation error of $g(\lambda)$. Then the maximum relative propagation error $\arg\max_{\lambda,\gamma} 0.5\gamma E_f / \log \pi(\lambda, \gamma|\boldsymbol{y})$ is bound by approximately 5%.

Tensor-train approximation error for the marginal posterior

We calculate the error of the TT approximation of the marginal posterior with the Wasserstein distance $||x||$. The wasserstein distance between the normalised true marginal posterior $\pi(\lambda, \gamma|\boldsymbol{y})$ and the TT approximation $\tilde{\pi}(\lambda, \gamma|\boldsymbol{y})$ is 0.1.

Error due to grid size

When we calculate the mean and covariance matrix of the full conditional $\pi(\boldsymbol{x}|\boldsymbol{y})$ we have to bin up the samples of the marginal posterior $\pi(\gamma, \delta|\boldsymbol{y})$ or use a TT approximation on a predefined grid with a certain number of grid points, we like to give an estimate for this error as well. In doing we bin up samples and use the height $\tilde{\pi}(\boldsymbol{\theta}_d^{(k)})$ for a bin $k = 1, \ldots, \mathrm{N}_b$ to calculate the mean $\tilde{\mu}_d = \sum_{\mathrm{N}_b} \tilde{\pi}(\boldsymbol{\theta}_d^{(k)})$. We compare to the sample mean $\boldsymbol{\mu}_d = \sum_{k=1}^{N} \boldsymbol{\theta}_d^{(k)}/N$ and calculate the relative error $||\boldsymbol{\mu}_{\text{samp}} - \boldsymbol{\mu}_{\text{distr}}||/||\boldsymbol{\mu}_{\text{samp}}||$ where $\boldsymbol{\mu}_{\text{samp}} = (\tilde{\mu}_1, \ldots, \tilde{\mu}_D)$ and equivalently $\boldsymbol{\mu}_{\text{distr}} = (\tilde{\mu}_1, \ldots, \tilde{\mu}_D)$. Here d refers to the $D = 16$ hyper-parameters $\gamma, \lambda, h_1, h_2, h_3, h_4, h_5, h_6, a_0, a_1, a_2, a_3, a_4, T_0, p_0, b$.

The relative error behaves proportionally to $1/N$, see Fig. 4.26 and Eq. A.11, and we consider a relative error less than 0.1% good enough. This happens roughly at a bin size of 25, which is our TT grid size. Note that we exclude the error due to τ_{int} the IACT and that we choose the grid according to the sampled values so that the sampling region is the same as the region in which we approximate the posterior distributions. .

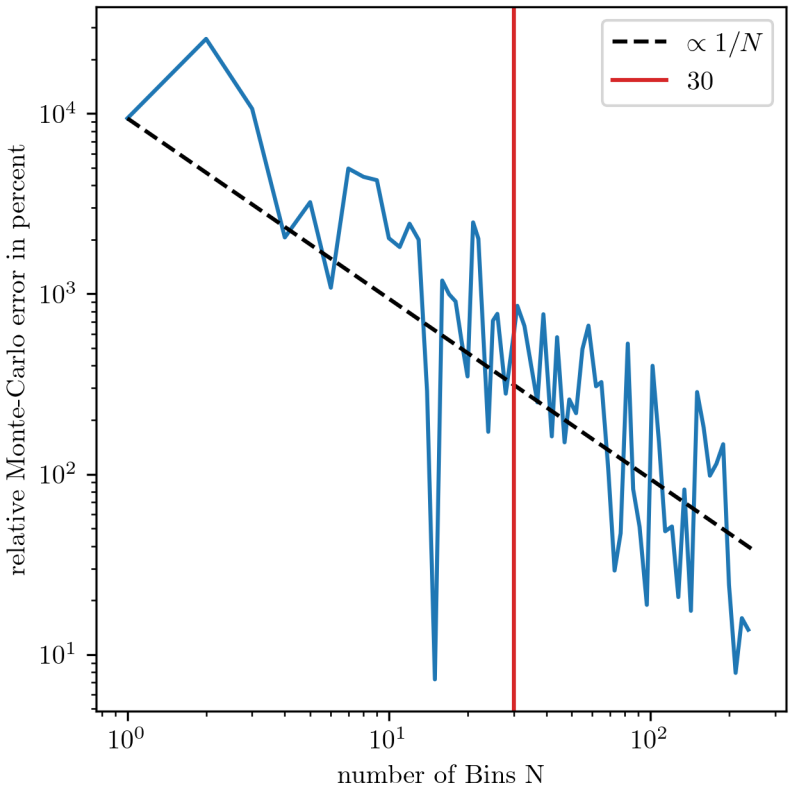

Figure 4.26: Assessment of Monte-Carlo error, where we calculate the relative error of the mean due to binning up the samples compared to the sample mean $||\boldsymbol{\mu}_{\text{samp}} - \boldsymbol{\mu}_{\text{distr}}||/||\boldsymbol{\mu}_{\text{samp}}||$.

5 Summary and Outlook

In this chapter we draw conclusion based on the results from the previous chapter. We compare the regularised solution to the mean and to the samples from the full posterior. We elaborate on the occurring approximation errors. We compare the marginal posterior distributions based on the drawn samples and from the TT-decomposition. While elaboration about the different methods, we also elaborate on how informative the data and what the means in terms of ozone, pressure and temperature profile.

5.1 Regularisation vs MTC

As already mentioned the regularisation approach only provides on solution, see Fig. 4.16. In Fig. 4.14 we plot samples from the full conditional, which lay above L-Curve and make sense in terms of the Lagrange multipliers as the point on the L-Curve can be seen as extreme values. So the regularised estimate does not correlate to posterior solutions of the inverse problem. We note that the mean of full conditional is very similar to the regularised solution but is also some sort of an extreme value.

In comparison to the regularisation solution we can provide the mean and variance of the full conditional posterior distribution, as well as the sample mean.

5.2 Sampling vs TT

We can conclude that the TT approximation is faster or as fast as sampling methods. For the marginal posterior $\pi(\gamma, \lambda|\boldsymbol{y})$ the calculation of the TT-cores takes 0.1s, which we consider similar to the sampling time of 0.5s. But the TT approximation needs less function evaluations than the MWG sampler. More precisely, the TT needs $n_{\text{tot}} =$

$2n_{\text{sweeps}}((d-2)r^2n + 2nr) = 400$ function evaluations, with number of sweeps $n_{\text{sweeps}} = 2$ and rank $r = 10$ and grid size $n = 25$ compared to 10000 samples.

When approximating the posterior distribution of the temperature pressure ratio we are much faster compared to sampling methods. Since the parameter space is 16-dimensional we have to run the t-walk for about 2 million steps. In addition of checking the trace of the samples, we also estimate the IATC with [56] see Tab. 4.2. Since for shorter chains with a sample size of 10^6 the error for the IATC estimate is much larger we decide to a sample size of $4 \cdot 10^6$ is sufficient. This comes with a sampling time of 20mins, much larger compare to the 2.5min. Which makes sense as we need $n_{\text{tot}} = 2n_{\text{sweeps}}((d-2)r^2n + 2nr) = 384838438$ function evaluations. We also note that we do run into problems especially in higher dimensional functions as we have a large range of values and hence introduce the constant c as already mentioned. The t-walk is more robust but the TT approximation is faster.

But both the samples and the TT approximation point towards the same results.

Reduce correlation structure by rotating coordinate system

5.3 Approximation Errors

We consider the approximation errors of the functions $f(\lambda)$, $g(\lambda)$ and propagation error into the marginal posterior for sampling of about 10% good enough. The TT approximation error from the marginal posterior is with about 10% also good enough since we do not believe that our model is accurate enough to capture those differences.

When approximation the affine map we get an relative error of about 0.4%, which is much smaller than the relative difference in between noise free and noisy data of approximately of 1.7%. We like to note that the relative difference The error linear to non-linear. Low rank bound as in [64]

5.4 Atmospheric Physics

Here we want to say how informative the data is and what we can about the ozone pressure and temperature profiles.

So all the samples as in Fig. 4.16 and Fig. 4.11, present valid solutions to the inverse problem. Hence, we can see that the variability of ozone in the upper atmosphere is large and that we do not capture the ozone peak around 80km. The posterior temperature profiles is similar to the prior profiles, as also seen in marginal posterior Fig. 4.18 to 4.22. We can already see that in the prior analys, as the pressure temperature ratio does inherit the exponential structure of the pressure profile. So the posterior pressure profile is much more informative, see marginal for b in Fig. 4.22. So we can retrieve an informative pressure profile for the pressure but not for temperature.

Ideally we should do this iteratively update ozone and then temperature and pressure until proven convergence.

6 Outlook

6.1 Measurement Device

Then we can include more measurement specific details such as the pointing accuracy. Then we could sample measurement N_Γ geometries $\Gamma^{(k)} \sim \pi(\Gamma)$ so that the posterior $\pi(\boldsymbol{x}|\boldsymbol{y}) \approx 1/N_\Gamma \sum_\Gamma \pi(\boldsymbol{x}, \Gamma^{(k)}|\boldsymbol{y})$ and include other measurement device specific parameters.

6.2 Methods

Here we point out possibilities for improvement of the currently used methods

6.2.1 TT approximation

Within the TT approximation we run into numerical problems. One way of solving this issue could be to use a different basis set such as Lagrange polynomials as these exactly fit to a Gaussian or Chebychev polynomial as basis functions. Another idea is to use different reference measure for integration, such as a Gaussian measure instead of the current Lebesgue measure. Or that the TT finds normalisation constants automatically.

6.2.2 Sampling

The t-walk is a robust easy to implement sampling method, of course one could employ a more efficient sampler such as a gibbs sampler or something similar [].

6.2.3 Model

Since we have to truncate the full conditional at the end the model is not accurate enough to eliminate those values. This was to show that we can to a more comprehensive analysis

compared to a regularised method. Ideally we like to use a more accurate model where we parametrise ozone, similar to the pressure and temperature profile. In doing so one would has to know much more about ozone in different altitudes. Then we possibly could employ a different graph Laplacian based on a different structure of ozone. And when we approximate the non-linear forward map with a affine map using a linear solver we could of course use other methods such as the machine learning methods.

References

[1] Bryan Duncan. *Aura at 20 Years.* https://science.nasa.gov/science-research/earth-science/aura-at-20-years/. [Online; accessed 31/08/25]. NASA's Goddard Space Flight Center (GSFC), 2024.

[2] Susan L Ustin and Elizabeth McPhee Middleton. "Current and near-term Earth-observing environmental satellites, their missions, characteristics, instruments, and applications". In: *Sensors* 24.11 (2024), p. 3488.

[3] Mallika Irene Suresh et al. "Multichannel upconversion of terahertz radiation in an optical disk resonator". In: *Opt. Express* 33.5 (2025), pp. 10302–10311.

[4] Florian Sedlmeir et al. "Detecting THz in the telecom range: All resonant THz up-conversion in a whispering gallery mode resonator". In: *2014 39th International Conference on Infrared, Millimeter, and Terahertz waves (IRMMW-THz)*. 2014, pp. 1–2.

[5] Clive D Rodgers. "Retrieval of atmospheric temperature and composition from remote measurements of thermal radiation". In: *Reviews of Geophysics* 14.4 (1976), pp. 609–624.

[6] Nathaniel J. Livesey et al. *Earth Observing System (EOS) Microwave Limb Sounder (MLS) Version 5.0x Level 2 and 3 data quality and description document.* Version 5.0-1.1a. NASA Goddard Earth Sciences Data and Information Services Center, 2022.

[7] Sze M Tan, Colin Fox, and Geoff K. Nicholls. *Course notes for ELEC 445 – Inverse Problems and Imaging.* https://coursesupport.physics.otago.ac.nz/wiki/pmwiki.php/ELEC445/HomePage. [Online; accessed 10/12/23]. Physics Department, University of Otago, 2016.

[8] Nathaniel J Livesey et al. "Retrieval algorithms for the EOS Microwave limb sounder (MLS)". In: *IEEE Transactions on Geoscience and Remote Sensing* 44.5 (2006), pp. 1144–1155.

[9] Schwartz M. et al. *MLS/Aura Level 2 Ozone (O3) Mixing Ratio V005.* https://disc.gsfc.nasa.gov/datasets/ML2O3_005/summary?keywords=mls%20o3. [Online; accessed 25/04/24]. NASA Goddard Earth Sciences Data and Information Services Center, 2020.

[10] F. Werner et al. "Applying machine learning to improve the near-real-time products of the Aura Microwave Limb Sounder". In: *Atmospheric Measurement Techniques* 16.11 (2023), pp. 2733–2751.

[11] Pasquale Sellitto et al. "Neural network algorithms for ozone profile retrieval from ESA-envisat sciamachy and NASA-AURA OMI satellite data". In: vol. 3. Aug. 2008, pp. III –170.

[12] Colin Fox and Richard A Norton. "Fast sampling in a linear-Gaussian inverse problem". In: *SIAM/ASA Journal on Uncertainty Quantification* 4.1 (2016), pp. 1191–1218.

[13] Gareth O. Roberts and Jeffrey S Rosenthal. "General state space Markov chains and MCMC algorithms". In: *Probability Surveys* 1 (2004), pp. 20–71.

[14] S. P. Meyn and R.L. Tweedie. *Markov Chains and Stochastic Stability. 2nd Edition.* New York: Cambridge University Press, 2009.

[15] Havard Rue and Leonhard Held. *Gaussian Markov random fields: theory and applications.* London: CRC press, 2005.

[16] Richard A Norton, J Andrés Christen, and Colin Fox. "Sampling hyperparameters in hierarchical models: improving on Gibbs for high-dimensional latent fields and large datasets". In: *Communications in Statistics-Simulation and Computation* 47.9 (2018), pp. 2639–2655.

[17] Charles W. Champ and Andrew V. Sills. "The Generalized Law of Total Covariance". In: *preprint* (2022).

[18] Charles J Geyer. "Practical markov chain monte carlo". In: *Statistical science* (1992), pp. 473–483.

[19] U. Wolff and B. Bunk. *Lecture Notes on Computational Physics II [in german]*. `www-com.physik.hu-berlin.de/comphys/comphys.htm`. [Online; accessed 29/08/25]. Humboldt University, Berlin, 2016.

[20] A. Sokal. "Monte Carlo Methods in Statistical Mechanics: Foundations and New Algorithms". In: *Functional Integration: Basics and Applications*. Ed. by Cecile DeWitt-Morette, Pierre Cartier, and Antoine Folacci. Boston, MA: Springer US, 1997, pp. 131–192.

[21] Daniel Simpson, Finn Lindgren, and Håvard Rue. "Think continuous: Markovian Gaussian models in spatial statistics". In: *Spatial Statistics* 1 (2012), pp. 16–29.

[22] Gareth O. Roberts and Jeffrey S Rosenthal. "Harris recurrence of Metropolis-within-Gibbs and trans-dimensional Markov chains". In: *The Annals of Applied Probability* 16.4 (2006), 2123–2139.

[23] J. Andrés Christen and Colin Fox. "A general purpose sampling algorithm for continuous distributions (the t-walk)". In: *Bayesian Analysis* 5.2 (2010), pp. 263 –281.

[24] Tiangang Cui and Sergey Dolgov. "Deep composition of tensor-trains using squared inverse rosenblatt transports". In: *Foundations of Computational Mathematics* 22.6 (2022), pp. 1863–1922.

[25] M. Capiński and P.E. Kopp. *Measure, Integral and Probability. Springer Undergraduate Mathematics Series*. London: Springer-Verlag London, 2004.

[26] M. Simonnet. *Measures and Probabilities*. New York: Springer-Verlag, 1996.

[27] Vesa Kaarnioja. *Inverse Problems. Eighth lecture*. `https://vesak90.userpage.fu-berlin.de/ip23/week8.pdf`. [Online; accessed 10/04/25]. Freie Universität Berlin, Department of Mathematics and Computer Science, 2023.

[28] Philip J Davis and Philip Rabinowitz. *Methods of numerical integration*. San Diego, CA: Academic Press, Inc., 1984.

[29] Sergey Dolgov et al. "Approximation and sampling of multivariate probability distributions in the tensor train decomposition". In: *Statistics and Computing* 30 (2020), pp. 603–625.

[30] Colin Fox et al. "Grid methods for Bayes-optimal continuous-discrete filtering and utilizing a functional tensor train representation". In: *Inverse Problems in Science and Engineering* 29.8 (2021), pp. 1199–1217.

[31] Ivan V Oseledets. "Tensor-train decomposition". In: *SIAM Journal on Scientific Computing* 33.5 (2011), pp. 2295–2317.

[32] Ivan Oseledets. "DMRG Approach to Fast Linear Algebra in the TT-Format". In: *Computational Methods in Applied Mathematics* 11.3 (2011), pp. 382–393.

[33] John Thickstun. *Kantorovich-rubinstein duality*. `https://courses.cs.washington.edu/courses/cse599i/20au/resources/L12_duality.pdf`. [Online; accessed 31/08/25]. University of Washington, 2019.

[34] Luigi Ambrosio, Elia Brué, and Daniele Semola. *Lectures on Optimal Transport*. Cham: Springer Nature Switzerland, 2024.

[35] Jean Feydy. "Analyse de données géométriques, au delà des convolutions". Thesis. Université Paris-Saclay, July 2020. URL: `https://theses.hal.science/tel-02945979`.

[36] Marcel Berger. *Geometry I. 4th Edition*. Berlin Heidelberg: Springer-Verlag, 2009.

[37] Katsumi Nomizu and Takeshi Sasaki. *Affine differential geometry*. Cambridge: Cambridge University Press, 1994.

[38] Per Christian Hansen. "Regularization, GSVD and truncated GSVD". In: *BIT numerical mathematics* 29.3 (1989), pp. 491–504.

[39] Per Christian Hansen. "The L-Curve and its Use in the Numerical Treatment of Inverse Problems". English. In: *Computational Inverse Problems in Electrocardiology*. Ed. by P. Johnston. WIT Press, 2001, pp. 119–142.

[40] Yu-Xiang Wang et al. "Trend Filtering on Graphs". In: *Journal of Machine Learning Research* 17.105 (2016), pp. 1–41.

[41] Per Christian Hansen and Dianne Prost O'Leary. "The use of the L-curve in the regularization of discrete ill-posed problems". In: *SIAM Journal on Scientific Computing* 14.6 (1993), pp. 1487–1503.

[42] KC Santosh, Nibaran Das, and Swarnendu Ghosh. "Chapter 3 - Deep learning models". In: *Deep Learning Models for Medical Imaging*. Ed. by KC Santosh, Nibaran Das, and Swarnendu Ghosh. Primers in Biomedical Imaging Devices and Systems. Academic Press, 2022, pp. 65–97.

[43] C. Readings. *Envisat MIPAS An Instrument for Atmospheric Chemistry and Climate Research*. Noordwijk: ESA Publications Division, 2000.

[44] Jae N. Lee and Dong L. Wu. "Solar Cycle Modulation of Nighttime Ozone Near the Mesopause as Observed by MLS". In: *Earth and Space Science* 7.4 (2020).

[45] Iouli E Gordon et al. "The HITRAN2020 molecular spectroscopic database". In: *Journal of Quantitative Spectroscopy and Radiative Transfer* 277 (2022), p. 107949.

[46] Marie Šimečková et al. "Einstein A-coefficients and statistical weights for molecular absorption transitions in the HITRAN database". In: *Journal of Quantitative Spectroscopy and Radiative Transfer* 98.1 (2006), pp. 130–155.

[47] George B. Rybicki and Alan P. Lightman. *Radiative processes in Astrophysics*. Weinheim: Wiley-VCH, 2004.

[48] W.G. Read et al. "The clear-sky unpolarized forward model for the EOS aura microwave limb sounder (MLS)". In: *IEEE Transactions on Geoscience and Remote Sensing* 44.5 (2006), pp. 1367–1379.

[49] Colin Fox. *Blokkurs on computing MCMC for inverse problems*. unpublished. Physics Department, University of Otago, 2025.

[50] Australian National Concurrent Design Facility. *CubeSat Microwave Radiometer Mission to Support Global Ozone Layer Monitoring. Concept Study - Summary Report*. unpublished, internal report. Canberra BC: UNSW Canberra Space, 2023.

[51] Joe W Waters et al. "The earth observing system microwave limb sounder (EOS MLS) on the Aura satellite". In: *IEEE Transactions on Geoscience and Remote Sensing* 44.5 (2006), pp. 1075–1092.

[52] N. J. Livesey et al. "Validation of Aura Microwave Limb Sounder O3 and CO observations in the upper troposphere and lower stratosphere". In: *Journal of Geophysical Research: Atmospheres* 113.D15 (2008).

[53] *U.S. Standard Atmosphere, 1976*. Washington, D.C.: United States. National Oceanic and Atmospheric Administration, United States Committee on Extension to the Standard Atmosphere, 1976.

[54] H.M. Pickett. “Microwave Limb Sounder THz module on Aura”. In: *IEEE Transactions on Geoscience and Remote Sensing* 44.5 (2006), pp. 1122–1130.

[55] L. Froidevaux et al. “Validation of Aura Microwave Limb Sounder stratospheric ozone measurements”. In: *Journal of Geophysical Research: Atmospheres* 113.D15 (2008).

[56] Ulli Wolff. *UWerr.m Version6*. `https://www.physik.hu-berlin.de/de/com/ALPHAsoft`. [Online; accessed 5/11/23]. Humboldt-Universität to Berlin, 2004.

[57] Josef Dick, Frances Y. Kuo, and Ian H. Sloan. “High-dimensional integration: The quasi-Monte Carlo way”. In: *Acta Numerica* 22 (2013), 133–288.

[58] Johnathan M Bardsley et al. “Randomize-then-optimize for sampling and uncertainty quantification in electrical impedance tomography”. In: *SIAM/ASA Journal on Uncertainty Quantification* 3.1 (2015), pp. 1136–1158.

[59] I. V. Oseledets et al. *ttpy - a Python implementation of the TT-toolbox*. `https://github.com/oseledets/ttpy`. [accessed 23/06/25]. 2018.

[60] Ivan Oseledets and Eugene Tyrtyshnikov. “TT-cross approximation for multidimensional arrays”. In: *Linear Algebra and its Applications* 432.1 (2010), pp. 70–88.

[61] Per Christian Hansen. *Discrete Inverse Problems: Insight and Algorithms*. Philadelphia: SIAM, 2010.

[62] Ville Satopäa et al. “Finding a "Kneedle" in a Haystack: Detecting Knee Points in System Behavior”. In: *2011 31st International Conference on Distributed Computing Systems Workshops*. IEEE. 2011, pp. 166–171.

[63] J. Andrés Christen and Colin Fox. *The t-walk software*. `https://www.cimat.mx/~jac/twalk/`. [Online; accessed 25/11/24]. CIMAT, Mexico, and University of Otago, New Zealand.

[64] Paul B. Rohrbach et al. “Rank Bounds for Approximating Gaussian Densities in the Tensor-Train Format”. In: *SIAM/ASA Journal on Uncertainty Quantification* 10.3 (2022), pp. 1191–1224.

[65] Greg Lawler. *Notes on probability*. `https://www.math.uchicago.edu/~lawler/probnotes.pdf`. [Online; accessed 10/04/25]. The University of Chicago, Department of Mathematics, 2016.

Appendices

A

Theoretical and technical background

A.1 Correlation Structure

In the book Gaussian Markov Random Fields [15], Rue and Held demonstrate that a strong correlation between the hyper-parameter μ and the latent field $\boldsymbol{x}$ can significantly slow down convergence when using samplers, in particularly Gibbs samplers. They consider the hierarchical model

$$\mu \sim \mathcal{N}(0, 1) \tag{A.1a}$$

$$\boldsymbol{x}|\mu \sim \mathcal{N}(\mu\mathbf{1}, \boldsymbol{Q}^{-1}), \tag{A.1b}$$

and apply a Gibbs sampler based on the full conditional distributions

$$\mu^{(k)}|\boldsymbol{x}^{(k)} \sim \mathcal{N}\left(\frac{\mathbf{1}^T\boldsymbol{Q}\boldsymbol{x}^{(k-1)}}{1+\mathbf{1}^T\boldsymbol{Q}\mathbf{1}}, \left(1+\mathbf{1}^T\boldsymbol{Q}\mathbf{1}\right)^{-1}\right) \tag{A.2}$$

$$\boldsymbol{x}^{(k)}|\mu^{(k)} \sim \mathcal{N}(\mu^{(k)}\mathbf{1}, \boldsymbol{Q}^{-1}). \tag{A.3}$$

As illustrated in Figure A.1, when the sampler is restricted to steps only in the μ-direction (horizontal axis) or the $\boldsymbol{x}$-direction (vertical axis), it requires many iterations to adequately explore the parameter space. This inefficiency arises from the high correlation between μ and $\boldsymbol{x}$, visible in Figure A.1 as a 'squeeze' of the distribution.

A solution to the slow mixing problem is to update $(\mu, \boldsymbol{x})$ jointly. Since here μ is one dimensional, effectively only marginal density of μ is needed.

$$\mu^\star \sim q(\mu^\star|\mu^{(k-1)}) \tag{A.4}$$

$$\boldsymbol{x}^{(k)}|\mu^\star \sim \mathcal{N}(\mu^\star\mathbf{1}, \boldsymbol{Q}^{-1}) \tag{A.5}$$

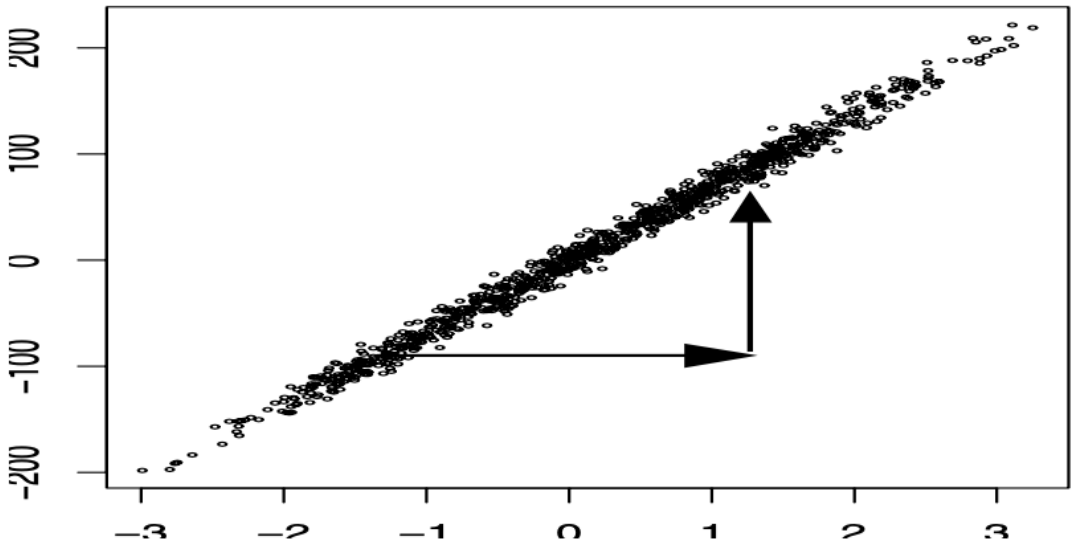

Figure A.1: The figure taken from [15, Figure 4.1 (b)], shows samples from a marginal chain for μ and $\mathbf{1}^T\boldsymbol{Q}\boldsymbol{x}^{(k)}$ over 1000 iterations, based on the hierarchical model in Eq. A.1, with an autoregressive process encoded in $\boldsymbol{Q}$. The algorithm updates μ and $\boldsymbol{x}$ successively from their full conditional distributions. The plot displays $(\mu^{(k)}, \mathbf{1}^T\boldsymbol{Q}\boldsymbol{x}^{(k)})$, with $\mu^{(k)}$ on the horizontal axis and $\mathbf{1}^T\boldsymbol{Q}\boldsymbol{x}^{(k)}$ on the vertical axis. The slow mixing and convergence of μ result from its strong dependence on $\mathbf{1}^T\boldsymbol{Q}\boldsymbol{x}^{(k)}$, while the sampler permits only axis-aligned (horizontal and vertical) and does not allow diagonal moves, as illustrated by the arrows.

With a simple MCMC algorithm targeting μ one can explore the sample space efficiently and only draw a corresponding sample for $\boldsymbol{x}$ from its full conditional once, for instance, the proposal $\mu^\star$ has been accepted.

A.2 On the Monte-Carlo Error and Integrated Autocorrelation time

To assess the error σ^2 of chain $\mathcal{M}_i$, we ignore systematic error due to initialisation bias (burn-in period), but we have to take into account that samples produced by any system or algorithm are correlated. To derive the integrated autocorrelation time (IATC), we follow the lecture notes [19]. In general, the error of a Monte-Carlo-based estimate from a sample set $\mathcal{M}_i = \{\boldsymbol{x}^{(1)}, \ldots, \boldsymbol{x}^{(k)}, \ldots, \boldsymbol{x}^{(s)}, \ldots, \boldsymbol{x}^{(N)}\} \sim \pi(\boldsymbol{x}|\boldsymbol{y})$ is:

$$(\sigma^{(i)})^2 = \mathrm{var}(\boldsymbol{\mu}^{(i)}_{\mathrm{samp}}) = \mathrm{var}(\mathrm{E}_{\boldsymbol{x}|\boldsymbol{y}}[h(\boldsymbol{x})]) = \left(\frac{1}{N}\sum_{k=1}^{N} h(\boldsymbol{x}^{(k)}) - \boldsymbol{\mu}^{(i)}\right)^2. \tag{A.6}$$

Expanding this summation, we see that

$$(\sigma^{(i)})^2 = \frac{1}{N^2}\sum_{k,s=1}^{N} \Gamma(k-s) \tag{A.7}$$

with the auto correlation coefficient $\Gamma(k-s) = (h(\boldsymbol{x}^{(k)}) - \boldsymbol{\mu}^{(i)})(h(\boldsymbol{x}^{(s)}) - \boldsymbol{\mu}^{(i)})$. Next we rewrite

$$\sum_{k,s=1}^{N} \Gamma(k-s) = \mathrm{var}(\boldsymbol{\mu}_{\mathrm{samp}}^{(i)}) \sum_{k,s=1}^{N} \frac{\Gamma(k-s)}{\Gamma(0)} = \mathrm{var}(\boldsymbol{\mu}_{\mathrm{samp}}^{(i)}) \sum_{k,s=1}^{N} \rho(k-s)\,, \tag{A.8}$$

with the normalised auto correlation coefficient $\rho(k-s) = \Gamma(k-s)/\Gamma(0)$ at lag $k-s$ and $\Gamma(0) = \mathrm{var}(\boldsymbol{\mu}_{\mathrm{samp}}^{(i)})$ for $k = s$. Typically $\Gamma(t)$ decays exponentially so that $\Gamma(t) \overset{t\to\infty}{\propto} \exp\{-t/\tau\}$ and for positive τ and $N \gg \tau$ we can approximate

$$\sum_{k,s=1}^{N} \rho(k-s) = N \sum_{t=-(N-1)}^{N-1} \left(1 - \frac{t}{N}\right)\rho(t) \approx N \sum_{t=-\infty}^{\infty} \rho(t) \coloneqq 2N\tau_{\mathrm{int}}\,, \tag{A.9}$$

see [20], and define the IATC as in [19, pp. 103-105]. If $\tau \gg 1$ one can show that $\tau_{\mathrm{int}} \approx \tau$

$$\sum_{t=-\infty}^{\infty} \rho(t) = 1 + 2\sum_{t=1}^{\infty} \left(e^{-1/\tau}\right)^t = 1 + 2\frac{e^{-1/\tau}}{1-e^{-1/\tau}} \approx 1 + 2\frac{1-1/\tau}{1/\tau} = 2\tau - 1 \approx 2\tau_{int} \tag{A.10}$$

where we use the geometric power series $\sum_{n=0}^{\infty} x^n = 1/(1+x)$ and the Taylor series $e^x \approx 1 + x$ for small x. Consequently, the estimate for the Monte-Carlo error is:

$$(\sigma^{(i)})^2 \approx \frac{\mathrm{var}(h(\boldsymbol{x}))}{N} \underbrace{\sum_{t=-\infty}^{\infty} \rho(t)}_{\coloneqq 2\tau_{\mathrm{int}}} = \mathrm{var}(h(\boldsymbol{x}))\frac{2\tau_{\mathrm{int}}}{N}\,, \tag{A.11}$$

where we define the IACT provides a good estimate of how many steps the sampling algorithm needs to take to produce one independent sample. More specifically, the effective sample size $\frac{2\tau_{\mathrm{int}}}{N}$ gives an estimate of how efficient a sampler is.

A.3 Measure theory

Recall the probability space $(\Omega, \mathcal{F}, \mathbb{P})$, where Ω denotes the sample space, and $\mathcal{F}$ is a collection of countable subsets $\{A_n\}_{n\in\mathbb{N}}$ of Ω. Each $A_n \subseteq \Omega$ is called an event, and a map $\mathbb{P} : \mathcal{F} \to \mathbb{R}$ is referred to as a measure. In the following, we describe the conditions required for $\mathcal{F}$ to be a σ-algebra, and for $\mathbb{P}$ to qualify as a probability measure. We refer to [65] [25] for further reading.

A.3.1 Probability Measure

For a probability measure, we require:

- $\mathbb{P}(\Omega) = 1$ and $\mathbb{P}(\emptyset) = 0$
- $\mathbb{P}(A) \in [0, 1]$

- $\mathbb{P}(\bigcup_{j\in\mathbb{N}} A_j) = \sum_{j\in\mathbb{N}} \mathbb{P}(A_j)$ if we have pairwise disjoint sets or $A_i \cap A_j = \emptyset$ for $i \neq j$

In other words, the probability assigned to the entire sample space must be equal to one, $\mathbb{P}(\Omega) = 1$, and the probability of the empty set must be zero, $\mathbb{P}(\emptyset) = 0$. For any subset $A \subseteq \Omega$, the probability $\mathbb{P}(A)$ must lie between zero and one, i.e., $\mathbb{P}(A) \in [0, 1]$. If e.g. two subsets A and B are disjoint (i.e., $A \cap B = \emptyset$), then the probability of their union satisfies $\mathbb{P}(A \cup B) = \mathbb{P}(A) + \mathbb{P}(B)$. This property must also hold for a countable sequence of disjoint sets $\{A_j\}_{j\in\mathbb{N}}$, such that $\mathbb{P}\left(\bigcup_{j\in\mathbb{N}} A_j\right) = \sum_{j\in\mathbb{N}} \mathbb{P}(A_j)$.

A.3.2 σ-Algebra

A collections of subsets $\mathcal{F}$ is called σ-algebra if:

- $\emptyset, \Omega \in \mathcal{F}$,
- if $A \in \mathcal{F}$ then $A^C \coloneqq A/\Omega \in \mathcal{F}$
- if $A_1, A_2, \cdots \in \mathcal{F}$ then $\bigcup_{j\in\mathbb{N}} A_j \in \mathcal{F}$

In other words, the empty set $\emptyset$ and the entire sample space Ω must always be elements of $\mathcal{F}$. If a set $A \in \mathcal{F}$, then its complement $A^C = \Omega \setminus A$ must also be in $\mathcal{F}$. If, in terms of a probability measure, we are able to assign a probability $\mathbb{P}(A)$ to an event A, we must also be able to assign a probability to the event "not A", i.e., $\mathbb{P}(A^C)$. Finally, if a countable collection of sets $A_1, A_2, \cdots \in \mathcal{F}$, then their union $\bigcup_{j\in\mathbb{N}} A_j$ must also be in $\mathcal{F}$. These three properties define the requirements for $\mathcal{F}$ to be a σ-algebra.

A.4 Python Code

18.0pt plus 2.0pt minus 1.0pt

```python
def MargBack(TTCore, univarGrid):
  ''' Backward marginalisation, see Prop. ?? as in SIRT from Cui et al. [24] '''

  dim = len(univarGrid)
  B = dim * [None]  # coeffTensor
  B[-1] = TTCore[-1]
  R = [None] * dim
  C = [None] * dim

  for k in range(dim - 1, 0, -1):
    r_kmin1, n, r_k = np.shape(TTCore[k])
    # !! we set Lebesgue Measure to const = one
    M = np.identity(n) * (univarGrid[k][-1] - univarGrid[k][0])  # Mass matrix
    L = scy.linalg.cholesky(M)

    # construct Tensor C Eq. (27)
    C[k] = np.zeros((r_kmin1, n, r_k))
    for alpha in range(0, r_kmin1):
      for l in range(0, r_k):
        C[k][alpha, :, l] = B[k][alpha, :, l] @ L[:, :]

    # unfold along first coordinate and compute thin QR decomposition of C^T
    # Eq. (28)
    Q, R[k] = np.linalg.qr(C[k].reshape((r_kmin1, n * r_k), order='C').transpose()
    , mode='reduced')

    # compute next coefficient tensor
    # Eq. (29)
    r_kmin2, n, r_kmin1 = np.shape(TTCore[k - 1])
    B[k - 1] = np.zeros(np.shape(TTCore[k - 1]))
    for alpha_2 in range(0, r_kmin2):
    #for i in range(0, n):
      for l_1 in range(0, r_kmin1):
        B[k - 1][alpha_2, :, l_1] = TTCore[k - 1][alpha_2, :, :] @ R[k][l_1, :]

return B
```

Listing A.1: Python example

```python
def SIRT(seeds, SQTT, univarGrid, BackMarg, absError):
  ''' do squared inverse rosenblatt transform SIRT as in Cui et al. [24] '''

  dim, numbSampl = seeds.shape
  samples = np.zeros(seeds.shape)
  probVal = np.zeros(seeds.shape)
  Approx = np.zeros(seeds.shape[1])

  # lebesgue measure for qudrature
  WholeLebLam = np.zeros(dim)
  for k in range(0, dim):
    WholeLebLam[k] = (univarGrid[k][-1] - univarGrid[k][0])
  lamX = np.ones(dim)
  for k in range(1, dim):
    lamX[k - 1] = np.prod(WholeLebLam[k:])

  # error as in [24, Eq. (35)]
  gamError = absError / np.prod(WholeLebLam)

  # sample from first dimension [24, Eq. (35)]
  firstMarg = gamError * lamX[0] + np.sum(BackMarg[0][0, :, :] ** 2, 1)
  # cumulative distribution function, normalised numerical
  firstCDF = np.cumsum(firstMarg / np.sum(firstMarg))
  # draw samples as 'inverse transform'
  samples[0] = np.interp(seeds[0], firstCDF, univarGrid[0])
  probVal[0] = np.interp(samples[0], univarGrid[0], firstMarg / np.sum(firstMarg))

  # sample from other dimensions
  for n in range(0, numbSampl):
    # interpolate linear on grid in first dimension
    CurrApprCore = LinInterPolTT(SQTT[0], univarGrid[0], samples[0][n])
    for d in range(1, dim):
      # marginal function condition on previous samples
      rank_min, gridSize, rank_pls = BackMarg[d].shape
      MargDep = np.zeros((BackMarg[d].shape))

      for r in range(0, rank_min):
        # condition on previous samples
        MargDep[r, :, :] = CurrApprCore[0, r] * BackMarg[d][r, :, :]

      currMarg = gamError * lamX[d] + np.sum(np.sum(np.copy(MargDep), axis=0)** 2, axis=1)
      currCDF = np.cumsum(currMarg / np.sum(currMarg))

      # draw sample as 'inverse transform'
      samples[d][n] = np.interp(seeds[d][n], currCDF, univarGrid[d])
      probVal[d][n] = np.interp(samples[d][n], univarGrid[d], currMarg / np.sum(currMarg))
      # piecewise polynomial interpolation, see Eq. 2.41, as in [29]
      # multiply (condition) current dimension with previous samples
      CurrApprCore = np.copy(CurrApprCore) @ LinInterPolTT(SQTT[d], univarGrid[d], samples[d][n])

  Approx[n] = gamError + CurrApprCore ** 2

```

```
53  return sampls, probVal, Approx
```

Listing A.2: Python example

```python
def MargForw(TTCore, univarGrid):
''' Forward marginalisation, see Prop. 2, similar to backward marginalsiation as
    in  Cui et al. [24] '''
  # compute pre marginal coefficients sarting at dim = 1, k = 0
  BPre = dim * [None]  # coeffTensor
  LebLam = 1  # !! Lebesgue Measure
  BPre[0] = TTCore[0]
  RPre = [None] * dim
  CPre = [None] * dim

  for k in range(0, dim-1):
    r_kmin1, n, r_k = np.shape(TTCore[k])
    # !! we set Lebesgue Measure to const = one
    M = np.identity(n) * (univarGrid[k][-1] - univarGrid[k][0])  # Mass matrix
    L = scy.linalg.cholesky(M)

    # construct Tensor C [24, Eq.  (27)]
    CPre[k] = np.zeros((r_kmin1, n, r_k))
    for alpha in range(0, r_kmin1):
      for l in range(0, r_k):
        CPre[k][alpha, :, l] = BPre[k][alpha, :, l] @ L[:, :]

    # unfold along first coordinate and compute thin QR decomposition of C
    # 3.1 [24, Eq.  (28)]
    Q, RPre[k] = np.linalg.qr(CPre[k].reshape((r_kmin1 * n, r_k), order='C'), mode
    ='reduced')

    # compute next coefficient tensor
    # [24, Eq.  (29)]
    r_k, n, r_kpls1 = np.shape(TTCore[k + 1])
    BPre[k + 1] = np.zeros(np.shape(TTCore[k + 1]))
    for alpha_1 in range(0, r_kpls1):
      for l_1 in range(0, r_k):
        BPre[k + 1][l_1, :, alpha_1] = RPre[k][l_1,:] @ TTCore[k + 1][:, :,
    alpha_1]

  return BPre

```

Listing A.3: Python example